

# Recent Progress on Structurally Ordered Materials for Electrocatalysis

Hainan Sun, Sanzhao Song, Xiaomin Xu, Jie Dai, Jie Yu, Wei Zhou, Zongping Shao,\* and WooChul Jung\*

Tuning material properties by modulation of the arrangement of atoms is a fundamental and effective strategy in materials science. Structurally long-range ordered materials are increasingly finding utility for electrocatalytic applications. Such ordered structures can achieve unique functions that increase the electrocatalytic activity compared to corresponding electrocatalysts with a disordered structure. Effective strategies for designing high-performance electrocatalysts based on structurally ordered materials are presented. This review also summarizes the recent progress on structurally ordered materials as efficient electrocatalysts and highlights the applications in several representative electrochemical reactions, such as, the oxygen evolution reaction, oxygen reduction reaction, and hydrogen evolution reaction. The structural features of the atomic long-range ordered framework and superior electrochemical performance are demonstrated by advanced characterization techniques (structural identification) and electrochemical measurements (performance evaluations), respectively. Special attention is paid to the establishment of a structure-activity relationship to highlight the advantages of the ordered structure. Finally, the remaining challenges and emerging opportunities in these related materials are proposed.

## 1. Introduction

Many techniques have been developed to mitigate the consumption of fossil fuels and alleviate related environmental problems.<sup>[1]</sup> Among them, fuel cell, water electrolysis, and rechargeable metal-air batteries have been demonstrated as secure, sustainable, and eco-friendly energy conversion techniques.<sup>[2]</sup> For example, due to their high energy density, high

energy conversion efficiency (vs Carnot heat engine), zero carbon emissions, and potential commercial applications in vehicles, fuel cells (hydrogen to electricity, e.g., proton-exchange membrane fuel cells) have attracted tremendous amounts of attention.<sup>[3]</sup> In these devices, the oxygen reduction reaction (ORR) and hydrogen oxidation reaction (HOR) take place at the cathode and anode, respectively.<sup>[2b,4]</sup> Electrochemical water electrolysis (electricity to hydrogen, e.g., an alkaline electrolyzer and a proton-exchange membrane electrolyzer) is a promising technique to realize the hydrogen economy and can be processed in alkaline, acid, neutral, and seawater media according to the types of electrolytes and electrocatalysts used.<sup>[5]</sup> Notably, the necessary electricity can be sustainably supplied from natural resources (e.g., wind, solar, and tidal energy). During this process, the oxygen evolution reaction (OER) and the hydrogen evolution reaction (HER)

take place on the anode and cathode, respectively.<sup>[5b,6]</sup> Similarly, the performance of a rechargeable metal-air battery also relies on the reaction efficiency of the OER and ORR during the charging and discharging processes.<sup>[2c,7]</sup>

In particular, the OER and ORR typically involve four-electron charge-transfer steps coupled with multiple reaction intermediates (e.g., \*OH, \*O, and \*OOH).<sup>[3a,5b,8]</sup> Moreover, their reaction kinetics are strongly restricted by adsorption-energy

H. Sun, W. Jung  
Department of Materials Science and Engineering  
Korea Advanced Institute of Science and Technology (KAIST)  
Daejeon 34141, Republic of Korea  
E-mail: wcjung@kaist.ac.kr

S. Song  
Key Laboratory of Interfacial Physics and Technology  
Shanghai Institute of Applied Physics  
Chinese Academy of Sciences  
Shanghai 201800, P. R. China

 The ORCID identification number(s) for the author(s) of this article can be found under <https://doi.org/10.1002/aenm.202101937>.

DOI: 10.1002/aenm.202101937

X. Xu, Z. Shao  
WA School of Mines: Minerals  
Energy and Chemical Engineering (WASM-MECE)  
Curtin University  
Perth, Western Australia 6845, Australia

J. Dai, W. Zhou, Z. Shao  
State Key Laboratory of Materials-Oriented Chemical Engineering  
College of Chemical Engineering  
Nanjing Tech University  
Nanjing 211816, P. R. China  
E-mail: shaozp@njtech.edu.cn

J. Yu  
Department of Building and Real Estate  
The Hong Kong Polytechnic University  
Hung Hom, Kowloon, Hong Kong 999077, P. R. China

scaling relationships, making the reaction rates commonly two orders of magnitude slower than the corresponding HER and HOR rates.<sup>[8c]</sup> Over the past few decades, various types of functional materials have been developed to catalyze these electrochemical reactions, among which the noble metal (e.g., Ru, Pd, Ir, and Pt)-based electrocatalysts with moderate binding energies for a specific reaction and excellent electrocatalytic activity are still demonstrated as the benchmark materials.<sup>[6c,9]</sup> Considering the scarcity and high cost of these precious metals, one route is to reduce the usage of noble metal while enhancing the overall electrocatalytic performance, including the activity, selectivity, and stability. On the other hand, non-precious-metal electrocatalysts such as alloys, oxides, (oxy)hydroxides, perovskite oxides, transition-metal sulfides, phosphides, selenides, and metal-organic frameworks (MOFs) have been extensively explored.<sup>[2e,10]</sup> Their impressive electrocatalytic performance capabilities make them promising candidates as alternatives to noble metal-based materials. Some good reviews that provide a fundamental understanding of typical reactions and recent research on noble/transition-metal-based functional materials have been provided.<sup>[2e,5b,5c,6a,6c,7a,9a–9c,10a,10b,11]</sup>

Tuning the material properties from the aspect of the atomic arrangement is a fundamental and effective strategy in materials science. Remarkably, materials with the characteristic of a long-range ordered structure have attracted much research interest in heterogeneous catalysis due to the unique physical structures and functional properties.<sup>[4a,12]</sup> The atomically ordered arrangement of metal elements arouses strong intrinsically interatomic interaction. Additionally, the well-defined stoichiometries and flexible control of the local geometry further allow the creation of ordered structure materials that exhibit exceptional physicochemical properties, such as simultaneously increased electrocatalytic performance compared to the disordered counterparts. Moreover, the atomic ordering degrees, element types, and relative concentrations of the elements drastically influence the overall electrocatalytic performance. In addition to the regulation of the atomic ordering, charge/spin ordering and 3D macro(meso) porous ordering are also key parameters that determine the electrocatalytic performance, and several reviews relevant to the topic are available.<sup>[12e,13]</sup> Unfortunately, with the global boom in materials science related to energy storage and conversion systems, thus far, there has been no comprehensive review paper that timely introduces the advantages and applications of structurally ordered materials for electrochemical applications.

This review focuses on materials with an ordered structure and their applications for several representative electrocatalytic reactions (**Figure 1**). We discuss how the chemistries of structurally ordered materials can be tuned toward enhanced functionality. Recent progress on structurally ordered materials as high-performance electrocatalysts are summarized, together with a discussion of catalyst design/synthesis strategies, electrocatalytic capabilities, and the origins of improved activity/stability. Special attention is paid to the understanding of the relationship between the unique ordered structure and electrochemical properties with the assistance of density functional theory (DFT) computational studies. Finally, the remaining challenges and emerging opportunities are discussed in detail.

We anticipate that such a fundamental and comprehensive review can guide the development of more advanced electrocatalysts beyond those with an ordered structure.

## 2. Advantages of an Ordered Structure

Transition-metal- and precious metal-based materials have been extensively investigated as superior electrocatalysts for energy conversion.<sup>[5c,5d,7a,9c,10a,14]</sup> Partial elemental substitutions are demonstrated as an effective method to increase catalytic performance and such electronic interactions between multiple elements are known as synergistic effects.<sup>[9e,10b]</sup> However, serious issues such as random atomic arrangement and ambiguous roles of constituent elements hamper theoretical investigations for rational materials design.

In a disordered structure, the atoms exist randomly along 3D directions, leading to various surface compositions, with arbitrarily distributed active sites. In contrast, structurally long-range ordered compounds with well-defined compositions, stoichiometries, and atomic arrangements pave the way for more predictable regulations of structural, geometric, and electronic effects for the purpose of improving the electrocatalytic performance.<sup>[9d,15]</sup> For solid-state materials, the interatomic interaction is greatly determined by the lattice ordering (e.g., atomic arrangement, bond angle and length, coordination structure). From this perspective, regulating the structural order can help to guide the optimization of exposed sites, trigger the interatomic interaction, and modulate the reaction barrier. In addition to the engineering of the atomic arrangements, particle size control and size distribution strategies are also critical parameters to be tuned for high activity and stability targets.<sup>[1b]</sup> Thus, a combination of certain atomic arrangements and other effective design strategies would boost the exploration of novel electrocatalysts for energy conversion systems.

It is well known that the establishment of well-defined electronic structure-electrocatalytic performance relationships is of great significance for a deeper understanding of reaction mechanisms.<sup>[16]</sup> Unveiling these relationships is also beneficial for the exploitation of more efficient catalysts for applications in sustainable energy conversion. Artificial intelligence has been demonstrated as an effective tool in high-throughput materials design and new catalyst discoveries based on established key descriptors, allowing one to avoid the cumbersome process of conventional trial-and-error methods.<sup>[1b,17]</sup> Furthermore, it is beneficial to construct a structural model for structurally ordered materials with uniform active sites on the same surface plane and with a precise structure, providing more opportunities for DFT calculations. Taken together, structural ordering provides a promising direction for regulating the functional properties of materials.

## 3. Emerging Materials with an Ordered Structure

### 3.1. Perovskite Oxides

Perovskite oxides ( $ABO_3$ ) have been demonstrated as an important type of functional materials.<sup>[10e,11e,14c,18]</sup> The functional

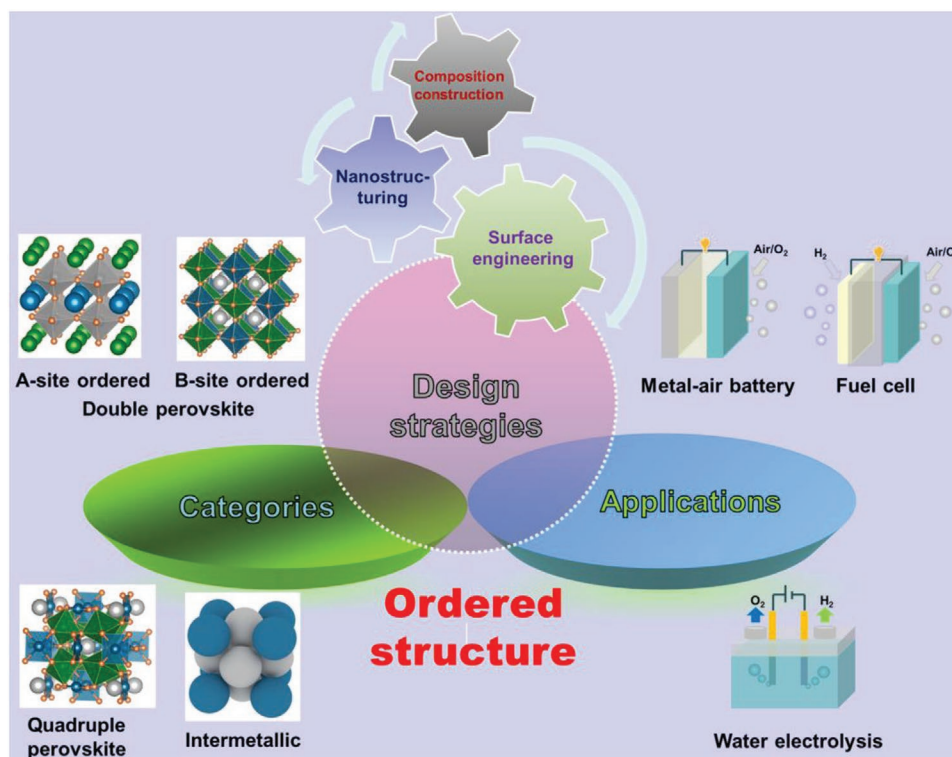


**Figure 1.** A brief description of the categories, applications, and design strategies of structurally ordered materials.

properties of perovskites can be tailored by selecting proper elements in the A/B/O-sites and by regulating the crystal structures.<sup>[2f,11e,19]</sup> Single perovskite oxides exhibit random arrangements of the cation distribution along 3D directions (Figure 2a). In particular, perovskite oxides with a cation-ordered structure exhibit unusual property compared to their single perovskite counterparts, in which the cations are arranged in an ordered manner in the 3D structure.<sup>[12d,12f]</sup> Herein, we provide a summary of perovskite oxides with a cation-ordered structure.

### 3.1.1. A-Site Cation Ordered Double Perovskites

The A-site cation ordered double perovskite  $A'A''B_2O_{5+\delta}$  ( $A'$  represents lanthanides,  $A''$  represents Ba or Sr, and B represents transition-metal elements or a mixture of them) exhibits a layered structure with a stacking sequence of  $[A'O_\delta]-[BO_2]-[A''O]-[BO_2]-[A'O_\delta]$  along the c axis (Figure 2b).<sup>[20]</sup> All oxygen vacancies are confined to the  $A'O$  plane, as is oxygen migration.<sup>[20e]</sup> A-site ordered double perovskite oxides have been extensively explored as promising materials for solid oxide fuel cells.<sup>[21]</sup> The layered structure was found to exhibit faster oxygen diffusion and surface exchange rates than those of single perovskites.<sup>[21,22]</sup>

### 3.1.2. B-Site Cation Ordered Double Perovskites

B-site cation ordered double perovskite  $A_2B'B''O_6$  possesses alternately occupied transition-metal sites (B-sites of

perovskite oxide) of  $B'$  and  $B''$  cations that are distinctive from the single  $ABO_3$  perovskite structure (Figure 2c).<sup>[23]</sup> The formation of  $B'O_6$  and  $B''O_6$  octahedra structures resulting from intervening oxygen bridging the  $B'$  and  $B''$  atom pair usually impart unique properties to the materials. This type of structurally ordered material with a variety of superior properties has been applied in the fields of superconductors, magnetoresistors, multiferroic materials, and catalysts.<sup>[23a,23c,24]</sup> The oxidation states and ionic radii of  $B'$  and  $B''$  cations have a powerful influence on the degree of B-site ordering, which determines the electronic properties. For example, insulating antiferromagnetic behavior and half-metallic ferromagnetic behavior were observed for the double perovskite  $Sr_2FeWO_6$  and  $Sr_2FeMoO_6$ , respectively.<sup>[23a,25]</sup> Thus, novel combinations of  $B'$  and  $B''$  cations and rational regulation of the B-site ordering are the key factors for successful electrocatalysis applications.

### 3.1.3. Quadruple Perovskites

For the B-site ordered double perovskite ( $A_2B'B''O_6$ ), when three-quarters of the A-site can be substituted with another transition-metal  $A'$ , a quadruple perovskite ( $AA_3B_2B''_2O_{12}$ ) with an A-site and B-site ordered structure will form (Figure 2d).<sup>[26]</sup> Due to the square-planar coordination, the  $A'$ -site metal ions are commonly  $Cu^{2+}$  and  $Mn^{3+}$  ions with strong Jahn-Teller distortions.<sup>[26,27]</sup> Because the low-field magnetoresistance effect of ordered perovskites is associated with antisite disorder between the B-site and the  $B'$ -site ions, it is possible to realize B/ $B'$

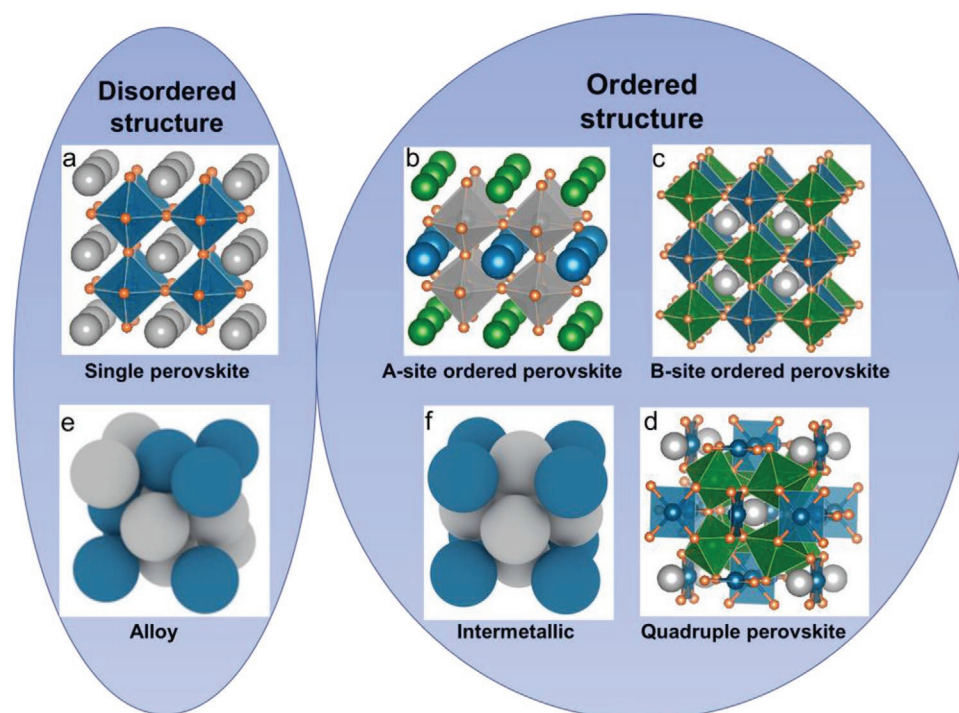


**Figure 2.** An illustration of emerging materials with an ordered structure in comparison to counterparts with a disordered structure. a) Single perovskite, b) A-site cation ordered double perovskite, c) B-site cation ordered double perovskite, d) quadruple perovskite, e) alloy, and f) intermetallic.

sites with an ordered degree of nearly 100%.<sup>[27a]</sup> Such a peculiar two-site ordered perovskite exhibits versatile electronic and functional properties.<sup>[28]</sup>

### 3.2. Intermetallics

A common alloy is a single-phase solid solution in which different types of atoms adopt statistically random positions within the lattice (Figure 2e). A conventional alloy typically consists of only one, two, or occasionally three elements.<sup>[11f,29]</sup> Introducing low-cost and earth-abundant elements into a noble-metal-based alloy not only reduces the cost of the noble-metal-based materials but also effectively enhances the electrocatalytic performance. Intermetallic compounds induced by a combination of ionic (partial charge transfer) and covalent bonding exhibit an atomic ordering structure (Figure 2f), which is the main difference from substitutional alloys with a disordered structure.<sup>[12c]</sup> The energy barrier is the activation energy for atomic ordering, which is closely related to the diffusion kinetics of the atoms and the bonding energy.<sup>[9d]</sup> Constituent elements at precisely determined positions in an ordered fashion endow the intermetallic structure with inherent thermodynamic stability, providing outstanding structural robustness under electrochemical reaction conditions. For instance, Matsumoto et al. found that the formation of the PtBi ordered phase increased the leaching potential of Bi, leading to the dramatically enhanced operational stability of the ordered structure.<sup>[30]</sup> Thus, the catalytic performance of intermetallic materials varies greatly from those of the corresponding elements or alloys, originating from the modulated electronic structure beyond the arrangement of the atoms.

## 4. Optimization Strategies for Structurally Ordered Materials

### 4.1. Surface Engineering

Electrocatalysis takes place on the surfaces of the catalysts; thus, a rational surface modification scheme can effectively improve the catalytic activity.<sup>[31]</sup> Novel physiochemical properties, such as, a tuned electronic structure, additionally created active sites, and a strong synergistic effect, can be generated by surface and interface atomic engineering.<sup>[32]</sup>

#### 4.1.1. Ex-Solution

Perovskite oxide is a good candidate for an in situ ex-solution due to its compositional flexibility and structural stability.<sup>[33]</sup> The ex-solution process will increase oxygen vacancies into the lattice of the residual perovskite oxide and generate highly conductive metal particles on the surface.<sup>[33c]</sup> Importantly, according to previous reports, the introduced oxygen vacancies and ex-solved metal nanoparticles are both favorable factors for the OER process.<sup>[5b,6d]</sup> Given these considerations, Zhu et al. synthesized  $\text{Sr}_2\text{Fe}_{1.3}\text{Ni}_{0.2}\text{Mo}_{0.5}\text{O}_{6-\delta}$  decorated with the Fe-Ni alloy and oxygen vacancies.<sup>[34]</sup> Theoretical calculations revealed that oxygen vacancies can increase the adsorption energy of water. Moreover, the ex-solved alloy nanoparticles dramatically increased the available OER active sites on the surface. As expected, a double perovskite oxide decorated with nanoparticles exhibited OER activity superior to the pure-phase counterpart and single perovskite BSCF and comparable to the commercial  $\text{IrO}_2$ . Furthermore, surface

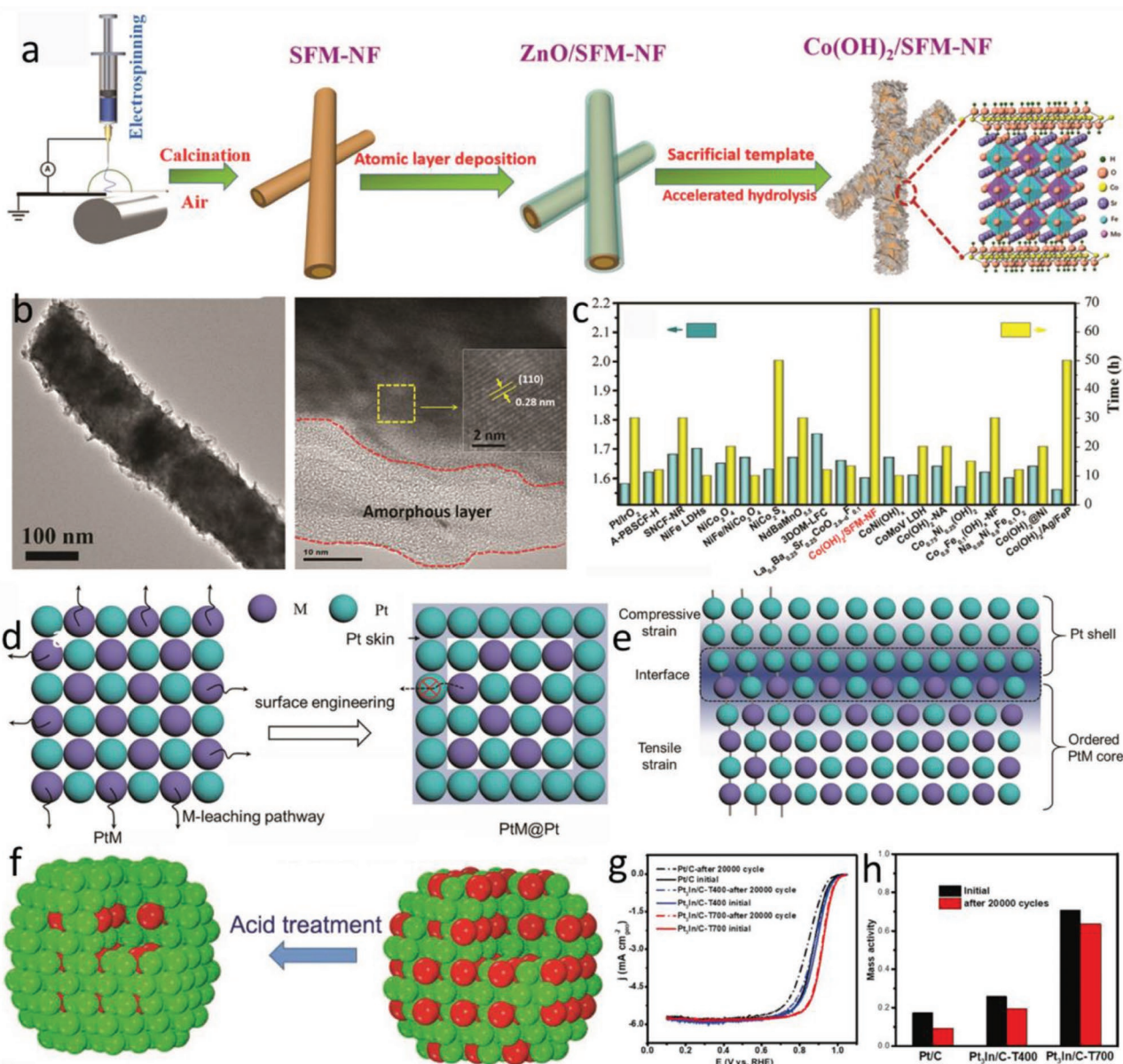


**Figure 3.** a) Schematic illustration of the synthesis of the core-shell structure. b) TEM images of  $\text{Co}(\text{OH})_2/\text{SFM-NF}$ . c) Comparison of the overall water electrolysis activity (potential at  $10 \text{ mA cm}^{-2}$ ) and stability of the represented catalysts reported here. Reproduced with permission.<sup>[37]</sup> Copyright 2020, Royal Society of Chemistry. d) Surface engineering process from intermetallic PtM to the core-shell structure of PtM@Pt. e) Strain effect on the interface between the Pt shell and the intermetallic PtM core. Reproduced with permission.<sup>[94]</sup> Copyright 2021, Royal Society of Chemistry. f) Schematic illustration of the synthesis of  $\text{Pt}_3\text{In/C-T700}$  by an acid treatment. g) LSV curves and h) mass activity before and after the CV test. Reproduced with permission.<sup>[38]</sup> Copyright 2020, Wiley-VCH.

self-reconstruction for an alloy-supported metal oxide under electrocatalytic conditions has recently been studied by advanced techniques (e.g., in situ/operando XAS). The ex-solved metals tend to restructure into metal (oxy)hydroxides under OER conditions, serving as the real active sites for the electrocatalytic reaction.<sup>[35]</sup>

#### 4.1.2. Surface Decoration

A rational surface decoration technique can increase the number of exposed active sites, enhance the electrical conductivity, and

lower the reaction energy barrier at the surface/interface of the material.<sup>[36]</sup> The double perovskite  $\text{Sr}_2\text{Fe}_{1.5}\text{Mo}_{0.5}\text{O}_{6-\delta}$  (SFM) was selected as the core structure owing to its diverse spin and oxidation states of Fe and Mo ions, making it likely show good electrocatalytic activity.<sup>[37]</sup> Cobalt hydroxide  $\text{Co}(\text{OH})_2$  with a 2D and layered open structure has been demonstrated to possess high OER and HER activity levels. Thus, the core-shell structure was fabricated by electrospinning and atomic layer deposition techniques (Figure 3a). Importantly, a  $\text{Co}(\text{OH})_2$  amorphous layer with a thickness of  $\approx 10\text{--}15 \text{ nm}$  was evenly generated on the perovskite surface (Figure 3b). Benefitting from the abundant

oxygen vacancies, large electrochemical surface area, and fast electron transfer rate through the surface decoration strategy, Co(OH)<sub>2</sub>/SFM-NF exhibited improved OER and HER activities. Impressively, when assembled as an overall water electrolysis system, the cell can drive 10 mA cm<sup>-2</sup> at a low voltage of 1.6 V and exhibit long-term stability, surpassing many reported bifunctional materials for alkaline water splitting (Figure 3c). This work provided a general surface decoration strategy for the development of high-performance electrocatalysts for water splitting.

Transition-metal leaching of ordered PtM intermetallic materials during the acidic ORR directly influences the operational stability of the material. Constructing Pt skin on ordered PtM intermetallic nanoparticles is an effective strategy to design highly efficient intermetallic electrocatalysts. Surface dealloying is carried by the selective leaching of the surface transition metal (M) and by stacking smooth Pt layers on the surfaces of the intermetallic PtM nanoparticles (Figure 3d).<sup>[9d,31a]</sup> Electrochemical dealloying and chemical dealloying are methods frequently adopted to realize surface dealloying.

Electrochemical dealloying is typically conducted on thin-film catalysts, such as, those coated onto a glassy carbon electrode. During the electrochemical reaction in an acidic electrolyte, the surface transition metal is dissolved in the solution and the remaining Pt on the surface forms a smooth Pt shell.<sup>[9d]</sup> The electrochemical dealloying induced Pt shell and surface strain from the intermetallic PtM core significantly enhance the ORR performance (Figure 3e), which has been demonstrated by intermetallic PtCo, PtCo<sub>3</sub>, Pt<sub>3</sub>Fe, PtFe, PtFe<sub>3</sub>, Pt<sub>2</sub>CoNi, PtCu<sub>3</sub>, and PtSn after the electrochemical dealloying process. For the chemical dealloying process, the obtained PtM intermetallic powders undergo an acid treatment in order to leach out the transition metal and realize a Pt-rich surface. For example, a carbon-supported Pt<sub>3</sub>In intermetallic was first prepared and chemical dealloying in an acid solution was used to obtain a Pt shell on the Pt<sub>3</sub>In nanoparticles surface (Figure 3f).<sup>[38]</sup> Pt<sub>3</sub>In@Pt shows desirable ORR activity (mass activity of 0.71 A mg<sub>Pt</sub><sup>-1</sup>) and impressive durability (Figure 3g,h). The core-shell structure and the optimized oxygen-binding energy jointly contribute to the improved ORR performance.

In addition to the dealloying process, Tang et al. presented a deposition method to construct a core-shell structure based on the PtM intermetallic.<sup>[39]</sup> Briefly, trace Pd atoms (1.8 at%) were introduced to optimize the surface of intermetallic PtBi nanoplates, which contributed to the formation of tensile-strained Pd and electronic-modulated intermetallic PtBi. Due to the synergistic effect between the PtBi intermetallic and Pd atoms, enhanced formic acid oxidation activity was achieved. Furthermore, Gong et al. combined a dealloying process and surface atom decoration to obtain the Pt-decorated porous PdFe intermetallic.<sup>[15a]</sup> The clean surface of the structurally ordered PdFe intermetallic was first exposed to an acidic solution. Then, the obtained porous intermetallic was immersed in a H<sub>2</sub>PtCl<sub>6</sub> solution and the Pt-decorated porous PdFe intermetallic was obtained. Impressively, the rationally designed porous ordered PdFe@Pt catalyst exhibited a 28-fold enhancement in the ORR activity compared to that of Pt/C and only 15% activity degradation after 10 000 cycles. Importantly, the chemically sensitive 3D tomography, which could provide a visualized structure

and a composition change, revealed that the gradual surface Pt rearrangement is the key factor related to the improved ORR performance.

#### 4.1.3. Surface Self-Reconstruction

Surface self-reconstruction during electrochemical reactions is widely reported in various types of materials and electrolytes (e.g., alkaline and acidic media). The surface-active sites of catalysts undergo structural self-reconstruction coupled with a change of the electrocatalytic activity under oxidation or reduction processes.<sup>[40]</sup> For perovskite oxides, A-site metals are highly prone to leaching in acidic electrolytes compared to alkaline electrolytes.<sup>[5b,18a,41]</sup> Surface reconstruction induced by cation leaching under an electrochemical reaction condition in an acid solution is a major issue when developing perovskite oxide-based electrocatalysts.<sup>[5b,10e,42]</sup> Notably, there would also be different observed electrochemical activities followed by the respective reaction mechanisms for materials with different structures. Zhang et al. studied the OER activities of Sr<sub>2</sub>MIrO<sub>6</sub> (M = Fe and Co, B-site cation ordered double perovskite) and Sr<sub>2</sub>Fe<sub>0.5</sub>Ir<sub>0.5</sub>O<sub>4</sub> (Ruddlesden-Popper structure).<sup>[43]</sup> Interestingly, Sr<sub>2</sub>CoIrO<sub>6</sub> exhibited relatively stable electrocatalytic activity during cycling testing (activity superior to that of commercial micron-sized IrO<sub>2</sub>), while the catalytic behaviors of Sr<sub>2</sub>FeIrO<sub>6</sub> and Sr<sub>2</sub>Fe<sub>0.5</sub>Ir<sub>0.5</sub>O<sub>4</sub> were surprisingly similar regardless of the remarkable differences in their crystal structures (Figure 4a,b). Independent of the crystal structure and composition of perovskite-like catalysts, their OER activities normalized to Brunauer–Emmett–Teller surface areas after the activation process are comparable to those of Ir<sup>5+</sup>-based Ba<sub>2</sub>LnIrO<sub>6</sub> and La<sub>2</sub>LiIrO<sub>6</sub>. An additional study revealed that the electrocatalytic activities of Ir<sup>5+</sup>-based perovskite-like catalysts are eventually dominated by the in situ-formed IrO<sub>x</sub>·mH<sub>2</sub>O triggered by the potential-dependent dissolution/precipitation process (Figure 4c).<sup>[44]</sup> Very recently, we found that the high electrochemical activity of double perovskite Sr<sub>2</sub>CoIrO<sub>6,δ</sub> in alkaline media was not only ascribed to the ordered structure but also contributed from the in situ formation of high-valence Ir<sup>5+/6+</sup> and Co<sup>4+</sup> metal site (Figure 4d–f).<sup>[45]</sup> This work opens a promising path to overcome the sluggish kinetics of OER bottleneck for water splitting via proper arrangements of the multi-active sites in the catalyst.

Designed precatalysts, especially for alloy-type materials, are found to undergo obvious compositional changes under electrochemical reaction conditions. Intermetallics can easily be transformed into metal oxides/hydroxides; thus, the rational design of a precatalyst coupled with an in situ-generated active surface structure is the key when applying intermetallic materials as highly active electrocatalysts.<sup>[46]</sup> Moreover, for transition-metal-based materials, especially those containing a 3d transition metal, independent of the material types (e.g., oxides, alloys, (oxy)hydroxides, and sulfides) and the synthetic routes, the surface formation of (oxy)hydroxides was confirmed and (oxy)hydroxides were demonstrated as the real active sites for the OER.<sup>[47]</sup> It was found that Fe-based intermetallic Fe<sub>6</sub>Ge<sub>5</sub> would undergo a structural transformation into a core-shell-like structure. In detail, conductive intermetallic Fe<sub>6</sub>Ge<sub>5</sub> acts as the core, and the in situ-formed amorphous material (K<sub>x</sub>FeO<sub>2</sub>H<sub>y</sub>)

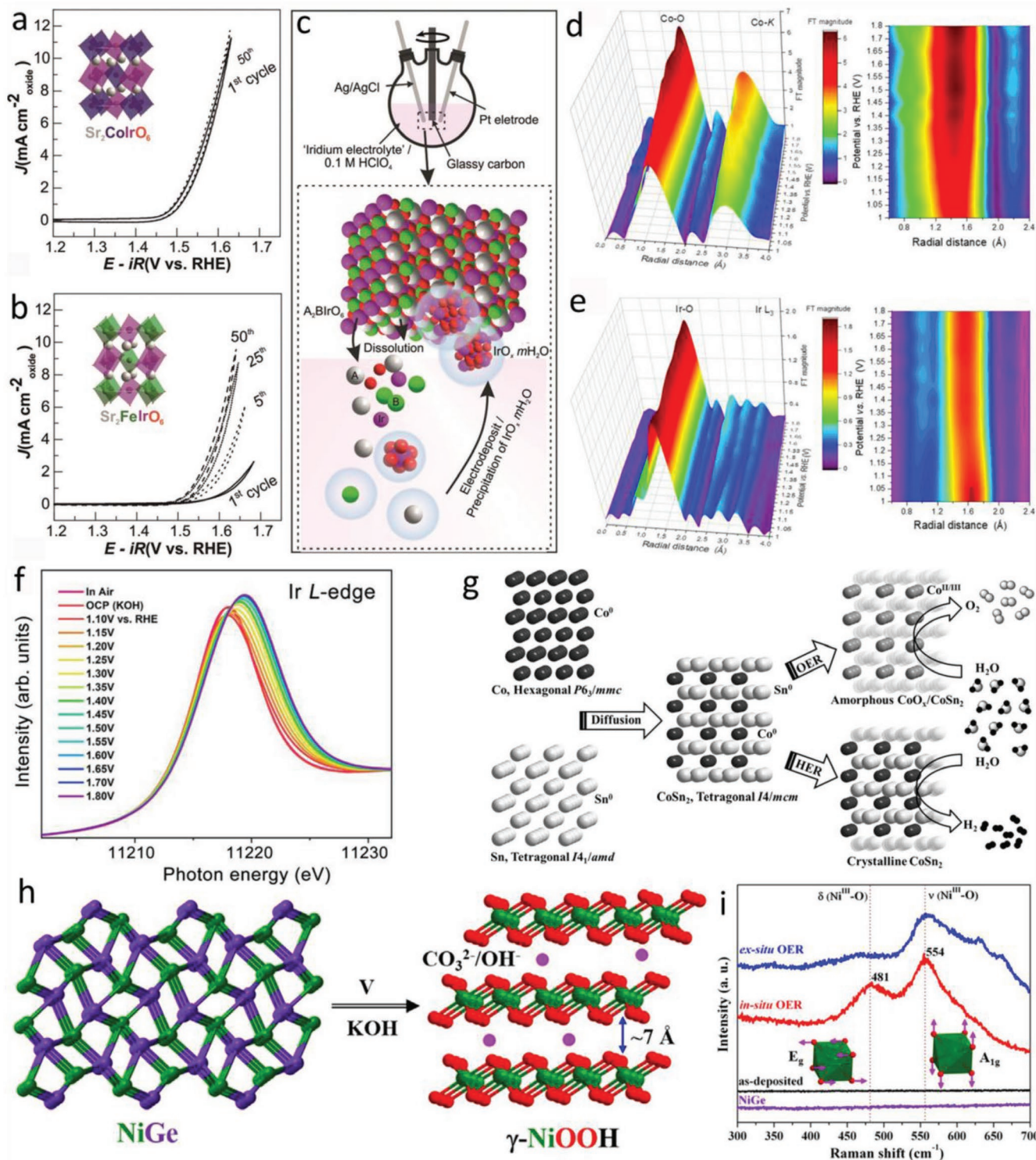


**Figure 4.** CV curves toward the OER for a)  $\text{Sr}_2\text{CoIrO}_6$  and b)  $\text{Sr}_2\text{FeIrO}_6$  in acidic media and their corresponding crystal structures (insets). c) Experimental set ups for OER activity evaluations and the proposed OER catalytic mechanism involving the dissolution-electrodeposition of iridium species. Reproduced with permission.<sup>[43]</sup> Copyright 2019, Wiley-VCH. 3D operando Fourier transforms of d)  $k^3$ -weighted EXAFS spectra at the Co-K edge and e)  $k^2$ -weighted EXAFS spectra at the Ir-L<sub>3</sub> edge as a functional of applied potential, along with corresponding enlarged 2D contour plots of Co-O and Ir-O. f) Ir-L<sub>3</sub> edge XANES spectra of  $\text{Sr}_2\text{CoIrO}_{6-\delta}$  electrocatalyst at different applied voltages. Reproduced with permission.<sup>[45]</sup> Copyright 2021, Wiley-VCH. g) Structural transformations of intermetallic  $\text{CoSn}_2$  during the OER and HER processes. Reproduced with permission.<sup>[50]</sup> Copyright 2018, Wiley-VCH. h) Crystal structure of  $\text{NiGe}$  (precatalyst) and  $\gamma\text{-NiOOH}$  (in situ formed under electrochemical conditions). i) Quasi in situ and ex situ Raman spectroscopy of  $\text{NiGe}$  on fluorinated tin oxide collected at a potential of 1.58 V. Reproduced with permission.<sup>[51]</sup> Copyright 2021, Wiley-VCH.

serves as the shell.<sup>[48]</sup> Impressively, this Fe-based OER catalyst shows a low Tafel slope ( $32 \text{ mV dec}^{-1}$ ) and a small overpotential of  $272 \text{ mV}$  to drive a high current density ( $100 \text{ mA cm}^{-2}$ ) in alkaline media. Similarly, recent works also demonstrated the in situ formation of a core-shell structure as a common phenomenon and first-row transition-metal-based oxyhydroxides (shell structure) as the real active sites.<sup>[49]</sup> Menezes et al. presented non-noble intermetallic  $\text{CoSn}_2$  nanocrystals as a precatalyst for electrocatalytic overall water-splitting.<sup>[50]</sup> The leaching of Sn from the lattice and the oxidation of Co under the reaction conditions lead to the formation of highly disordered amorphous active Co (oxy)hydroxides, which were the original active sites for the observed high OER activity (Figure 4g). Moreover, the in situ-formed metallic Co is the active site for the HER, and the presence of Sn provides high electronic conductivity. The high OER and HER activities of intermetallic  $\text{CoSn}_2$  enable an overall water electrolyzer with a small cell voltage of  $1.55 \text{ V}$  at  $10 \text{ mA cm}^{-2}$ . Ni-based intermetallic was also found with similar electrochemical behavior. For example, intermetallic NiGe deposited on both nickel foam and fluorinated tin oxide electrodes exhibited superior OER activity and stability (over three weeks) to those of state-of-the-art Ni-, Co-, Fe-, and benchmark NiFe-based electrocatalysts.<sup>[51]</sup>  $\gamma\text{-NiOOH}$  with intercalated  $\text{OH}^-/\text{CO}_3^{2-}$ , which was electrochemically transformed from NiGe, was found to act as the true active species from combined ex situ characterizations and quasi in situ Raman spectroscopy (Figure 4h,i).

## 4.2. Composite Construction

In addition to developing a pure phase structure, interface engineering by the construction of a composite material is also a widely used strategy to optimize the electrocatalytic activity.<sup>[52]</sup> Generally, interfacial interactions can induce synergistic effects originating from the optimized free energies of the reaction intermediates, the considerable electron transfer channels, and the electronic coupling effect.<sup>[53]</sup> A-site ordered double perovskite-based heterostructures have been developed as efficient OER, ORR, and HER electrocatalysts, such as,  $\text{PrBa}_{0.5}\text{Sr}_{0.5}\text{Co}_2\text{O}_{5+\delta}@\text{FeOOH}$  and  $(\text{PrBa}_{0.8}\text{Ca}_{0.2})_{0.95}(\text{Co}_{1.5}\text{Fe}_{0.5})_{0.95}\text{Co}_{0.05}\text{O}_{5+\delta}$  nanofibers/Co/CoO<sub>x</sub> nanosheets.<sup>[54]</sup> Particularly, Liu reported a double/single perovskite heterostructure containing tetragonal double perovskite  $\text{PrBaCo}_2\text{O}_{5.87}$  and cubic single perovskite  $\text{PrCoO}_3$  requiring a low overpotential ( $364 \text{ mV}$ ) to afford a large current density ( $500 \text{ mA cm}^{-2}$ ) toward the HER in alkaline media (Figure 5a,b).<sup>[55]</sup> Single-perovskite nanorods promoted conductivity and enhanced the electrochemical active sites. The 1D nanostructure improved the hydrophilicity of the catalyst surface, ensuring superior long-time stability when operating at large current densities. DFT calculations revealed that the heterostructure displayed optimal water adsorption/dissociation and  $\text{OH}^*$  desorption properties, suggesting the advantage of the perovskite-based heterostructure for electrocatalysis (Figure 5c). Our group also designed a single/double perovskite hybrid that can simultaneously utilize bulk and surface properties of single and double perovskite oxides (Figure 5d).<sup>[52b]</sup> Single perovskite was found unstable and double perovskite can maintain the phase

structure, which was reflected by in situ synchrotron X-ray diffraction (XRD) patterns (Figure 5e). Combining the advantages of single and double perovskite oxides, a limited surface self-reconstruction mechanism was also presented (Figure 5f).

As mentioned above, the core-shell structure has been demonstrated as effective for realizing synergistic effects to enhance the electrocatalytic activity and durability simultaneously.<sup>[9d,56]</sup> For intermetallic Pt-alloy nanoparticles, the loss of transition metals from the crystal lattices under reaction conditions would cause the ordered structure to collapse. Thus, the rational design of an intermetallic Pt-alloy core with a Pt-rich shell can enhance the Pt mass activity further and maintain good stability toward the ORR.<sup>[9d,11f,12b]</sup> As a good case, a core-shell structure was constructed containing intermetallic  $\text{Pt}_3\text{Fe}$  as the core and Pt atoms as the shell; it was then embedded onto a porous atomically dispersed Fe-N-C support (Figure 5g).<sup>[57]</sup> Remarkably, the hybrid structure exhibits superior ORR activity with a half-wave potential of  $0.923 \text{ V}$  (vs RHE) along with good durability (Figure 5h). In addition to the advantages of the core-shell structure, the Fe-N-C structure is also highly active for the ORR, and the close proximity between the Fe-N<sub>4</sub> active sites and the alloy nanoparticles creates synergistic catalysis, as demonstrated by experimental data and computational analyses (Figure 5i).

## 4.3. Nanostructuring

Perovskite oxides synthesized by conventional synthetic methods (e.g., solid-state reactions, sol-gel method, and high-pressure synthesis) commonly exhibit large particle sizes and few morphological features.<sup>[18c]</sup> To make more active sites available on the surface, decreasing the particle size is the most effective strategy. In addition to remarkably improving the mass activity, the intrinsic properties can also be regulated as the particle size decreases in nanostructured materials. Recently, developing well-regulated nanostructures (e.g., nanofibers, nanotubes, and nanoarrays) has been demonstrated as an effective strategy to design high-performance electrocatalysts.<sup>[10e,58]</sup>  $\text{PrBaCo}_2\text{O}_{5+\delta}$  exhibits intrinsic activity toward the OER comparable to that of BSCF. To overcome the low specific surface area owing to the conventional high calcination temperatures and to improve the mass activity further, Zhao et al. synthesized  $\text{PrBa}_{0.5}\text{Sr}_{0.5}\text{Co}_{1.5}\text{Fe}_{0.5}\text{O}_{5+\delta}$  (PBSCF) nanofibers by a strategy of co-doping and nanostructure engineering. PBSCF with an average diameter of  $20 \text{ nm}$  exhibited significantly enhanced OER activities compared to bulk PBSCF powder and other reported advanced perovskite catalysts.<sup>[59]</sup> Porous structures, including microporous, mesoporous, and macroporous structures with a rich porous architecture generally provide large surface areas.<sup>[2f]</sup> The rich pores offer free pathways for electrolyte diffusion, enabling good interaction between the active sites on the surface and the reactants. The nanosize effect was also demonstrated by synthesizing hierarchically porous PBSCF by a general inorganic salt-template strategy (Figure 6a).<sup>[60]</sup> The hierarchically porous structure facilitated the mass transfer and provided a high surface area ( $148 \text{ m}^2 \text{ g}^{-1}$ ), thus exposing more surface-active sites. Furthermore, the introduction of P, which originated from the  $\text{K}_3\text{PO}_4$  template, created Fe and Co with

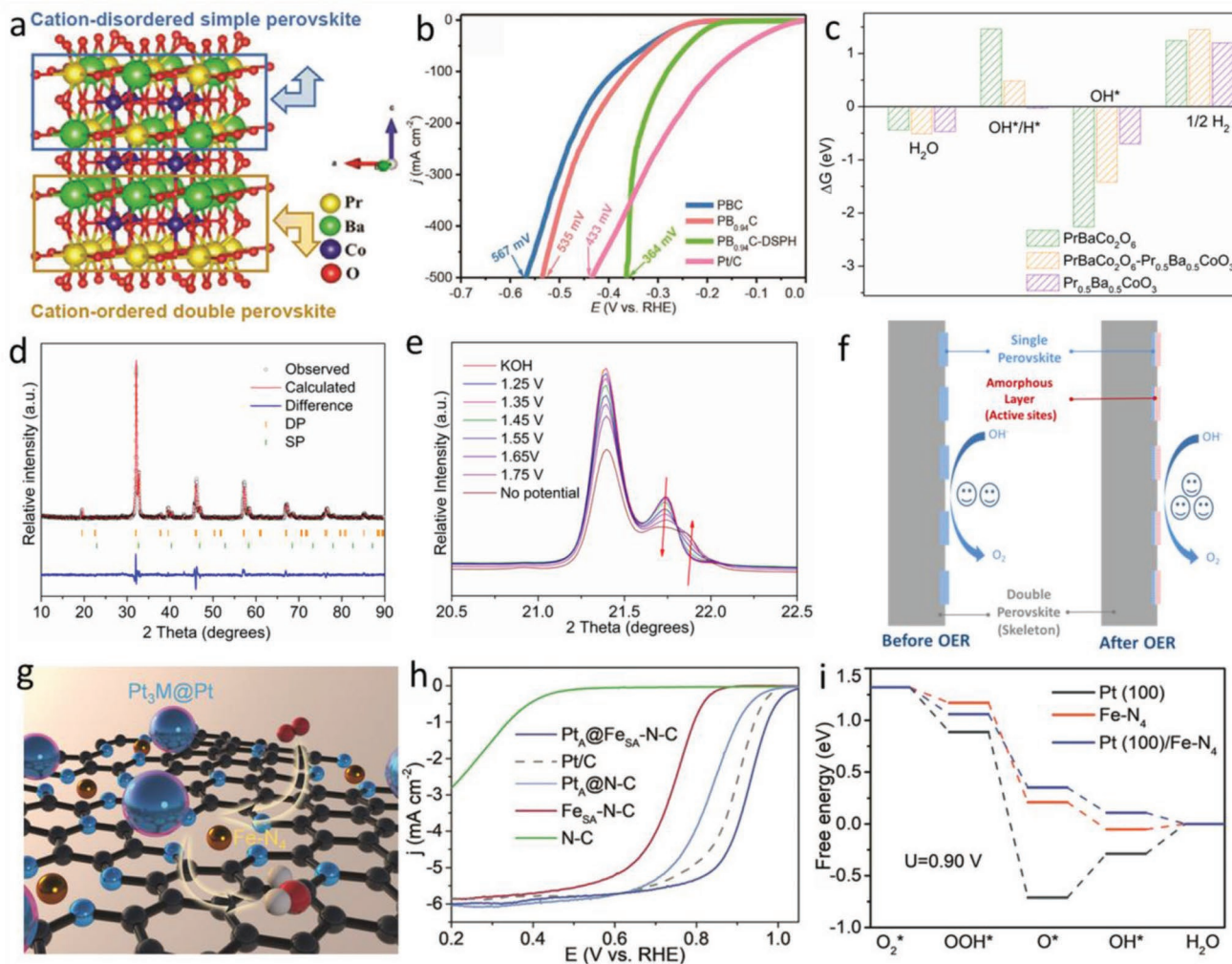


**Figure 5.** a) Crystal structure of a heterostructure containing double perovskite  $\text{PrBaCo}_2\text{O}_6$  and single perovskite  $\text{Pr}_{0.5}\text{Ba}_{0.5}\text{CoO}_3$  (PB0.94C-DSPH). b) LSV curves of double perovskite  $\text{PrBaCo}_2\text{O}_6$  (PBC), PB0.94C-DSPH,  $\text{PrBa}_{0.94}\text{Co}_2\text{O}_{5+\delta}$  (PB0.94C), and Pt/C catalysts toward the HER in alkaline media. c) Calculated free energies for the HER on the (100) surfaces of the  $\text{PrBaCo}_2\text{O}_6$ ,  $\text{PrBaCo}_2\text{O}_6\text{-Pr}_{0.5}\text{Ba}_{0.5}\text{CoO}_3$  heterostructure, and  $\text{Pr}_{0.5}\text{Ba}_{0.5}\text{CoO}_3$ . Reproduced with permission.<sup>[55]</sup> Copyright 2020, Wiley-VCH. d) Structural refinements of the XRD patterns for single/double perovskite hybrid. e) In situ synchrotron XRD of the single/double perovskite catalyst under the OER conditions. f) Schematic of the proposed reaction mechanism for the single/double perovskite catalyst before and after OER catalysis. Reproduced with permission.<sup>[52b]</sup> Copyright 2020, Wiley-VCH. g) Schematic of  $\text{Pt}_3\text{M@Pt}$ . h) LSV curves of different catalysts toward the ORR in acidic media. i) Calculated free energies for the ORR at a potential of 0.9 V for Pt(100)/Fe-N<sub>4</sub>, Pt(100), and Fe-N<sub>4</sub>. Reproduced with permission.<sup>[57]</sup> Copyright 2020, Royal Society of Chemistry.

higher valence states, which was also the key factor behind the promoted OER performance. In particular, 3D ordered meso- and macroporous morphologies have allowed new electrocatalysts to emerge.<sup>[19]</sup> The periodic pore arrangement further enhances certain catalytic properties, such as, the operational durability. Unique structures can be obtained via wet chemical processes and templating routes. Recently, more attention is focused on the preparation of single perovskite oxides.<sup>[2f,13b]</sup> For example, Dai et al. prepared 3D ordered macroporous (3DOM) single perovskite oxide  $\text{LaFeO}_3$  using a template of monodispersed PMMA spheres.<sup>[61]</sup> Honeycomb-like morphologies with well-ordered and interconnected pore channels can be obtained via this route. Remarkably, enhancement of approximately two times and four times of the OER and HER activities, respectively were realized together with greatly improved OER

durability. According to a report by Mei et al., 3DOM double perovskite oxides  $\text{La}_2\text{NiMO}_6$  ( $M = \text{Cu, Co, Fe, Mn}$ ) were prepared by the colloidal crystal template approach.<sup>[62]</sup> First, the unique 3DOM structure improves the interactions between the soot and the catalyst. Meanwhile, the periodic arrangement of  $[\text{MO}_6]$  and  $[\text{NiO}_6]$  octahedrons in the double perovskite structure induced the generation of coordination unsaturated B-site ions. However, reports of the synthesis of double-perovskite-based ordered porous structures and their applications to electrocatalysis remain limited. Combining structurally ordered intermetallic with mesoporous carbon was also demonstrated as an effective approach by which to design durable electrocatalysts. Zhao et al. prepared mesoporous carbon-supported  $\text{Pt}_3\text{Co}$  intermetallic nanoparticles, including the steps of carbonization, impregnation, freeze-drying, and high-temperature annealing

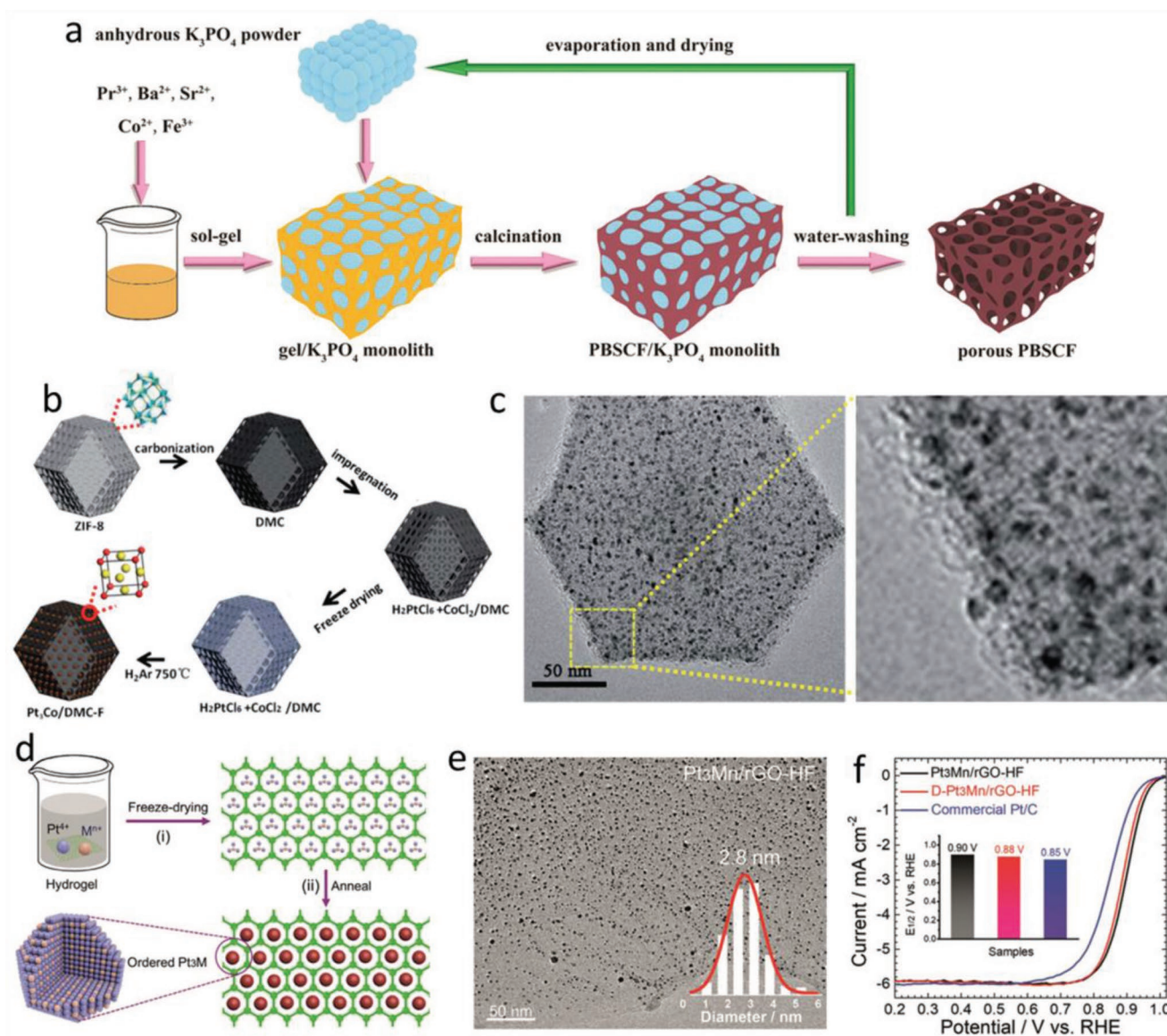


**Figure 6.** a) Schematic illustration of the synthesis of porous PBSCF. Reproduced with permission.<sup>[60]</sup> Copyright 2019, Royal Society of Chemistry. b) Schematic of the preparation procedures of Pt<sub>3</sub>Co/DMCF. c) TEM images of Pt<sub>3</sub>Co/DMCF-F with an enlarged view of the selected area. Reproduced with permission.<sup>[63]</sup> Copyright 2020, Royal Society of Chemistry. d) Schematic illustration of the preparation process of Pt<sub>3</sub>M composites. e) TEM images of Pt<sub>3</sub>Mn/rGO-HF; the insets show the corresponding particle-size histogram. f) LSV curves of ordered/disordered Pt<sub>3</sub>Mn and Pt/C toward the ORR. Reproduced with permission.<sup>[15b]</sup> Copyright 2020, Wiley-VCH.

in a reductive atmosphere (Figure 6b).<sup>[63]</sup> The average size of the Pt<sub>3</sub>Co intermetallic nanoparticles, estimated from the corresponding histograms, is  $2.9 \pm 0.5$  nm. Pt<sub>3</sub>Co intermetallic nanoparticles exhibited a uniform morphology and narrow particle size distribution (Figure 6c). The pore confinement not only prevents aggregation during the annealing and electrochemical reaction processes but also effectively suppresses detachment. The combination of the ordered crystal structure and the ordered porous structure is expected to exhibit exceptional functional properties.

Although the transformation from a disordered alloy to an intermetallic involves high-temperature annealing, the obtained intermetallic particle size is normally up to 10 nm.

Notably, the nanosized level is difficult to realize in perovskite oxides. However, a high-temperature thermal treatment process results in a relatively wide size distribution of intermetallic materials. Moreover, both computational and experimental studies suggest that high-performance Pt-based ORR catalysts require a particle size between 2 and 4 nm.<sup>[9d,15b,63]</sup> Improving the interaction between intermetallic nanoparticles and the carbonaceous matrix can prevent aggregation during the electrochemical reaction. Han et al. designed a composite material including conductive N-doped carbon as the support and size-controlled PtZn intermetallic nanoparticles, which were modified with tetra(4-carboxyphenyl)porphine anchored Pt sites.<sup>[64]</sup> First, zeolitic imidazolate frameworks (ZIFs) were

selected as the precursor to synthesize Pt-based intermetallic nanoparticles. The introduction of Zn allows the synthesis of the intermetallic to happen at a low pyrolysis temperature. N-doped carbon can also serve as the active sites for the ORR. More importantly, TCCP acted as a bridge to coordinate with Pt ions and ZIF-8. Upon pyrolysis, uniform PtZn intermetallic nanoparticles with a well-defined size were formed in situ on N-doped carbon. Specifically, when the size of the nanoparticles reached 5 nm, the catalyst exhibited the best ORR activity with an enhancement of approximately four times compared to Pt/C in terms of the mass activity. In another study by Yang's group, they synthesized sub-3 nm PtCo intermetallic nanoparticles supported on mesoporous carbon using the strong electronic adsorption method.<sup>[65]</sup> The size of the nanoparticles was well controlled by tuning the pH of the carbon support and the precursor suspensions. Zhang et al. also presented a controllable and general strategy to synthesize atomically intermetallic Pt<sub>3</sub>M (M = Mn, Cr, Fe, Co, etc.) nanoparticles.<sup>[15b]</sup> Reduced-graphene oxide-supported Pt<sub>3</sub>M was prepared by a hydrogel-freeze-drying method (Figure 6d). Intermetallic Pt<sub>3</sub>M exhibits an ultra-small particle size ( $\approx 3$  nm) and superior monodispersity (Figure 6e). The well-kept porous structure can immobilize the metal precursors with a defined atomic ratio on the graphene oxide support during solvent sublimation. Specifically, intermetallic Pt<sub>3</sub>Mn nanoparticles exhibited outstanding ORR activity compared to that of disordered nanoparticles and commercial Pt/C (Figure 6f). This work demonstrated a scalable and economical approach for the controllable preparation of Pt-based intermetallic materials.

## 5. Applications of Structurally Ordered Materials in Electrocatalysis

### 5.1. Applications of A-Site Cation Ordered Double Perovskites

The A-site cation ordered double perovskite structure has been confirmed to be stable during the OER, ascribed to the proper O *p*-band center position relative to the Fermi level.<sup>[66]</sup> Wang et al. reported an A-site ordered double perovskite capable of functioning as an outstanding catalyst for alkaline water splitting.<sup>[67]</sup> NdBaMn<sub>2</sub>O<sub>5.5</sub> exhibited superior OER and HER activities relative to its disordered counterparts (see their crystal structures in Figure 7a). The optimized  $e_g$  occupancy, O *p*-band center position, and distorted structure enabled an elaborately designed structure and composition with significantly enhanced activities (Figure 7b–d). Remarkably, NdBaMn<sub>2</sub>O<sub>5.5</sub> achieved a larger current density than that of Pt/C (HER)-RuO<sub>2</sub> (OER) at large potentials as well as excellent stability.

In particular, LnBaCo<sub>2</sub>O<sub>5+ $\delta$</sub>  (Ln = lanthanides) have received much attention from researchers as cathode materials for intermediate-temperature solid oxide fuel cells due to their faster surface oxygen exchange, easier oxygen ion diffusion, and higher conductivity at lower temperatures compared to those of single perovskite oxides.<sup>[21,68]</sup> In the layered structure, oxygen deficiency tends to arise in the LnO layers owing to the high stability of A-site ordering. Moreover, the concentration of oxygen vacancies varies with the synthesis conditions.<sup>[69]</sup> Miao et al. evaluated the role of oxygen vacancies in PrBaCo<sub>2</sub>O<sub>5+ $\delta$</sub>  toward

the OER.<sup>[70]</sup> They found that the intrinsic activity decreased with a large number of oxygen vacancies, which was attributed to a large reduction in the  $e_g$  filling of Co ions, the increased electrical resistivity, and the weakened Co–O bond covalency. Constructing a multi-metal system is an effective strategy by which to improve the activity and stability of catalysts.<sup>[71]</sup> In particular, the combination of Co and Fe can dramatically improve the electrocatalytic performance toward the OER, which has been confirmed in single perovskite oxides, spinel oxides, and alloys. Fabbri's group used operando X-ray absorption spectroscopy (XAS) technology to investigate the function of Fe in various types of Co-based perovskite oxides. In terms of PrBaCo<sub>2</sub>O<sub>6- $\delta$</sub> , the OER performance is enhanced with the introduction of Fe into the B-site (Figure 7e).<sup>[72]</sup> Operando XAS demonstrated that the oxidation states of Co ions in PrBaCo<sub>2(1-x)Fe<sub>x</sub>O<sub>6- $\delta$</sub>  were lower than those of PrBaCo<sub>2</sub>O<sub>6- $\delta$</sub> , which facilitates surface reconstruction with the generation of an (oxy)hydroxide layer (Figure 7f,g). PrBa<sub>0.5</sub>Sr<sub>0.5</sub>Co<sub>1.5</sub>Fe<sub>0.5</sub>O<sub>5+ $\delta$</sub>  (PBSCF) is a well-known triple conductivity material (H<sup>+</sup>/O<sup>2-</sup>/e<sup>-</sup>).<sup>[73]</sup> In addition to nanostructural engineering, Zhu et al. evaluated the effect of the crystal orientation on proton-coupled electron transfer processes and the OER activity.<sup>[74]</sup> PBSCF thin film samples with different orientations deposited on single crystal substrates were obtained by the pulsed laser deposition technique (Figure 7h). PBSCF follows the OER activity of a thin film at (100) > (110) > and (111). The proton diffusion path of the (100) surface exhibited energy-saving and fast reaction kinetics characteristics (Figure 7i,j). With the rational selection of the crystal orientation of the A-site ordered double perovskite, the OER activity can be effectively improved.</sub>

Although pure perovskite oxides show excellent OER activities, their HER activities are still not satisfactory due to their poor electrical conductivity, limited efficient active sites, and unfavorable hydrogen adsorption/desorption abilities.<sup>[75]</sup> To address these problems of perovskite oxides, substantial efforts have been devoted to the design of efficient HER electrocatalysts based on perovskite oxides.<sup>[75,76]</sup> Sun et al. evaluated the effect of the crystal structure on the HER activity.<sup>[77]</sup> The cubic single perovskite Pr<sub>0.5</sub>Ba<sub>0.5</sub>CoO<sub>3- $\delta$</sub>  (PBC-900 and PBC-1000), the orthorhombic double perovskite PrBaCo<sub>2</sub>O<sub>5+ $\delta$</sub>  ( $\delta = \approx 0.52$ , PBC-1100), and the tetragonal double perovskite PrBaCo<sub>2</sub>O<sub>5+ $\delta$</sub>  ( $\delta = \approx 0.76$ , PBC-1150) were synthesized by simply altering the annealing temperatures (Figure 8a). Impressively, PBC-1100 exhibited the best HER activities in terms of the mass activity, intrinsic activity, and overpotential at 10 mA cm<sup>-2</sup> (Figure 8b). The high levels of oxygen vacancies and lattice O<sup>2-</sup> and the highest O *p*-band center compared to other crystal structures were responsible for the outstanding HER activity of PBC-1100 (Figure 8c). Moreover, quite stable durability was observed in PBC-1100, as confirmed by the negligible activity degradation after the 1000th LSV test (Figure 8d). A moderate value of oxygen vacancies in PrBaCo<sub>2</sub>O<sub>6- $\delta$</sub>  coupled with the highest HER activity was also found in another work.<sup>[78]</sup> The oxygen deficiency site acts as a water-adsorption/dissociation site. Additionally, the higher valence state of the metal site facilitates the charge-transfer process owing to the stronger covalency between the transition metals and the adsorbed intermediates. Thus, any rational design of an ideal catalyst should take these factors into consideration.

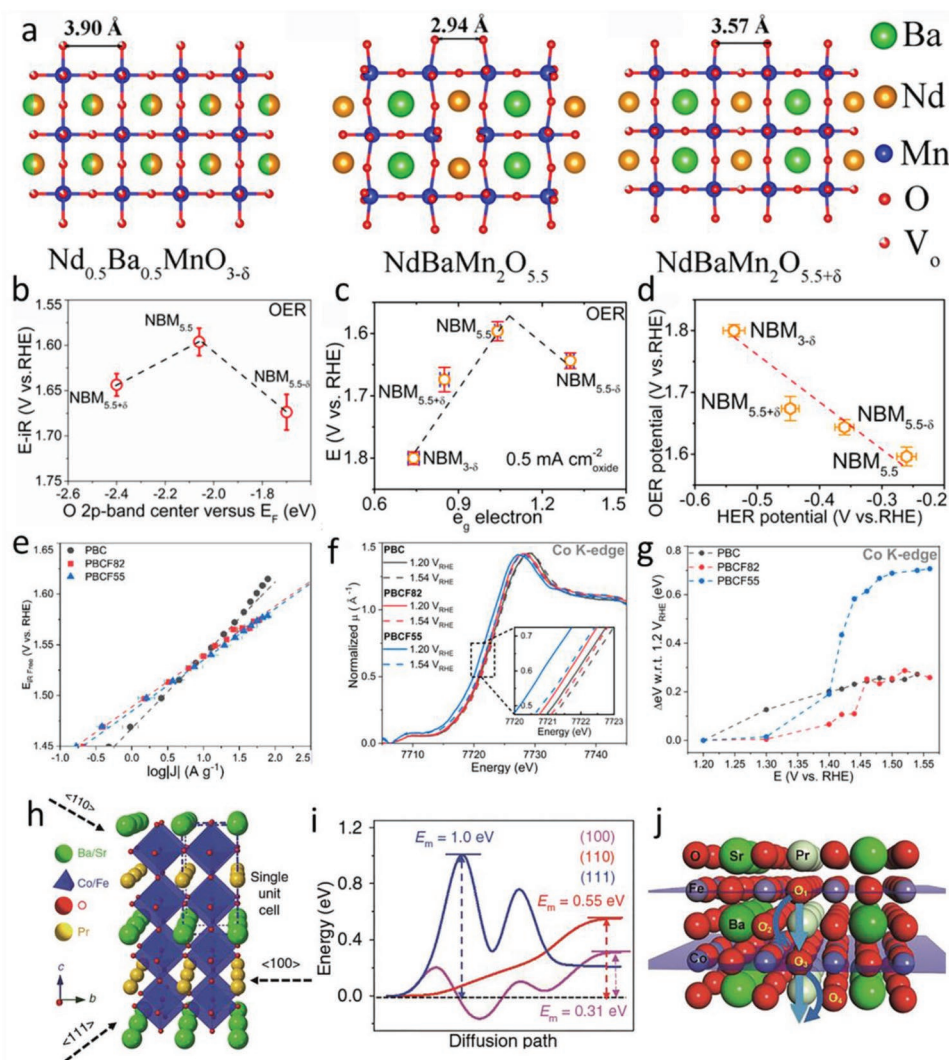


**Figure 7.** a) Projection along the [010] direction for  $\text{Nd}_{0.5}\text{Ba}_{0.5}\text{MnO}_{3-\delta}$ ,  $\text{NdBaMn}_2\text{O}_{5.5}$ , and  $\text{NdBaMn}_2\text{O}_{5.5+\delta}$ . b) Relationship between OER activity and the O 2p-band center versus the Fermi level. c) Relationship between the OER activity and the occupancy of the  $e_g$  orbit. d) Activity relationship between the OER and HER. Reproduced with permission.<sup>[67]</sup> Copyright 2018, American Chemical Society. e) Tafel plots of the OER activities. f) Operando XAS of the Co K-edge spectra collected at 1.2 and 1.54 V. g) Co K-edge energy shift compared to the edge position at 1.2 V during operando electrocatalytic tests of  $\text{PrBaCo}_2\text{O}_{6-\delta}$  (PBC),  $\text{PrBaCo}_{1.8}\text{Fe}_{0.2}\text{O}_{6-\delta}$  (PBCF82), and  $\text{PrBaCo}_{1.5}\text{Fe}_{0.5}\text{O}_{6-\delta}$  (PBCF55). Reproduced with permission.<sup>[72]</sup> Copyright 2019, MDPI. h) Crystal structure of PBSCF showing the different surface orientations of (100), (110), and (111). i) Energy profiles for proton diffusion in bulk PBSCF. j) Geometrical demonstration of oxygen and proton bulk diffusion in PBSCF along the (100) direction. Reproduced with permission.<sup>[74]</sup> Copyright 2020, Nature Publishing Group.

In particular, the structure of an A-site ordered double perovskite can simultaneously realize the ordering arrangement of oxygen vacancies and that of high-valence transition-metal cations. Specifically, oxygen vacancies and high-valence cations are located at pyramidal  $\text{Co}^{3+}$  sites and octahedral  $\text{Co}^{4+}$  sites, respectively. Benefiting from the layered structure along the c axis of the A-site ordered double perovskite, the oxygen vacancies also display an ordered configuration (Figure 8e).<sup>[79]</sup> DFT calculations also confirmed the active roles of these two sites (Figure 8f). As expected, the optimized  $(\text{Gd}_{0.5}\text{La}_{0.5})\text{BaCo}_2\text{O}_{5.75}$  ( $\delta=0.25$ ) exhibited the best HER performance among the series of  $\text{RBaCo}_2\text{O}_{5.5+\delta}$  electrocatalysts (Figure 8g). Subsequently, A-site ionic electronegativity was demonstrated as an effective descriptor to predict the HER activity based on the screening

of Co-based perovskite oxides.<sup>[76b]</sup>  $(\text{Gd}_{0.5}\text{La}_{0.5})\text{BaCo}_2\text{O}_{5.5+\delta}$  exhibited the highest HER activity with an A-site ionic electronegativity value of approximately 2.33, in which a volcano-type activity trend was successfully established (Figure 8h,i). This is due to the modulated electronic states of Co ions via an inductive effect between A-site and B-site cations bridged by O ions (Figure 8j).

## 5.2. Applications of B-Site Cation Ordered Double Perovskites

The ordered structure enables short reaction paths for the multistep OER process. Sun et al. was the first to present the B-site cation ordered double perovskite as a good candidate for

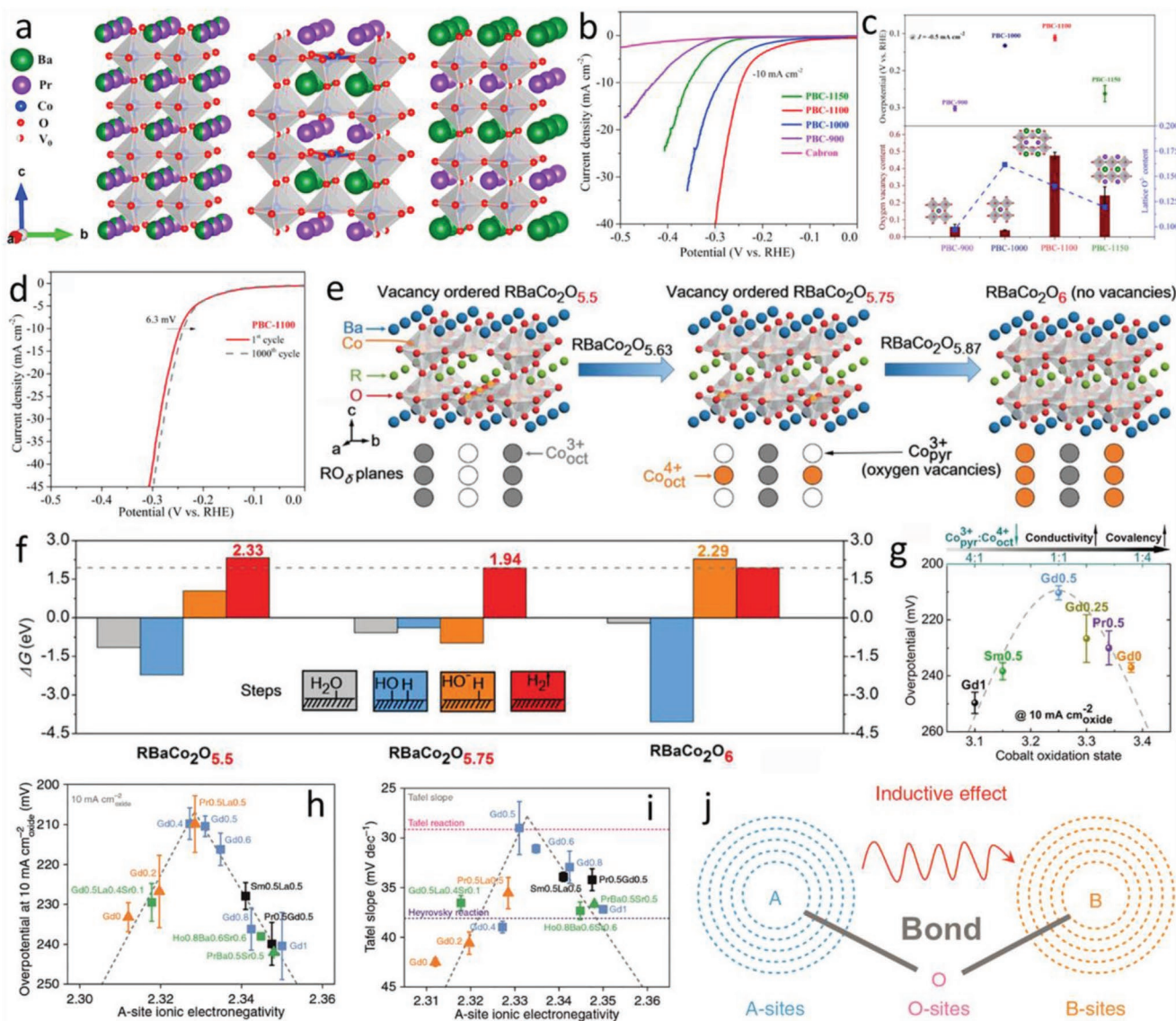


**Figure 8.** a) Schematic illustration of a single perovskite (disordered structure), an orthorhombic A-site ordered double perovskite, and a tetragonal A-site ordered double perovskite structure. b) LSV curves of PBC-900, PBC-1000, PBC-1100, and PBC-1150 toward HER. c) Dependence of the HER activity on the oxygen vacancy content and lattice oxygen content. d) LSV curves of the initial and 1000th of PBC-1100. Reproduced with permission.<sup>[77]</sup> Copyright 2019, Elsevier. e) Crystal structures of the  $\text{RbBaCo}_2\text{O}_{5.5}$  (oxygen vacancy ordered without high-valence metal sites) and  $\text{RbBaCo}_2\text{O}_{5.75}$  (oxygen vacancy ordered with high-valence metal sites), as well as,  $\text{RbBaCo}_2\text{O}_6$  (no oxygen vacancies). f) The calculated free energies for the HER steps on  $\text{RbBaCo}_2\text{O}_{5.5+\delta}$  surfaces ( $\delta = 0, 0.25, \text{ and } 0.5$ ). g) Volcano plot of the overpotential at the current density of  $10 \text{ mA cm}^{-2}$  as a function of Co valence state for the six studied electrocatalysts. Reproduced with permission.<sup>[79]</sup> Copyright 2020, Nature Publishing Group. h) HER activity trends of overpotential at  $10 \text{ mA cm}^{-2}$  and i) Tafel slope values as a function of A-site ionic electronegativity, respectively. j) Inductive effects and electron exchange interactions between A-sites and B-sites in perovskites from molecular orbital theory. Reproduced with permission.<sup>[76b]</sup> Copyright 2020, Nature Publishing Group.

the OER under alkaline media.<sup>[24c]</sup> Specifically, the presence of two types of cobalt local environments in  $\text{B}_2\text{Bi}_x\text{Sc}_{0.2}\text{Co}_{1.8-x}\text{O}_{6-\delta}$  greatly promoted the reaction kinetics, highlighting the critical role of the ordered structure (Figure 9a).  $\text{Sr}_2\text{FeMoO}_6$  is a classic half-metallic material with an ordered B-site ion arrangement (Figure 9b).<sup>[23a]</sup> Due to the lack of OER-active sites, as expected,  $\text{Sr}_2\text{FeMoO}_{6-\delta}$  (SFM) exhibited a high overpotential of 450 mV to obtain  $10 \text{ mA cm}^{-2}$ , suggesting unsatisfactory activity.<sup>[80]</sup> Notably, SFM endows fast OER kinetics revealed by its low Tafel slope, indicating the distinct advantage of the B-site

cation ordered structure for the OER process. However, a pure phase of SFM can only be synthesized in a reducing atmosphere with a high calcination temperature ( $>1200 \text{ }^\circ\text{C}$ ). Starting with SFM, the introduction of Ni and Co ions into the B'- and B''-sites can simultaneously tailor a calcined phase structure in an air atmosphere and introduce multiple-active sites. The as-synthesized  $\text{Sr}_2\text{Fe}_{0.8}\text{Co}_{0.2}\text{Mo}_{0.65}\text{Ni}_{0.35}\text{O}_{6-\delta}$  (SFCMN) retained the B-site cation ordered structure, as evidenced by the typical peaks of double perovskite at around  $19^\circ$  and  $38^\circ$  in the XRD (Figure 9c).<sup>[81]</sup> SFCMN exhibited a lower overpotential

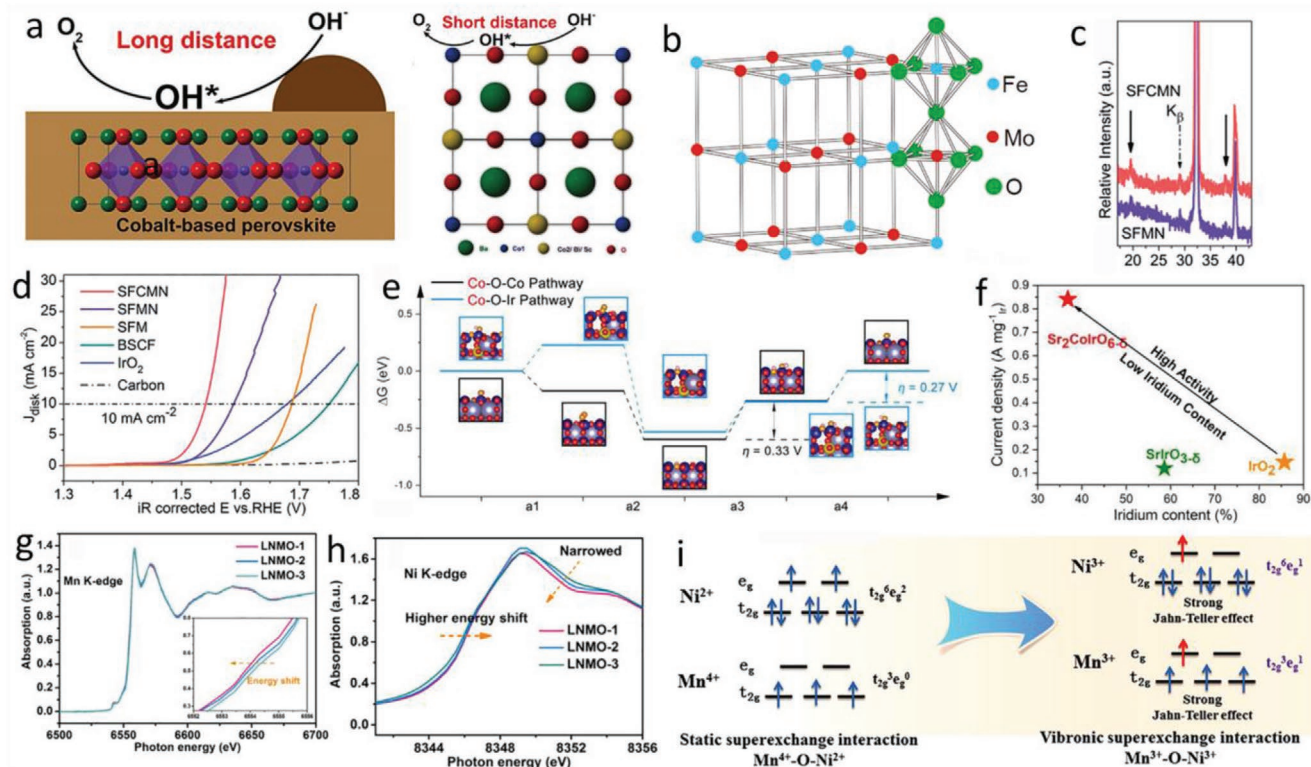


**Figure 9.** a) Schematic illustration of the reaction pathways on the B-site ordered double perovskite and single perovskite. Reproduced with permission.<sup>[24e]</sup> Copyright 2017, Wiley-VCH. b) A schematic diagram of  $\text{Sr}_2\text{FeMoO}_6$ . c) XRD patterns for the identification of the  $\text{A}_2\text{B}'\text{B}''\text{O}_6$  structure. d) LSV curves of SFM, SFMN, SFCMN, BSCF, and the noble metal oxide  $\text{IrO}_2$  toward the OER. Reproduced with permission.<sup>[81]</sup> Copyright 2019, Royal Society of Chemistry. e) The free energies at  $U_{\text{RHE}} = 1.23$  V of concerted proton-electron transfer OER steps; Regarding Co site of Co-O-Co pathway and Co-O-Ir pathway based on metal-and-lattice-oxygen-vacancy-site mechanism for  $\text{SrCoO}_{2.625}$ . f) Comparison of iridium mass activities of  $\text{Sr}_2\text{CoIrO}_{6-\delta}$ ,  $\text{SrIrO}_{3-\delta}$  and  $\text{IrO}_2$  at an overpotential of 300 mV. Reproduced with permission.<sup>[45]</sup> Copyright 2021, Wiley-VCH. g) Mn and h) Ni K-edge XANES spectra of various  $\text{La}_2\text{NiMnO}_{6-\delta}$  (LNM) samples. i) Superexchange process in the  $\text{A}_2\text{B}'\text{B}''\text{O}_6$  structure. Reproduced with permission.<sup>[84]</sup> Copyright 2018, American Chemical Society.

of 310 mV corresponding to  $10 \text{ mA cm}^{-2}$  compared to those of the parent oxide SFM (450 mV), the benchmark OER catalyst for perovskite oxide BSCF with a single perovskite structure (510 mV), and the noble metal oxide  $\text{IrO}_2$  (450 mV) (Figure 9d). Different from SFM,  $\text{Sr}_2\text{FeMo}_{0.65}\text{Ni}_{0.35}\text{O}_{6-\delta}$  (SFMN), and  $\text{Sr}_2\text{Fe}_{1.3}\text{Ni}_{0.2}\text{Mo}_{0.5}\text{O}_{6-\delta}$  with a low ordering of B-site atoms,  $\text{Sr}_2\text{CoIrO}_{6-\delta}$  exhibits a highly ordered arrangement of B-site ions, as reflected by the strong peak intensity for identifying the double perovskite.<sup>[23b]</sup> Both Co and Ir are highly active in the OER process and the O-bridged Co-O-Ir pathway has a great contribution to a synergistic effect (Figure 9e).<sup>[45]</sup> Moreover, unlike the synergistic interplay from the interfaces, such as for heterostructures and core-shell structures, this type of structurally ordered material enables an ideal condition to fully realize synergistic effects. The electrocatalytic activity of  $\text{Sr}_2\text{CoIrO}_{6-\delta}$  in the alkaline solution ranks the highest performance among solid-state catalysts (Figure 9f).

First-row transition-metal-based B-site ordered double perovskites are also promising candidates for electrocatalysis. Ahmed et al. synthesized  $\text{La}_2\text{NiMnO}_6$  nanoparticles that were ferromagnetic in nature.<sup>[82]</sup>  $\text{La}_2\text{NiMnO}_6$  nanoparticles showed superior OER activity. Additionally, to build the relationship between the catalytic activity and the complex spin configuration of the perovskite, Jiang et al. selected  $\text{La}_2\text{NiMnO}_{6-\delta}$  and  $\text{La}_2\text{CoMnO}_{6-\delta}$  as model catalysts.<sup>[83]</sup> Their experimental results revealed that

double perovskites exhibited bifunctional catalytic properties toward the OER and ORR in alkaline solutions. Furthermore, for the system of  $\text{La}_2\text{CoMnO}_{6-\delta}$ , the average  $e_g$  orbital occupation numbers based on both Co and Mn ions could explain the electrocatalytic activities of  $\text{La}_2\text{CoMnO}_{6-\delta}$  catalysts. Meanwhile, the average deviation of the  $e_g$  filling number of each ion from unity was proposed to explain  $\text{La}_2\text{NiMnO}_{6-\delta}$  catalysts, which have unity average  $e_g$ -filling. Tong et al. highlighted the vibronic superexchange in  $\text{La}_2\text{NiMnO}_{6-\delta}$  for enhanced OER activity.<sup>[84]</sup> The superexchange effect brings about the d electron configuration in B-site transition cations from a  $\text{Ni}^{2+}\text{-O-Mn}^{4+}$  static superexchange effect to a  $\text{Ni}^{3+}\text{-O-Mn}^{3+}$  vibronic superexchange effect (Figure 9g-i). As a result,  $\text{La}_2\text{NiMnO}_{6-\delta}$  nanoparticles exhibit improved OER activity relative to their bulk counterpart. To further enhance the bifunctional activities of the  $\text{La}_2\text{NiMnO}_6$ -based double perovskite, Sr and Ru were introduced, resulting in the compositional formula of  $\text{La}_{1.5}\text{Sr}_{0.5}\text{NiMn}_{0.5}\text{Ru}_{0.5}\text{O}_6$ .<sup>[85]</sup> XRD analysis was performed to determine the positions of Ni, Mn, and Ru in the B'/B'' sublattices, obtaining the precise formula of  $(\text{La}_{1.5}\text{Sr}_{0.5})_{\text{A}}(\text{Ni}_{0.5}\text{Mn}_{0.5})_{\text{B}'}(\text{Ni}_{0.5}\text{Ru}_{0.5})_{\text{B}''}\text{O}_6$  (LSNMR). X-ray absorption near-edge spectroscopy data revealed multi-metal sites, including  $\approx\text{Ni}^{2+}$ ,  $\approx\text{Mn}^{4+}$  (average oxidation state of  $\text{Mn}^{3.7+}$ ), and  $\approx\text{Ru}^{5+}$  in LSNMR. Further, DFT calculations demonstrated that the Mn sites and Ru sites are highly active ORR and OER sites, respectively.

### 5.3. Applications of Quadruple Perovskites

Fe<sup>4+</sup>-based single perovskite oxides, such as, SrFeO<sub>3</sub> and CaFeO<sub>3</sub>, are expected to exhibit high OER catalytic activity due to the  $t_{2g}^1 e_g^1$  configuration of high-spin Fe<sup>4+</sup> ions.<sup>[86]</sup> However, under experimental testing, the activity and stability of these materials are not satisfactory, mainly due to the unstable structure in electrochemical conditions. Yagi et al. reported that Fe<sup>4+</sup>-based quadruple perovskite CaCu<sub>3</sub>Fe<sub>4</sub>O<sub>12</sub> displayed comparable or superior OER activity to BSCF and RuO<sub>2</sub> under alkaline solutions.<sup>[86c]</sup> The enhanced activity and operating stability were attributed to the improved structural stability associated

with the presence of a covalent bonding network that incorporates Cu<sup>2+</sup> and Fe<sup>4+</sup> transition-metal ions. (Figure 10a–c) The same group later presented a systematic study of the OER activities of quadruple perovskite oxides and single perovskites (Figure 10d,e).<sup>[87]</sup> Electrochemical measurements revealed that the OER activities of CaCu<sub>3</sub>B<sub>4</sub>O<sub>12</sub> (B = Ti, V, Cr, Mn, Fe, and Co) exceed those of the single perovskite CaBO<sub>3</sub> (Figure 10f) in all cases. Notably, the activity order of B-site transition-metal ions for quadruple perovskite oxides follows the trend of the single perovskite oxide of CaBO<sub>3</sub>, suggesting that B-site ions take on a primary role, whereas A'-site Cu ions secondarily facilitate the OER activity for the quadruple perovskite oxide CaCu<sub>3</sub>B<sub>4</sub>O<sub>12</sub>.

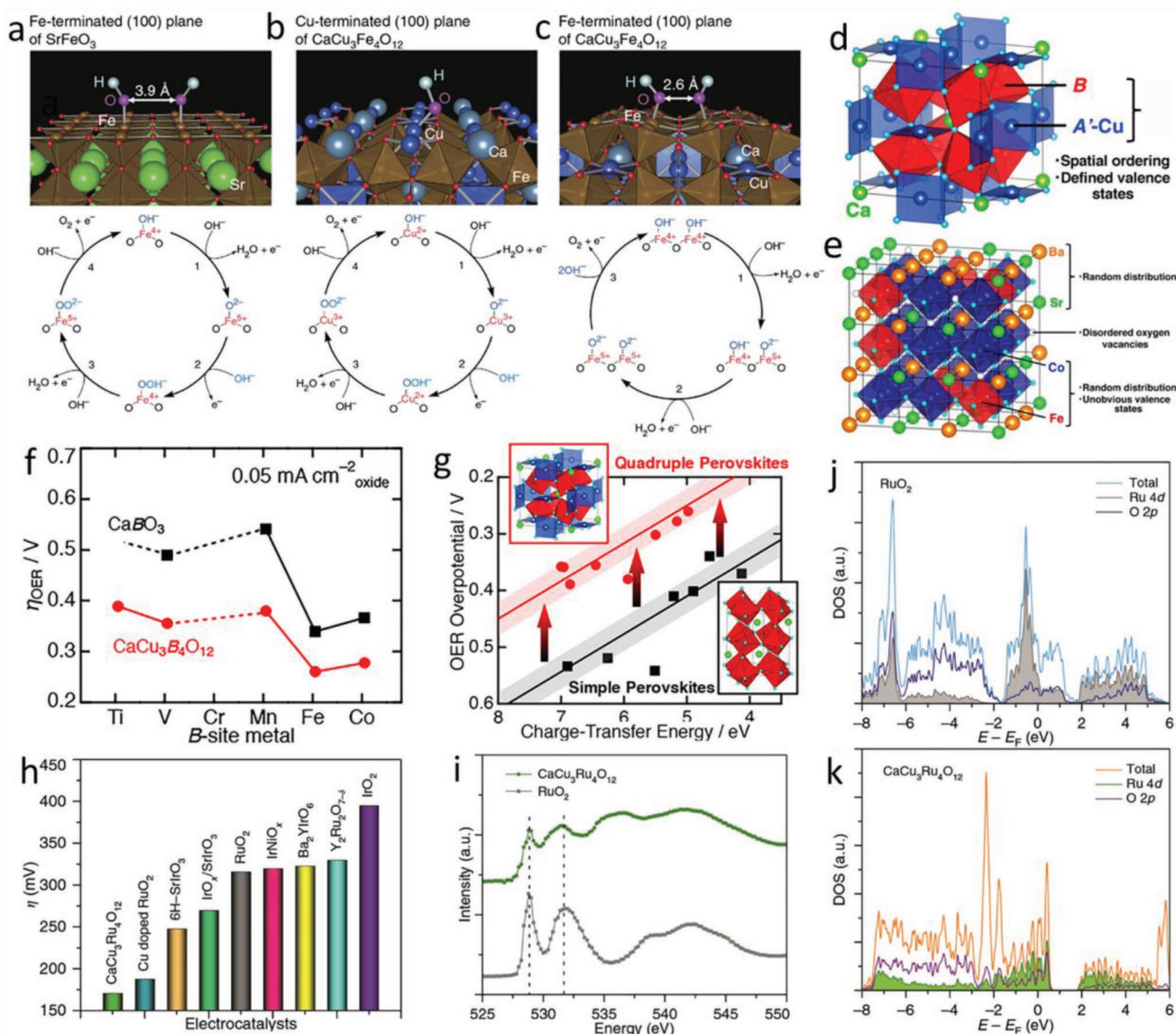


**Figure 10.** a–c) OH<sup>-</sup> adsorbed surfaces for SrFeO<sub>3</sub> and CaCu<sub>3</sub>Fe<sub>4</sub>O<sub>12</sub> and corresponding OER mechanism. Reproduced with permission.<sup>[86c]</sup> Copyright 2015, Nature Publishing Group. d) Crystal structure of quadruple CaCu<sub>3</sub>B<sub>4</sub>O<sub>12</sub>. e) Crystal structure of BSCF as a representative sample of a structurally disordered perovskite oxide. f) OER activities for single perovskite oxides CaBO<sub>3</sub> and quadruple perovskite CaCu<sub>3</sub>B<sub>4</sub>O<sub>12</sub>. g) OER overpotentials as a function of the charge-transfer energy for single perovskite oxides and quadruple perovskite oxides. Reproduced with permission.<sup>[87]</sup> Copyright 2018, American Chemical Society. h) Comparison of the overpotential for CaCu<sub>3</sub>Ru<sub>4</sub>O<sub>12</sub> and state-of-the-art OER electrocatalysts in acidic media. i) O K-edge soft XAS spectra of CaCu<sub>3</sub>Ru<sub>4</sub>O<sub>12</sub> and RuO<sub>2</sub>. Computed density of states of j) RuO<sub>2</sub> and k) CaCu<sub>3</sub>Ru<sub>4</sub>O<sub>12</sub>. Reproduced with permission.<sup>[89]</sup> Copyright 2019, Nature Publishing Group.

The charge-transfer energies (Figure 10g) and energy differences between the O  $2p$  band center and the unoccupied  $3d$  band center of the B-site metals explained the decreased overpotentials of quadruple perovskite oxides compared to single perovskite oxides. The strong covalence bonding effect was also confirmed by the  $Ti^{4+}$ -based quadruple perovskite  $CaCu_3Ti_4O_{12}$ , which served as a bifunctional electrocatalyst for the OER and ORR in an alkaline solution.<sup>[88]</sup>

Of note, early first-row transition-metal-based oxides are conventionally regarded as less active for the OER or ORR.<sup>[5b]</sup> Meanwhile, late first-row transition-metal-based quadruple perovskite oxides are not able to survive in strongly acidic media. As a case to highlight the advantage of the quadruple perovskite structure, Miao et al. reported that the quadruple perovskite  $CaCu_3Ru_4O_{12}$  exhibited a low overpotential of 171 mV to reach  $10\text{ mA cm}^{-2}$  in acidic media, much lower than that of  $RuO_2$  (316 mV) and other state-of-the-art electrocatalysts (Figure 10h).<sup>[89]</sup> The outstanding activity was attributed to the unique quadruple perovskite structure with a lower Ru  $4d$ -band center compared to  $RuO_2$  that could provide optimized binding energy of the oxygen intermediate for the OER process (Figure 10i–k).

## 5.4. Applications of Intermetallics

### 5.4.1. Applications of Noble Metal-Based Intermetallics

*Oxygen Reduction Reaction Catalysts in an Acidic Electrolyte:* Carbon-supported Pt-based materials (e.g., Pt and Pt-alloy) are currently commercial cathode materials of proton-exchange membrane fuel cells due to their high ORR performance in acidic and oxidizing environments. Alloy/dealloying, thin Pt shells on core structures, and fabricating ordered intermetallic Pt-M (M = first-row transition-metals) are state-of-the-art strategies to reduce the Pt loading while still improving the ORR activity.<sup>[105]</sup> The defined crystal structure and stoichiometry of intermetallic have received increasing attention.<sup>[9d,106]</sup> A cubic ordered  $L1_2$  phase, such as,  $Pt_3Co$ ,  $Pt_3Cr$ , and a tetragonal ordered  $L1_0$  phase, such as,  $PtCo$  and  $Pt$ , reportedly exhibit markedly enhanced ORR performance compared to the corresponding disordered alloy phase. For example,  $PtCu$  shows a drastic structural change from an alloy into the rhombohedral  $L1_1$  intermetallic structure during the disorder-to-order transformation (Figure 11a).<sup>[107]</sup> As expected, intermetallic  $PtCu$  with a nanoframe structure exhibits a larger value of electrochemically active surface area (Figure 11b) and a higher half-wave potential ( $E_{1/2}$ ) compared to those of  $Pt/C$  and disordered  $PtCu$  alloy (Figure 11c). Gan et al. presented a systematic evaluation of the structural features and ORR catalytic capabilities of  $PtM_3$  (M = Fe, Co, and Ni) low-Pt ordered intermetallic nanoparticulate catalysts.<sup>[108]</sup> Notably, after high-temperature thermal annealing ( $600\text{ }^\circ\text{C}$  in  $H_2/Ar$  for 4 h), only the  $PtCo_3$  and  $PtFe_3$  catalysts show an ordered structure (Figure 11d). Moreover, the surface of the ordered  $PtCo_3$  was coated with in situ-uniformed thin Pt shell ( $\approx 0.6\text{ nm}$ ), which is crucial to protect the transition-metal Co during the harsh reaction conditions (Figure 11e). This work highlights the importance of both structural control and particle sintering behavior with regard to the overall

performance. Additionally, anion doping has been demonstrated as an effective strategy to introduce ligand and strain effects in intermetallic PtM catalysts.<sup>[109]</sup> The formation of stable M-N bonding and the modulation of the adsorption energetics of oxygenated species on the Pt surface will lead to further improved ORR performance.<sup>[110]</sup> Recently, Zhao et al. synthesized intermetallic  $PtCuN$  ( $L1_1$ -ordered phase) supported on Ketjenblack (Int- $PtCuN/KB$ ) (Figure 11f). Int- $PtCuN/KB$  exhibited higher ORR performance than that of Int- $PtCu/KB$ .<sup>[105a]</sup> Impressively, Int- $PtCuN/KB$  showed improvements by 5.2 and 3.9 times in terms of the mass activity and intrinsic activity, respectively, compared to those of commercial  $Pt/C$  (Figure 11g). Good operational stability was demonstrated by mass activity attenuation of only 23.4% after 20 000 accelerated durability test cycles (Figure 11h). Such outstanding ORR performance can be attributed to synergistic effects caused by several factors, including unique ordered structure and the compressive strain through N-doping, which benefit the adsorption of intermediates on the Pt surface. The presence of the Pt monolayer shell effectively decreases Cu leaching under the reaction conditions. Moreover, the formation of Cu–N bonds and intermetallic ordering also effectively alleviates Cu dissolution from the core (Figure 11i,j).

In addition to bimetallic alloys, considerable efforts have been devoted to designing ternary alloys, especially structurally ordered intermetallic materials.<sup>[111]</sup> Too many elements would increase the challenges of forming an ordered structure due to the difficulty related to explicitly establishing the effects of every element. Wang et al. found that the incorporation of Ni in intermetallic  $PtCu$  can effectively tune the electronic structure of Pt, which contributes to the impressive ORR activity and stability.<sup>[111]</sup> Wang's group found that the introduction of Cu ( $PtFe_xCu_{1-x}$  alloys) enabled the formation of an ordered body-centered tetragonal- $PtFe$  phase based on the parent disordered face-centered cubic- $PtFe$  phase at low annealing temperatures.<sup>[112]</sup> The concentration of Cu has a significant effect on the particle size distribution, lattice strain, and Fe dissolution behavior, which are all crucial factors that determine the activity and durability (Figure 11k). The optimal Cu concentration ( $PtFe_{0.7}Cu_{0.3}$ ) gave the best durability performance. Notably, a high concentration of Cu (e.g.,  $PtFe_{0.5}Cu_{0.5}$ ) would destroy the ordered structure and lead to the leaching of Fe and a loss of durability. Although the introduction of smaller Cu atoms sacrificed the activity toward methanol oxidation, the rationally designed composition also led to considerably enhanced stability behavior. Therefore, this work presented a strategic method to design a ternary alloy beyond the application of methanol oxidation.

*Oxygen Reduction Reaction Catalysts in an Alkaline Electrolyte:* Meanwhile, carbon-supported Pt materials, such as, commercial  $Pt/C$ , are the benchmark catalysts for the ORR in alkaline solutions, which is the key reaction for metal-air batteries. Developing Pt-free materials with high ORR performance is also the key to reducing the cost of the battery devices. Pd also exhibits high ORR activity comparable to that of Pt. Pd-based ordered intermetallic materials not only exhibit high ORR activity but also show high corrosion resistance under alkaline reaction conditions (lowering the leaching of 3d transition metals).<sup>[9c]</sup> As a case to highlight the advantage of this ordered structure, Yang et al. utilized Au incorporation in an ordered

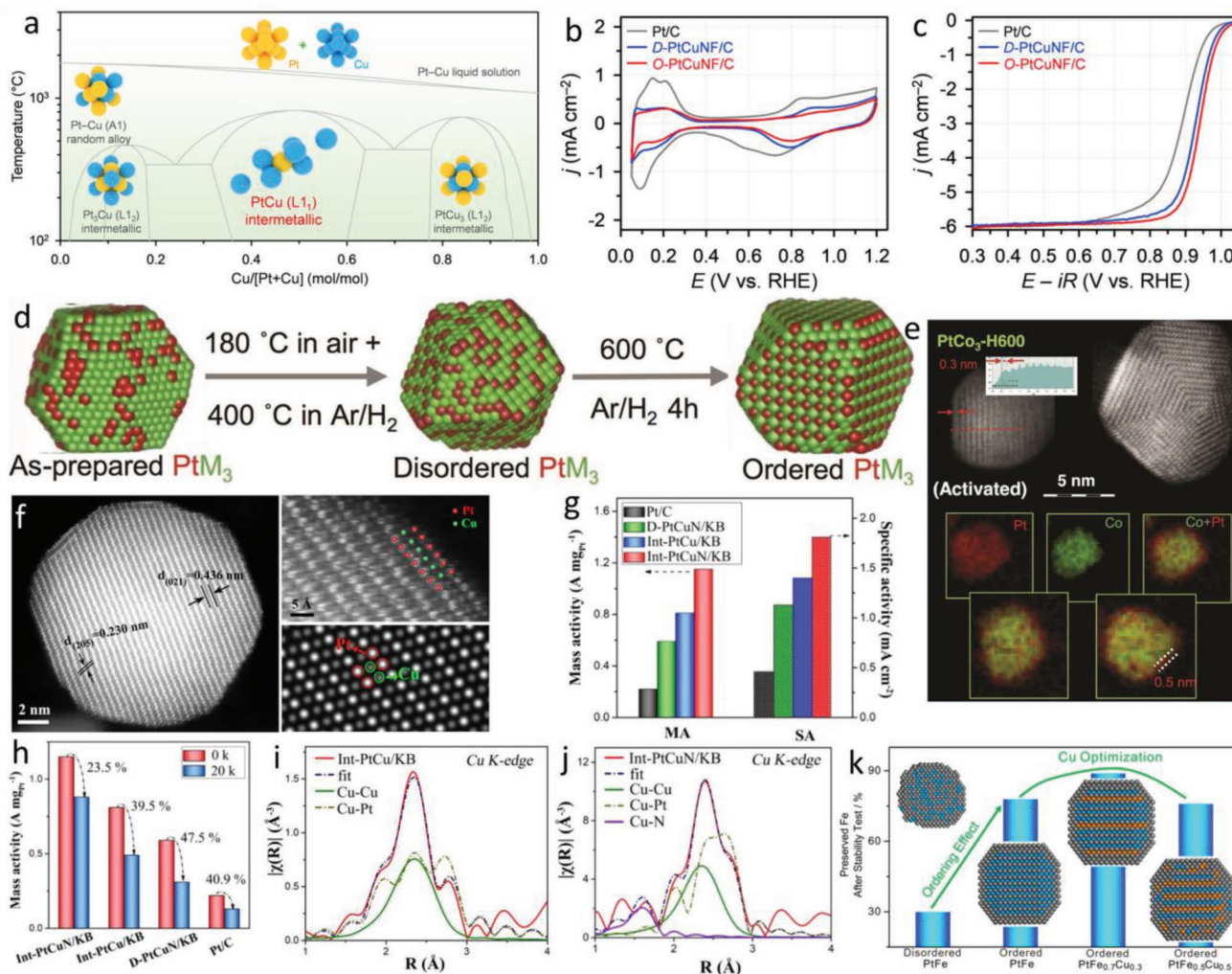


**Figure 11.** a) Pt-Cu phase diagram. b) CV curves and c) ORR LSV curves of Pt/C, D-PtCuNF/C, and O-PtCuNF/C. Reproduced with permission.<sup>[107]</sup> Copyright 2020, American Chemical Society. d) Schematic illustration of the synthesis process of PtM<sub>3</sub> (M = Fe, Co, and Ni) intermetallic catalysts. e) High-resolution STEM images and EELS mapping of the activated ordered PtCo<sub>3</sub>-H600 catalyst. Reproduced with permission.<sup>[108]</sup> Copyright 2019, Wiley-VCH. f) Observed and simulated atomic-resolution HAADF-STEM images of PtCu intermetallic particles. g) Specific activity and mass activity of Int-PtCuN/KB, Int-PtCu/KB, D-PtCuN/KB, and commercial Pt/C at 0.9 V. h) Mass activity comparison of these samples before and after 20 000 cycles. In situ Cu K-edge FT-EXAFS spectra at 0.42 V of i) Int-PtCu/KB and j) Int-PtCuN/KB. Reproduced with permission.<sup>[105a]</sup> Copyright 2021, American Chemical Society. k) The relationship between phase structures of ternary-ordered intermetallic and operational stability. Reproduced with permission.<sup>[112]</sup> Copyright 2018, American Chemical Society.

intermetallic PdZn/C with several atomic-layer Pd shells (Au-O-PdZn/C), showing remarkable durability with less than 10% loss in the mass activity, after even 30 000 potential cycles (Figure 12a,b).<sup>[113]</sup> In detail, ordered intermetallic PdZn/C can be obtained by a post-annealing treatment of disordered PdZn, which was synthesized by an impregnation method. The ordered structure was identified by the emergence of the characteristic (001) and (100) peaks of an ordered intermetallic phase. Then, partially Pd and Zn were replaced by Au atoms through a galvanic replacement method, which is able to retain the ordered structure, as confirmed by XRD and bright-field high-resolution transmission electron microscopy imaging. Benefiting from this unique structure, the high ORR activity and durability of Au-O-PdZn/C enable its application in Zn-air batteries and Li-air batteries. Moreover, the synthesis of inter-

metallic Pd<sub>3</sub>Pb nanocubes with shape-controlled nanoparticles was reported (Figure 12c,d).<sup>[114]</sup> DFT calculations suggest that the high ORR activity of Pd<sub>3</sub>Pb was ascribed to a weakening in the binding energy of OH\* when compared to the Pd/C (Figure 12e,f).

Developing effective and universal strategies that can rapidly prepare intermetallic ultra-porous nanosheets with a tunable size is a necessity. Very recently, Guo et al. presented a universal template-directed synthesis method capable of bypassing the conventional time-consuming and high-temperature synthetic route (Figure 12g).<sup>[115]</sup> The use of preformed seeds is the key to control the deposition of atoms and the subsequent interatomic diffusion (Figure 12g). The atomic ordered arrangement was well demonstrated by the atomic-resolution HAADF-STEM images (Figure 12h,i). Particularly, the specific activity and mass activity

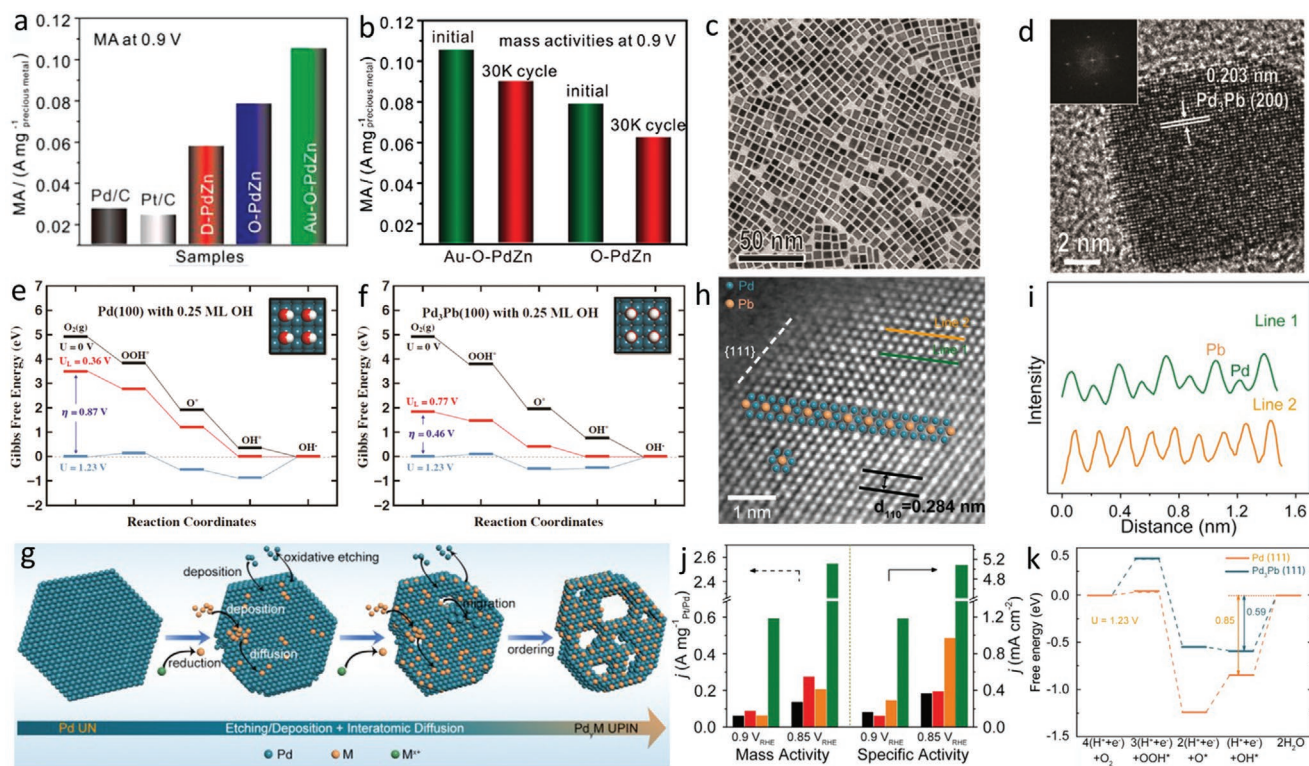


**Figure 12.** a) Initial mass activities of the studied catalysts at 0.9 V. b) Mass activities before and after 30 000 CV cycles. Reproduced with permission.<sup>[113]</sup> Copyright 2019, American Chemical Society. c) TEM and d) HRTEM images of Pd<sub>3</sub>Pb nanocubes. Plots of Gibbs free energy versus the reaction pathway for e) Pd(100) and f) Pd<sub>3</sub>Pb(100) surface. Reproduced with permission.<sup>[114]</sup> Copyright 2020, Royal Society of Chemistry. g) Schematic illustration of the fabrication process of Pd<sub>3</sub>Pb ultrathin porous intermetallic nanosheets by a template-directed strategy. h) Atomic-resolution aberration-corrected HAADF-STEM image of intermetallic Pd<sub>3</sub>Pb. i) The intensity profiles taken along the olive and orange lines in (h). j) LSV curves of commercial Pd/C, Pt/C, Pd ultrathin nanosheets/C and Pd<sub>3</sub>Pb ultrathin porous intermetallic nanosheets/C catalysts toward the ORR. k) Free energy diagrams of Pd<sub>3</sub>Pb (111) and Pd (111) slabs at a potential of 1.23 V toward the ORR. Reproduced with permission.<sup>[115]</sup> Copyright 2021, Wiley-VCH.

of intermetallic Pd<sub>3</sub>Pb/C were 9.8-fold and 6.8-fold higher, respectively, than those of Pt/C toward the ORR in alkaline solutions (Figure 12j). DFT calculations revealed that the rate-limiting step of the ORR is the OH\* → H<sub>2</sub>O (liquid) step for both Pd<sub>3</sub>Pb (111) and Pd (111). However, the corresponding overpotential was 0.59 V, much lower than that of Pd (111) (0.85 V) (Figure 12k).

**Hydrogen Evolution Reaction Catalysts in an Alkaline Electrolyte:** Similarly, Pt-based materials are also benchmark cathodic materials for polymer electrolyte membrane electrolyzers. However, the HER activity of Pt under alkaline conditions is approximately two to three orders of magnitude lower than that in acidic conditions due to the slow HER kinetics in alkaline media (e.g., the poor H<sub>2</sub>O dissociation ability of Pt). Developing alternative materials with high-performance in alkaline media to Pt-based catalysts remains a great challenge.<sup>[75,116]</sup> An effective strategy is to introduce oxophilic metals or metal (hydr)oxide to improve the ability of water dissociation and to facilitate the formation of hydrogen intermediates. Furthermore, precise structural control at the atomic level can realize the synergistic interplay of two nearby active centers. Based on these considerations, as well as, guidelines from previous works, Chen et al. was the first to develop Ir-based ordered alloy electrocatalysts for the alkaline HER.<sup>[16b]</sup> The oxophilic metal V with relative high metal-OH bond strength capabilities was selected to form an intermetallic structure with Ir (Figure 13a,b). Benefitting from the ordered structure, the carbon-supported

Ir<sub>3</sub>V-1000 (ordered structure) electrocatalyst exhibits a lower overpotential (9.0 mV) at 10 mA cm<sup>-2</sup> compared to those of the benchmarks Pt/C (54.0 mV), Ir<sub>3</sub>V-1000 (30.9 mV, cation disordered structure) and Ir/C (50.0 mV) (Figure 13c). Importantly, there is no obvious structural and electronic change of Ir<sub>3</sub>V-1000 after the HER process, confirming its high operational stability toward the HER. DFT calculations revealed that the oxophilic V sites in the alloy can effectively promote the ability of water dissociation. This is ascribed to the charge redistribution on the intermetallic Ir<sub>3</sub>V surface (Figure 13d). Ji et al. systematically evaluated the effect of lanthanide contraction on the HER activity of Re<sub>2</sub>Co<sub>17</sub> (Re = Y, Pr, Gd, Tb, Ho, and Er) intermetallics (Figure 13e).<sup>[117]</sup> They found that the averaged Co–Co bond length is the key factor that determines the HER activities (Figure 13f–h). This work highlights the rational selection of rare-earth metals and lanthanide contraction to tailor the interatomic spacing and the corresponding HER activity.

**Hydrogen Evolution Reaction Catalysts in an Acidic Electrolyte:** The alloying effects can also be extended to the HER in acidic electrolytes. For example, the introduction of 3d transition-metal Cu can effectively regulate the hydrogen binding energy, especially for the compressed intermetallic PdCu with B2 phase (PdCu-B2). Intermetallic PdCu-B2 with the nanowire structure exhibits a superior HER activity in acidic media (Figure 13i,j).<sup>[118]</sup> Generally, a high temperature annealing treatment is required to induce the phase transition from a disordered structure to an ordered

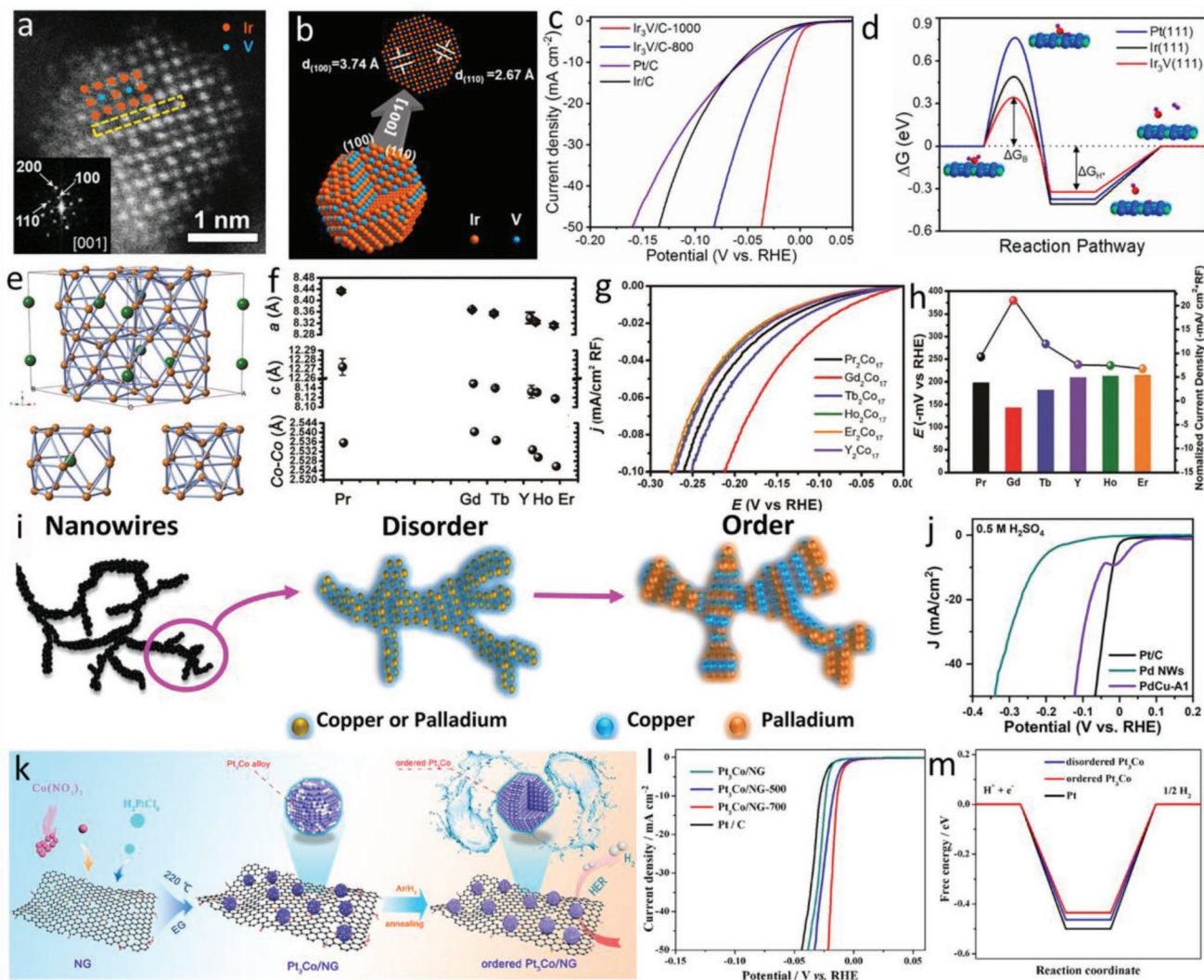


**Figure 13.** a) Atomic resolution HAADF-STEM image of Ir<sub>3</sub>V/C-1000. b) Structural illustration of intermetallic Ir<sub>3</sub>V nanoparticles. c) LSV curves of Ir<sub>3</sub>V/C-1000, Ir<sub>3</sub>V/C-800, Ir/C, and Pt/C toward the HER in alkaline media. d) Gibbs free energy diagram of Pt (111), Ir (111), and Ir<sub>3</sub>V (111) surfaces toward the HER process. Reproduced with permission.<sup>[16b]</sup> Copyright 2021, Elsevier. e) A ball-stick representation of the crystal structure of intermetallic Gd<sub>2</sub>Co<sub>17</sub>. f) Refined lattice constants and averaged Co–Co bond distances of RE<sub>2</sub>Co<sub>17</sub>. g) Roughness factor normalized LSV curves of RE<sub>2</sub>Co<sub>17</sub>. h) HER activity comparison diagram of RE<sub>2</sub>Co<sub>17</sub>. (Re = Y, Pr, Gd, Tb, Ho, and Er). Reproduced with permission.<sup>[117]</sup> Copyright 2020, Royal Society of Chemistry. i) Scheme for synthesis of the PdCu (A1 phase) nanowire network and its transformation to design PdCu (B2 phase) nanowires. j) LSV curves of Pt/C, Pd nanowires, and PdCu (A1 phase) toward the HER in acid media. Reproduced with permission.<sup>[118]</sup> Copyright 2020, American Chemical Society. k) Schematic illustration of the fabrication process of Pt<sub>3</sub>Co nanoparticles on N-doped graphene. l) LSV curves toward the HER in acidic media. m) Free energy diagram toward the HER process of Pt<sub>3</sub>Co/NG-700, Pt<sub>3</sub>Co/NG-500, Pt<sub>3</sub>Co/NG, and Pt/C. Reproduced with permission.<sup>[119]</sup> Copyright 2020, American Chemical Society.

structure. To avoid particle sintering during the annealing treatment, Lin et al. introduced nitrogen-doped graphene (NG) as a support to anchor ordered Pt<sub>3</sub>Co nanoparticles.<sup>[119]</sup> Moreover, the support can provide anchoring sites for modulating the particle size and uniform dispersion of the nanoparticles (Figure 13k). Meanwhile, the metal-support interaction can further improve the electrocatalytic activity and stability. Thus, intermetallic Pt<sub>3</sub>Co nanoparticles anchored on NG exhibit an ultra-small overpotential of 13 mV at 10 mA cm<sup>-2</sup> and remarkably high mass activity of 9.33 A mg<sup>-1</sup> at an overpotential of 20 mV, which is more than 50-fold higher than that of the Pt/C catalyst (Figure 13l). The advantages of the ordered structure were demonstrated by

DFT calculations, revealing that the ordered structure endows the optimum adsorption and dissociation abilities for H\* and exhibits better conductivity and higher electron transfer capabilities compared to the disordered one (Figure 13m).

#### 5.4.2. Applications of Transition-Metal-Based Intermetallics

*Oxygen Evolution Reaction Catalysts in an Alkaline Electrolyte:* Compared to a disordered alloy, an ordered intermetallic structure provides uniform active sites on the same surface plane. Therefore, transition-metal-based intermetallics with a

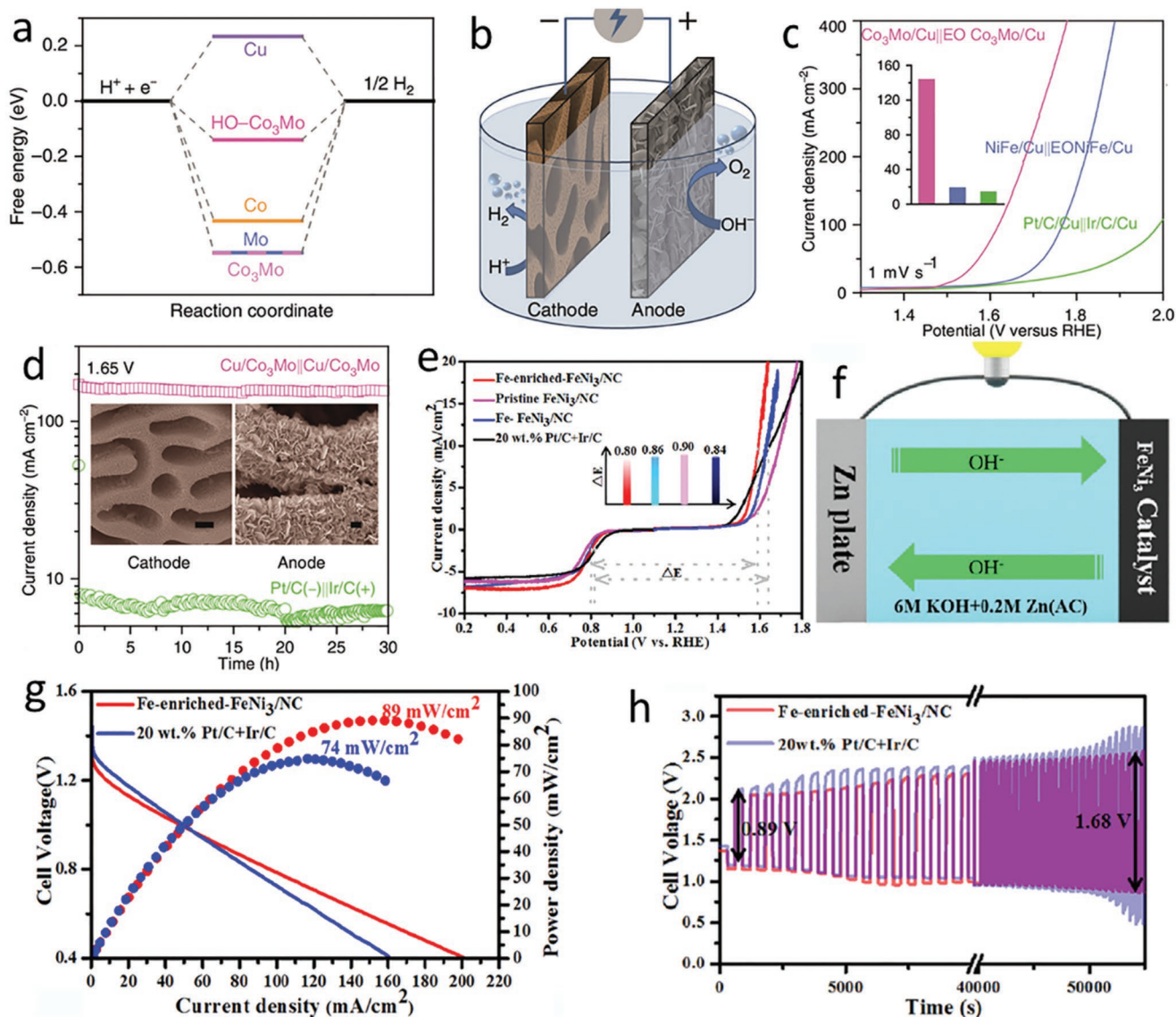


**Figure 14.** a) Free-energy diagram of hydrogen adsorption on HO-Co<sub>3</sub>Mo, pure Cu, Co, Mo, and Co<sub>3</sub>Mo surfaces. b) Schematic illustration of the overall alkaline water electrolyzer device. c) Polarization curves of overall water electrolysis in 1 M KOH and 0.5 M NaCl. d) Durability measurement of the electrolyzer at 1.65 V. Reproduced with permission.<sup>[121]</sup> Copyright 2020, Nature Publishing Group. e) The overall polarization curves of pristine FeNi<sub>3</sub>/NC, Fe-FeNi<sub>3</sub>/NC, Fe-enriched-FeNi<sub>3</sub>/NC and commercial 20 wt% Pt/C + Ir/C within the ORR and OER potential window. f) Schematic illustration of Zn-air battery. g) The discharge polarization curves and the corresponding power density curves of the Zn-air battery. h) Galvanostatic discharge-charge cycling curves of Pt/C + Ir/C- and Fe-enriched-FeNi<sub>3</sub>/NC-based batteries at 10 mA cm<sup>-2</sup>. Reproduced with permission.<sup>[122]</sup> Copyright 2020, Elsevier.

tuned size, structure, and composition are also good candidates for the OER in alkaline media.<sup>[4a,11f]</sup> Samanta et al. presented intermetallic NiZn, which shows better OER activity than that of the Ni<sub>0.7</sub>Zn<sub>0.3</sub> alloy, along with pure Ni nanoparticles and noble metal RuO<sub>2</sub>.<sup>[120]</sup> The introduction of Zn atoms into nanocrystalline Ni led to a dramatically increased number of available surface active sites, intrinsic activity, and a possible synergistic effect between the two transition metals. Additionally, the charge transfer from Ni to Zn further made Ni the active center and Ni a promoter in the alloy structure during the electrochemical process. This work highlights the engineering of the composition of intermetallic nanoparticles as an effective strategy to design high-performance electrocatalysts.

**Bifunctional Catalysts:** High-performance bifunctional electrocatalysts in the same media can simplify the fabrication procedures of devices, facilitate industrial applications, and lower production costs. Highly active electrocatalysts supported on a hierarchical nanoporous conductive substrate can lead to exceptionally high electrocatalytic performances. Shi et al. constructed nanoporous Cu-supported intermetallic Co<sub>3</sub>Mo as a highly efficient electrocatalyst for the OER and HER with in situ electrooxidation and hydroxylation processes, respectively.<sup>[121]</sup> In particular, the hydroxylated intermetallic Co<sub>3</sub>Mo showed the optimal hydrogen binding energy to promote the adsorption/desorption of hydrogen intermediates (Figure 14a). A two-electrode system was constructed for overall water electrolysis (Figure 14b), and the device requires a small overpotential of

420 mV to realize a current density of  $145 \text{ mA cm}^{-2}$ , along with good operational stability compared to that of the benchmark Pt/C + Ir/C couple (Figure 14c,d).

High-performance and low-cost bifunctional electrocatalysts toward the OER and ORR enable high power density levels in Zn-air batteries. FeNi<sub>3</sub>-based intermetallics have been demonstrated as promising oxygen electrocatalysts due to their high activity, good earth-abundance, and economic sustainability. Plasma technology was utilized to incorporate excess Fe into intermetallic FeNi<sub>3</sub>.<sup>[122]</sup> Through the modulation of the electronic interaction and lattice structure, valence electrons near the Fermi level and the volume of the initial cell were greatly enhanced for the Fe-enriched-FeNi<sub>3</sub>/NC sample compared to a pristine FeNi<sub>3</sub> crystal structure. The improved OER and ORR activities were ascribed to the formation of activated electrons and active sites (Figure 14e). The performance of a practical battery was evaluated by constructing a home-made Zn-air battery setup (Figure 14f). Peak power density of  $89 \text{ mW cm}^{-2}$  was obtained using Fe-enriched FeNi<sub>3</sub>/NC as the cathode material (Figure 14g). The overall performance of Fe-enriched FeNi<sub>3</sub>/NC surpasses that of the Pt/C + Ir/C couple, further demonstrating the bifunctional oxygen catalytic activities through the tuning of lattice distortion defects (Figure 14h).

## 6. Summary and Perspective

Intensive research efforts over the past decade have expanded the applications of structurally ordered materials and deepened our understanding of the electrocatalytic properties of electrocatalysts with an ordered structure. The recent significant advances of structurally ordered materials as highly efficient electrocatalysts have been summarized in this review. The relationship between the unique ordered structure and remarkable electrochemical performance outcomes has been especially emphasized. The atomically ordered arrangement of metal elements leads to strong intrinsically interatomic interaction. Additionally, the well-defined stoichiometries and flexible control of the local geometry further make ordered structure materials exhibit exceptional physicochemical properties. The main findings of the recently reported state-of-the-art electrocatalysts based on ordered structure materials have been summarized in Tables 1 and 2 for comparison. Despite these inspiring achievements, developing high-performance and low-cost electrocatalysts remains a great challenge. Below, we discuss the opportunities and perspectives for future studies.

### 6.1. Exploiting New Materials and New Applications

The exploration of new materials based on a long-range ordered structure with enhanced electrocatalytic performance is in strong demand. A complete paradigm on precisely controlling the physicochemical properties by modulating the arrangement of atoms within the ordered framework should also be presented. Notably, tuning the size, structure and composition at the nanoscale level should be systemically considered, as these achievements are the key factors impacting the overall electrocatalytic activity and stability. In addition to new materials design, structurally ordered

materials are also expected to be applied in other promising electrochemical reactions such as CO<sub>2</sub> reduction reaction and N<sub>2</sub> reduction reaction. To the best of our knowledge, the related works are still limited, which call for the establishment of relationship between material properties and reaction mechanisms.

### 6.2. Ordered Structures beyond Long-Range Ordering

In addition to the long-range ordering, materials with short-range ordering, namely amorphous structure, also show some advantages such as rich dangling bonds and more exposed surface active sites.<sup>[137]</sup> The in situ-formed (oxy)hydroxides during the electrochemical reaction usually exhibit low crystallinity. Recently, to highlight the advantageous role of transition (oxy)hydroxides with low crystallinity in electrocatalysis, Ye et al. synthesized low-crystallinity and high-crystallinity CoOOH nanosheet arrays.<sup>[138]</sup> The former one possesses considerable short-range (1–5 nm) ordered grains with different orientations. In particular, the abundant grain boundaries (edge sites of CoOOH) and oxygen vacancies enable low-crystallinity CoOOH nanosheet arrays to exhibit significantly improved OER activity compared to the perfect structure (high-crystallinity CoOOH nanosheet arrays). This work presented a novel approach to synthesize the defective materials with a short-range ordered feature for electrocatalysis. In addition, Shan et al. reported that Ir single atoms can be accommodated into the cationic sites of cobalt spinel oxide with short-range order and an identical spatial correlation as the host lattice.<sup>[139]</sup> In particular, due to the strong interaction between Ir and cobalt oxide support, the resultant Ir<sub>0.06</sub>Co<sub>2.94</sub>O<sub>4</sub> exhibits remarkable operational stability under OER condition. Thus, the rational design of long-range ordering (with crystalline structure), short-range ordering (with amorphous structure) and crystalline-amorphous materials needs more insights into the material properties and in-depth understanding of the structure-activity relationship.<sup>[137a,140]</sup>

Other than atom arrangement, materials with ordered vacancies and defects are also demonstrated as high-performance electrocatalysts.<sup>[141]</sup> The introduction of defects realizes the effective regulation of intrinsic properties and exploration of special discoveries in nanomaterials.<sup>[142]</sup> In particular, compared to the structure of the traditional trigonal prismatic 2H-phase MoS<sub>2</sub>, 1T-MoS<sub>2</sub> features a well-defined octahedral symmetry. Therefore, 1T-MoS<sub>2</sub> represents an emerging platform for further improving the HER performance of MoS<sub>2</sub> due to their great potential in activating basal planes.<sup>[143]</sup> Additionally, modification of MOFs with ordered active sites is an efficient route for the synthesis of high-performance electrocatalysts. Etching by chemical or physical methods is the general postsynthetic strategy to regulate the electronic structure of MOFs, which is random and uncontrollable at the molecular level. Zhou et al. adopted a top-down strategy that can precisely regulate the local coordination environment of MOF.<sup>[144]</sup> A new ordered MOF containing a hard base ligand and a soft acid metal was successfully designed. Moreover, it is highly expected that more effective design strategies can be presented on MOFs and their derivatives to develop more promising electrocatalysts, especially with the characteristics of ordered active sites.

**Table 1.** Summary of recently reported structurally ordered electrocatalysts based on perovskite oxides.

Catalysts	Applications (Electrolyte)	$\eta_{10a}$ [mV]	Tafel slope [dec $mV^{-1}$ ]	Main findings	Ref.
A-site ordered double perovskite oxides					
PrBa <sub>0.94</sub> Co <sub>2</sub> O <sub>5+<math>\delta</math></sub>	HER (1 M KOH)	186	56.5	Synergistic effect of double/single perovskite heterostructure	[55]
PrBaCo <sub>2</sub> O <sub>5.5</sub>	HER (0.1 M KOH)	245	89.0	Regulating crystal-structures for enhanced activity	[77]
PrBaCo <sub>2</sub> O <sub>6-<math>\delta</math></sub>	HER (1 M KOH)	240	61	Role of the oxygen vacancy content on the HER activity	[78]
PrBaCo <sub>2</sub> O <sub>6-<math>\delta</math></sub>	OER (1 M KOH)	360	70	Role in the oxygen vacancy content on the OER activity	[70]
BaGdCo <sub>1.8</sub> Fe <sub>0.2</sub> O <sub>6</sub>	OER (1 M NaOH)	477	60.1	Highly active Co-based double perovskite	[90]
PrBa <sub>0.85</sub> Ca <sub>0.15</sub> MnFeO <sub>5+<math>\delta</math></sub>	OER (0.1 M KOH)	400	86	Stable double perovskite structure with bifunctional properties	[91]
	ORR (0.1 M KOH)	768 <sup>b)</sup>	N.A.c)		
PBSCF	OER (1 M KOH)	313	58	Understanding/controlling oxygen defects for the OER	[92]
PBSCF	OER (1 M KOH)	434 ( $\eta$ 2.5)	86	Improving the proton-coupled electron transfer process by the crystal orientation	[74]
PBSCF	OER (0.1 M KOH)	359	56	Porous structure with a high surface area	[60]
PBSCF	OER (0.1 M KOH)	358	52	Nanofiber structure with exceptional OER activity	[59]
PrBaCo <sub>2(1-x)</sub> Fe <sub>2x</sub> Co <sub>6-<math>\delta</math></sub>	OER (0.1 M KOH)	≈310	50	Uncovering the origin of the high OER performance for the Fe-doped Co-based A-site double perovskite	[72]
PrBa <sub>0.5</sub> Sr <sub>0.5</sub> Co <sub>2</sub> O <sub>5+<math>\delta</math></sub> @FeOOH	OER (0.1 M KOH)	390	53	Oxyhydroxide/perovskite heterostructure exhibiting outstanding bifunctional properties	[54]
	HER (0.1 M KOH)	280	70		
EuBa <sub>0.5</sub> Sr <sub>0.5</sub> Co <sub>1.6</sub> Fe <sub>0.4</sub> O <sub>5+<math>\delta</math></sub>	OER (1 M KOH)	420	68.3	Highly active Fe sites with an octahedral coordination	[93]
BaNdMn <sub>2</sub> O <sub>5.5</sub>	OER (1 M KOH)	≈410	75	Oxygen-deficient double perovskite utilized for overall water splitting	[67]
	HER (1 M KOH)	290	87		
NdBa <sub>0.75</sub> Ca <sub>0.25</sub> Co <sub>1.5</sub> Fe <sub>0.5</sub> O <sub>5+<math>\delta</math></sub>	OER (0.1 M KOH)	397	81	B-site doping effects of the double perovskite for the OER and ORR	[94]
	ORR (0.1 M KOH)	679 ( $\eta$ -3)	48		
SmBa <sub>0.5</sub> Sr <sub>0.5</sub> Co <sub>2</sub> O <sub>6-<math>\delta</math></sub>	OER (0.1 M KOH)	370	46	Morphology, crystal structure, and electronic state co-tuning	[95]
Sr <sub>2</sub> Fe <sub>2</sub> O <sub>6-<math>\delta</math></sub>	OER (0.1 M KOH)	480	60	Electrical conductivity and defect-order structure for the OER	[96]
Ca <sub>2</sub> FeRuO <sub>6</sub>	ORR (1 M KOH)	780b)	76	The contribution of cooperative effect of 3d and 4d B-site metal ions and the synergistic effects of metal ions and the oxygen to catalytic activity	[97]
	OER (1 M KOH)	400	102		
	HER (1 M KOH)	418	N.A.		
(Gd <sub>0.5</sub> La <sub>0.5</sub> )BaCo <sub>2</sub> O <sub>5.75</sub>	HER (1 M KOH)	185	27.6	Ordered oxygen vacancies and high-valence metal sites for the high-performance HER	[79]

**Table 1.** Continued.

Catalysts	Applications(Electrolyte)	$\eta_{10a}$ [mV]	Tafel slope[dec mV <sup>-1</sup> ]	Main findings	Ref.
B-site ordered double perovskite oxides					
La <sub>2</sub> NiMnO <sub>6</sub>	OER (1 M KOH)	≈390	58	Vibronic superexchange in a double perovskite	[84]
La <sub>1.4</sub> Sr <sub>0.6</sub> NiMnO <sub>6</sub>	OER (1 M KOH)	367 ( $\eta_1$ )	86	Tuning the electronic structure for enhanced bifunctional properties	[98]
	ORR (1 M KOH)	720 <sup>b)</sup>	N.A.		
La <sub>1.5</sub> Sr <sub>0.5</sub> NiMn <sub>0.5</sub> Ru <sub>0.5</sub> O <sub>6</sub>	OER (0.1 M KOH)	430	N.A.	Multiple active sites for the OER and ORR in an ordered structure	[85]
	ORR (0.1 M KOH)	830 ( $\eta_1$ )	N.A.		
SFCMN	OER (0.1 M KOH)	310	56	Utilizing the ordered structure to introduce active elements	[80]
Sr <sub>2</sub> Fe <sub>1.5-x</sub> Co <sub>x</sub> Ni <sub>y</sub> Mo <sub>0.5</sub> O <sub>6-δ</sub>	OER (0.1 M KOH)	389	79	Ternary phase diagram of the rapid screening of high performance double perovskites	[99]
Sr <sub>2</sub> Fe <sub>1.3</sub> Ni <sub>0.2</sub> Mo <sub>0.5</sub> O <sub>6-δ</sub>	OER (0.1 M KOH)	360	59	Double perovskites decorated with oxygen vacancies and Fe-Ni alloy nanoparticles after ex-solution	[34]
Sr <sub>2</sub> Fe <sub>0.8</sub> Co <sub>0.2</sub> Mo <sub>0.6</sub> Co <sub>0.4</sub> O <sub>6-δ</sub>	OER (0.1 M KOH)	345	54	Building an ordered structure and introducing multi-element synergy	[100]
SrCo <sub>0.4</sub> Fe <sub>0.2</sub> W <sub>0.4</sub> O <sub>3-δ</sub>	OER (0.1 M KOH)	357	58	Material genome strategy to develop high-activity catalysts	[101]
Sr <sub>2</sub> CoIrO <sub>6</sub>	OER 0.1 M HClO <sub>4</sub>	≈370	N.A.	Evaluation of dissolution and precipitation equilibrium of Ir-based perovskite oxides	[43]
Sr <sub>2</sub> CoIrO <sub>6-δ</sub>	OER (1 M KOH)	210	N.A.	In situ formed high-valence Ir <sup>6+</sup> facilitating ultrafast OER	[45]
Ba <sub>2</sub> Bi <sub>0.1</sub> Sc <sub>0.2</sub> Co <sub>1.7</sub> O <sub>6-δ</sub>	OER (0.1 M KOH)	≈490	102	Dual active sites in an ordered structure	[24e]
Ba <sub>2</sub> CoMo <sub>0.5</sub> Nb <sub>0.5</sub> O <sub>6-δ</sub>	OER (0.1 M KOH)	435	77	Co-doping method to synthesize an ordered perovskite	[102]
Ba <sub>2</sub> PrIrO <sub>6</sub>	OER (0.1 M HClO <sub>4</sub> )	≈400	60	Developing high-performance double perovskite electrocatalysts	[103]
Quadruple perovskite oxides					
CaMn <sub>7</sub> O <sub>12</sub>	OER (0.1 M KOH)	270 ( $\eta_{0.01}$ )	101	Structure-activity relationship of quadruple manganese perovskite	[104]
CaCu <sub>3</sub> Fe <sub>4</sub> O <sub>12</sub>	OER (0.1 M KOH)	310 ( $\eta_{0.5}$ )	51	Covalent bonding network improving the structural stability	[86c]
CaCu <sub>3</sub> Ru <sub>4</sub> O <sub>12</sub>	OER (0.5 M H <sub>2</sub> SO <sub>4</sub> )	171	40	A lower Ru 4d-band center optimizing the binding energy of oxygen intermediates	[89]
CaCu <sub>3</sub> Ti <sub>4</sub> O <sub>12</sub>	OER (0.1 M KOH)	≈1020	N.A.	Bifunctional properties of quadruple perovskite nanoparticles	[88]
	ORR (0.1 M KOH)	≈630 ( $\eta_1$ )	N.A.		
CaCu <sub>3</sub> Fe <sub>4</sub> O <sub>12</sub>	OER (0.1 M KOH)	≈250 ( $\eta_{0.05}$ )	N.A.	Systematic study of the OER activity of quadruple perovskite and single perovskite oxides	[87]

<sup>a)</sup>  $\eta_{10}$  represents overpotentials corresponding to 10 mA cm<sup>-2</sup>; <sup>b)</sup> Represents the value related to half-wave potential; <sup>c)</sup> N.A. represents data not available in the literature.

### 6.3. Advancing In Situ/Operando Techniques

Under electrochemical conditions, surface changes of structurally ordered electrocatalysts require the rational establishment of a structure-activity relationship. Therefore, more advanced characterization techniques and tools are also required to study the structural characteristics before and after electrochemical reactions. In particular, in situ/operando techniques enable

observations of the dynamic changes of electrocatalysts during electrochemical reactions, which are beneficial when seeking to understand the structure-performance properties. For instance, in situ/operando TEM can detect the morphological and structural reconstruction processes during electrochemical reactions.<sup>[145]</sup> Additionally, in situ/operando XAS can track the structural reconstruction of electrocatalysts under electrochemical conditions.<sup>[40h,40i,146]</sup> Furthermore, it is beneficial to

**Table 2.** Summary of recently reported structurally ordered electrocatalysts based on intermetallic materials.

Catalysts	Applications (Electrolyte)	Potential [mV]	Tafel slope [mV dec <sup>-1</sup> ]	Main findings	Ref.
PtCo <sub>3</sub>	ORR (0.1 M HClO <sub>4</sub> )	903 <sup>b)</sup>	N.A. <sup>c)</sup>	Evaluation of low-Pt intermetallic catalysts	[108]
PtCo	ORR (0.1 M HClO <sub>4</sub> )	≈920 <sup>b)</sup>	N.A.	Strong electrostatic adsorption method for the preparation of sub-three nanometer intermetallics	[65]
PtZn	ORR (0.1 M HClO <sub>4</sub> )	911 <sup>b)</sup>	57	Size-controlled intermetallic nanoparticles on a N-doped carbon support	[64]
Pt <sub>3</sub> In	ORR (0.1 M HClO <sub>4</sub> )	920 <sup>b)</sup>	N.A.	Large-scale synthesis of intermetallic clusters on commercial carbon black	[38]
Pt <sub>3</sub> Co	ORR (0.1 M HClO <sub>4</sub> )	930 <sup>b)</sup>	62	Synthesis of mesoporous carbon confined intermetallic nanoparticles	[63]
Pt <sub>3</sub> Co	ORR (0.1 M HClO <sub>4</sub> )	943 <sup>b)</sup>	N.A.	Synthesis of high-loading intermetallic core-shell nanoparticles	[123]
Pt <sub>3</sub> Mn	ORR (0.1 M HClO <sub>4</sub> )	900 <sup>b)</sup>	N.A.	Scalable synthesis of Pt-based intermetallic ultra-small nanoparticles	[15b]
PtCu Nanoframes	ORR (0.1 M HClO <sub>4</sub> )	940 <sup>b)</sup>	N.A.	Synthesis of intermetallic nano-frames	[107]
PtNiN	ORR (0.1 M HClO <sub>4</sub> )	935 <sup>b)</sup>	N.A.	Formation of an intermetallic phase and further N-doping	[110]
PtCuN	ORR (0.1 M HClO <sub>4</sub> )	916 <sup>b)</sup>	N.A.	Preparation of rhombohedral L1 <sub>1</sub> ordered PtCu and further N-doping	[105a]
PtFe@Pt	ORR (0.1 M HClO <sub>4</sub> )	921 <sup>b)</sup>	58	Intermetallic with an atomic Pt shell	[124]
Mo-PtFe	ORR (0.1 M HClO <sub>4</sub> )	920 <sup>b)</sup>	N.A.	Electronic regulation of a Pt-based intermetallic by Mo-doping	[125]
Au-PtFe	ORR (0.1 M HClO <sub>4</sub> )	895 <sup>b)</sup>	N.A.	Au doping for activity improvement and chemical stabilization of an intermetallic	[126]
PtM@Fe-N-C	ORR (0.1 M HClO <sub>4</sub> )	923 <sup>b)</sup>	64	Atomically dispersed Fe-N-C decorated with a Pt alloy	[57]
PdFe	ORR (0.1 M HClO <sub>4</sub> )	850 <sup>b)</sup>	57	Surface engineering of an intermetallic with enhanced ORR performance	[15a]
Pt <sub>3</sub> Co	HER (0.5 M H <sub>2</sub> SO <sub>4</sub> )	13 <sup>a)</sup>	27.4	Designing ultrafine intermetallic nanoparticles supported on N-doped graphene	[119]
PtCu	HER (0.5 M H <sub>2</sub> SO <sub>4</sub> )	19.7 <sup>a)</sup>	27	PdCu nanostructure with an intermetallic B2 phase with superior HER performance	[118]
RuB <sub>2</sub>	HER (0.5 M H <sub>2</sub> SO <sub>4</sub> )	15.6 <sup>a)</sup>	30.2	Phase-pure ruthenium-boron intermetallic for the HER	[127]
	HER (1 M KOH)	25.0 <sup>a)</sup>	27.9		
Pd <sub>31</sub> Bi <sub>12</sub>	ORR (0.1 M KOH)	960 <sup>d)</sup>	21	Direct and rapid synthesis of a metastable intermetallic at room-temperature	[128]
Pd <sub>3</sub> Mn	ORR (0.1 M KOH)	832 <sup>b)</sup>	N.A.	Electrospinning synthesis of carbon-supported intermetallic nanocrystals	[129]
Pd <sub>2</sub> Sn nanosheets	ORR (0.1 M KOH)	893 <sup>b)</sup>	N.A.	2D defect-rich nanocrystal intermetallic	[130]
Pd <sub>3</sub> Pb nanocubes	ORR (0.1 M KOH)	880 <sup>b)</sup>	31	A low-temperature approach to synthesize intermetallic nanocubes	[114]
Pd <sub>3</sub> Pb	ORR (0.1 M KOH)	908 <sup>b)</sup>	55.6	Template-directed strategy for the rapid synthesis of a porous intermetallic with tunable sizes	[115]
PtFe	ORR (0.1 M KOH)	864 <sup>b)</sup>	42	Intermetallic with an ultralow Pt loading	[131]

**Table 2.** Continued.

Catalysts	Applications (Electrolyte)	Potential [mV]	Tafel slope [mV dec <sup>-1</sup> ]	Main findings	Ref.
PdZn/Co	ORR (0.1 M KOH)	766 <sup>b)</sup>	57.6	Atomically ordered intermetallic coupled with Co nanoparticles	[132]
Fe <sub>6</sub> Ge <sub>5</sub>	OER (1 M KOH)	272 ( $\eta$ 100)	32	In situ formation of a core-shell structure for an intermetallic under OER conditions	[48]
NiZn	OER (1 M KOH)	283 <sup>a)</sup>	73	Ultra-small intermetallic nanoparticles for efficient electrocatalysis	[120]
NiGe	OER (1 M KOH)	228 <sup>a)</sup>	56	In situ formation of $\gamma$ -NiOOH from intermetallic NiGe during OER	[51]
Ni <sub>2/3</sub> Fe <sub>1/3</sub> Al	OER (1 M KOH)	299 <sup>a)</sup>	58.9	Al leaching of intermetallic NiFe aluminides	[49b]
Ni <sub>2</sub> Si	OER (0.1 M KOH)	$\approx$ 570 <sup>a)</sup>	94	Liquid-phase synthesis in molten salts of intermetallic nanocrystals	[49a]
FeCoNiCrNb <sub>0.5</sub>	OER (0.1 M KOH)	288 <sup>a)</sup>	27.7	An intermetallic-oxide core-shell structure derived from a top-down dealloying approach	[133]
Ir <sub>3</sub> V	HER (1 M KOH)	9 <sup>a)</sup>	21.4	Intermetallic for the HER in alkaline media	[16b]
Gd <sub>2</sub> Ni <sub>17</sub>	HER (1 M KOH)	43.5 <sup>a)</sup>	32	Regulation of lanthanide contraction to tune the HER activity of an iron triad intermetallic	[117]
TiCo <sub>2</sub>	HER (1 M KOH)	70 <sup>a)</sup>	33	Manipulation of crystal and electronic structure to achieve high activity	[134]
Cu/Cu <sub>2</sub> Zr	HER (1 M KOH)	155 ( $\eta$ 100)	68	Intermetallic clusters in situ anchored on hierarchical nanoporous copper	[135]
Cu/Co <sub>3</sub> Mo	OER (1 M KOH)	$\approx$ 330 ( $\eta$ 100)	82	Intermetallic spontaneously separated from a hierarchical nanoporous copper skeleton	[121]
	HER (1 M KOH)	12 <sup>a)</sup>	40		
CoSn <sub>2</sub>	OER (1 M KOH)	230 <sup>a)</sup>	89	Intermetallic nanocrystals for high-performance electrocatalytic overall water splitting	[50]
	HER (1 M KOH)	103 <sup>a)</sup>	78		
FeNi <sub>3</sub>	OER (1 M KOH)	277 <sup>a)</sup>	77	Nitrogen-doped carbon-coupled FeNi <sub>3</sub> intermetallic for Zn-air batteries	[136]
	ORR (0.1 M KOH)	860 <sup>b)</sup>	N.A.		
Fe-enriched FeNi <sub>3</sub>	OER (0.1 M KOH)	360 <sup>a)</sup>	82	Fe-enriched FeNi <sub>3</sub> intermetallic for a Zn-air battery	[122]
	ORR (0.1 M KOH)	790 <sup>b)</sup>	77		

<sup>a)</sup>Represents overpotentials corresponding to 10 mA cm<sup>-2</sup>; <sup>b)</sup>Represents the value related to half-wave potential; <sup>c)</sup>N.A. represents data not available in the literature; <sup>d)</sup>The value represents the onset potential for the ORR.

construct a structural model for structurally ordered materials with uniform active sites on the same surface plane and with a precise structure, providing more opportunities for DFT calculations. Combinations of advanced in situ/operando techniques and DFT calculations can greatly promote the design of more promising electrocatalysts.

#### 6.4. Meeting the Requirements of Practical Applications

Although numerous electrocatalysts have been successfully designed and evaluated, their catalytic performances still do not meet the requirements of practical applications.<sup>[2a,147]</sup> First,

designs of high-performance electrocatalysts are required. For example, the requirements of OER electrocatalysts for industrial alkaline water electrolysis include a high current density (>500 mA cm<sup>-2</sup>) at a low overpotential with long-term operational stability.<sup>[148]</sup> Therefore, in addition to evaluations of the intrinsic activity (e.g., overpotential corresponding to a current density of 10 mA cm<sup>-2</sup>), effective and feasible scale-up strategies are also crucial to design electrocatalysts with a view toward large-scale production.<sup>[149]</sup> Second, it is important both to design high-performance bifunctional electrocatalysts capable of simplifying the device and operation procedures and to accelerate the industrialization of those promising energy conversion devices.<sup>[11b,148,149]</sup>

Over all, we hope this review can provide a guideline for future explorations of novel structurally ordered-based materials and new applications of these promising materials.

## Acknowledgements

This research was supported by the Hydrogen Energy Innovation Technology Development Program (NRF-2019M3E6A1064523), Nano-Material Technology Development Program (2017M3A7B4049547), and National R&D Program (2020M3H4A3105824) through the National Research Foundation of Korea (NRF) funded by the Ministry of Science, ICT and Future Planning. This research was performed as a cooperation project of “Basic project (referring to projects performed with the budget directly contributed by the Government to achieve the purposes of establishment of Government-funded research Institutes)” and supported by the KOREA RESEARCH INSTITUTE of CHEMICAL TECHNOLOGY (KRICT) (KS2122-10). China Postdoctoral Science Foundation funded project (No. 2020T130676).

## Conflict of Interest

The authors declare no conflict of interest.

## Keywords

electrocatalysts, intermetallic, ordered structures, perovskites, structure-activity relationship

Received: June 24, 2021

Revised: July 30, 2021

Published online:

- [1] a) S. Chu, A. Majumdar, *Nature* **2012**, *488*, 294; b) Z. W. Seh, J. Kibsgaard, C. F. Dickens, I. Chorkendorff, J. K. Nørskov, T. F. Jaramillo, *Science* **2017**, *355*, eaad4998.
- [2] a) M. F. Lagadec, A. Grimaud, *Nat. Mater.* **2020**, *19*, 1140; b) F. Xiao, Y.-C. Wang, Z.-P. Wu, G. Chen, F. Yang, S. Zhu, K. Siddharth, Z. Kong, A. Lu, J.-C. Li, C.-J. Zhong, Z.-Y. Zhou, M. Shao, *Adv. Mater.* **2021**, 2006292; c) Q. Liu, Z. Pan, E. Wang, L. An, G. Sun, *Energy Storage Mater.* **2020**, *27*, 478; d) J. Yu, B.-Q. Li, C.-X. Zhao, Q. Zhang, *Energy Environ. Sci.* **2020**, *13*, 3253; e) J. Wang, Y. Gao, H. Kong, J. Kim, S. Choi, F. Ciucci, Y. Hao, S. Yang, Z. Shao, J. Lim, *Chem. Soc. Rev.* **2020**, *49*, 9154; f) J. Yu, R. Ran, Y. Zhong, W. Zhou, M. Ni, Z. Shao, *Energy Environ. Mater.* **2020**, *3*, 121; g) X. Xu, Y. Pan, Y. Zhong, R. Ran, Z. Shao, *Mater. Horiz.* **2020**, *7*, 2519.
- [3] a) S. Zaman, L. Huang, A. I. Douka, H. Yang, B. You, B. Y. Xia, *Angew. Chem., Int. Ed.* **2021**, *60*, 17832; b) S. Im, J.-H. Lee, H.-I. Ji, *J. Korean Ceram. Soc.* **2021**, *58*, 351; c) Y. Zhang, B. Chen, D. Guan, M. Xu, R. Ran, M. Ni, W. Zhou, R. O'Hayre, Z. Shao, *Nature* **2021**, *591*, 246.
- [4] a) J. Zhang, L. Shen, Y. Jiang, S. Sun, *Nanoscale* **2020**, *12*, 19557; b) M. Li, X. Bi, R. Wang, Y. Li, G. Jiang, L. Li, C. Zhong, Z. Chen, J. Lu, *Matter* **2020**, *2*, 32.
- [5] a) W.-J. Jiang, T. Tang, Y. Zhang, J.-S. Hu, *Acc. Chem. Res.* **2020**, *53*, 1111; b) H. Sun, X. Xu, Y. Song, W. Zhou, Z. Shao, *Adv. Funct. Mater.* **2021**, *31*, 2009779; c) M. Wang, L. Zhang, Y. He, H. Zhu, *J. Mater. Chem. A* **2021**, *9*, 5320; d) X. Liu, M. Gong, S. Deng, T. Zhao, T. Shen, J. Zhang, D. Wang, *Adv. Funct. Mater.* **2021**, *31*, 2009032; e) V. R. Jothi, K. Karuppasamy, T. Maiyalagan, H. Rajan, C.-Y. Jung, S. C. Yi, *Adv. Energy Mater.* **2020**, *10*, 1904020; f) J. N. Hausmann, R. Schlögl, P. W. Menezes, M. Driess, *Energy Environ. Sci.* **2021**, *14*, 3679.
- [6] a) S. Gupta, M. K. Patel, A. Miotello, N. Patel, *Adv. Funct. Mater.* **2020**, *30*, 1906481; b) J. Song, C. Wei, Z.-F. Huang, C. Liu, L. Zeng, X. Wang, Z. J. Xu, *Chem. Soc. Rev.* **2020**, *49*, 2196; c) J. Yu, Q. He, G. Yang, W. Zhou, Z. Shao, M. Ni, *ACS Catal.* **2019**, *9*, 9973; d) Y. Pan, X. Xu, Y. Zhong, L. Ge, Y. Chen, J.-P. M. Veder, D. Guan, R. O'Hayre, M. Li, G. Wang, H. Wang, W. Zhou, Z. Shao, *Nat. Commun.* **2020**, *11*, 2002; e) X. Xu, C. Su, W. Zhou, Y. Zhu, Y. Chen, Z. Shao, *Adv. Sci.* **2016**, *3*, 1500187.
- [7] a) Y.-L. Zhang, K. Goh, L. Zhao, X.-L. Sui, X.-F. Gong, J.-J. Cai, Q.-Y. Zhou, H.-D. Zhang, L. Li, F.-R. Kong, D.-M. Gu, Z.-B. Wang, *Nanoscale* **2020**, *12*, 21534; b) Y. Dai, J. Yu, C. Cheng, P. Tan, M. Ni, *Chem. Eng. J.* **2020**, *397*, 125516.
- [8] a) S. Song, J. Sun, J. Zhou, Z. Hu, H.-J. Lin, T.-S. Chan, C.-T. Chen, N. Zhang, C. Jing, J. Hu, L. Zhang, J.-Q. Wang, *Chem. Eng. J.* **2021**, *425*, 130681; b) L. An, C. Wei, M. Lu, H. Liu, Y. Chen, G. G. Scherer, A. C. Fisher, P. Xi, Z. J. Xu, C.-H. Yan, *Adv. Mater.* **2021**, *33*, 2006328; c) Z.-F. Huang, J. Song, S. Dou, X. Li, J. Wang, X. Wang, *Matter* **2019**, *1*, 1494.
- [9] a) Y. Li, Y. Sun, Y. Qin, W. Zhang, L. Wang, M. Luo, H. Yang, S. Guo, *Adv. Energy Mater.* **2020**, *10*, 1903120; b) Z. Chen, X. Duan, W. Wei, S. Wang, B.-J. Ni, *Nano Energy* **2020**, *78*, 105270; c) T. Wang, A. Chutia, D. Brett, P. Shearing, G. He, G. Chai, I. P. Parkin, *Energy Environ. Sci.* **2021**, *14*, 2639; d) J. Zhang, L. Zhang, Z. Cui, *Chem. Commun.* **2021**, *57*, 11; e) H. Sun, W. Jung, *J. Mater. Chem. A* **2021**, *9*, 15506.
- [10] a) D. Zhou, P. Li, W. Xu, S. Jawaid, J. Mohammed-Ibrahim, W. Liu, Y. Kuang, X. Sun, *ChemNanoMat* **2020**, *6*, 336; b) S. Zhang, S. E. Saji, Z. Yin, H. Zhang, Y. Du, C.-H. Yan, *Adv. Mater.* **2021**, *33*, 2005988; c) K. Li, W. Chen, *Mater. Today Energy* **2021**, *20*, 100638; d) W. Wang, M. Xu, X. Xu, W. Zhou, Z. Shao, *Angew. Chem., Int. Ed.* **2020**, *59*, 136; e) H. Sun, J. Dai, W. Zhou, Z. Shao, *Energy Fuels* **2020**, *34*, 10547; f) S. Zhang, T. Yu, H. Wen, Z. Ni, Y. He, R. Guo, J. You, X. Liu, *Chem. Commun.* **2020**, *56*, 15387; g) N. Ma, G. Chen, Y. Zhu, H. Sun, J. Dai, H. Chu, R. Ran, W. Zhou, R. Cai, Z. Shao, *Small* **2020**, *16*, 2002089; h) Y. Zhu, H. A. Tahini, Z. Hu, J. Dai, Y. Chen, H. Sun, W. Zhou, M. Liu, S. C. Smith, H. Wang, Z. Shao, *Nat. Commun.* **2019**, *10*, 149; i) Z. Yang, F. Shaik, K. Liang, K. Guo, X. Ren, B. Jiang, *Electron. Mater. Lett.* **2021**, *17*, 87; j) A. Song, L. Cao, W. Yang, W. Yang, L. Wang, Z. Ma, G. Shao, *Carbon* **2019**, *142*, 40.
- [11] a) J. Zhao, J.-J. Zhang, Z.-Y. Li, X.-H. Bu, *Small* **2020**, *16*, 2003916; b) K. Zeng, X. Zheng, C. Li, J. Yan, J.-H. Tian, C. Jin, P. Strasser, R. Yang, *Adv. Funct. Mater.* **2020**, *30*, 2000503; c) H. Yi, R. Qin, S. Ding, Y. Wang, S. Li, Q. Zhao, F. Pan, *Adv. Funct. Mater.* **2020**, *31*, 2006970; d) Y. Wang, H. Su, Y. He, L. Li, S. Zhu, H. Shen, P. Xie, X. Fu, G. Zhou, C. Feng, D. Zhao, F. Xiao, X. Zhu, Y. Zeng, M. Shao, S. Chen, G. Wu, J. Zeng, C. Wang, *Chem. Rev.* **2020**, *120*, 12217; e) C. Sun, J. A. Alonso, J. Bian, *Adv. Energy Mater.* **2020**, *11*, 2000459; f) H. Y. Kim, S. H. Joo, *J. Mater. Chem. A* **2020**, *8*, 8195; g) C. Feng, M. B. Faheem, J. Fu, Y. Xiao, C. Li, Y. Li, *ACS Catal.* **2020**, *10*, 4019; h) X. Wang, Y. Zheng, W. Sheng, Z. J. Xu, M. Jaroniec, S.-Z. Qiao, *Mater. Today* **2020**, *36*, 125; i) C. Xu, A. Vasileff, Y. Zheng, S.-Z. Qiao, *Adv. Mater. Interfaces* **2021**, *8*, 2001904.
- [12] a) W. Xiao, W. Lei, M. Gong, H. L. Xin, D. Wang, *ACS Catal.* **2018**, *8*, 3237; b) S. L. A. Bueno, H. M. Ashberry, I. Shafei, S. E. Skrabalak, *Acc. Chem. Res.* **2021**, *54*, 1662; c) L. Rößner, M. Armbrüster, *ACS Catal.* **2019**, *9*, 2018; d) X. Xu, Y. Zhong, Z. Shao, *Trends Chem.* **2019**, *1*, 410; e) Y. Liu, C. Xiao, P. Huang, M. Cheng, Y. Xie, *Chem* **2018**, *4*, 1263; f) Y. Zhang, X. Xu, *CrystEngComm* **2020**, *22*, 6385.
- [13] a) H. Liu, L. Liu, L. Wei, B. Chu, Z. Qin, G. Jin, Z. Tong, L. Dong, B. Li, *Fuel* **2020**, *272*, 117738; b) H. Arandiyani, Y. Wang, H. Sun, M. Rezaei, H. Dai, *Chem. Commun.* **2018**, *54*, 6484; c) X. Li,

- D.-D. Ma, C. Cao, R. Zou, Q. Xu, X.-T. Wu, Q.-L. Zhu, *Small* **2019**, *15*, 1902218.
- [14] a) H. Yi, S. Liu, C. Lai, G. Zeng, M. Li, X. Liu, B. Li, X. Huo, L. Qin, L. Li, M. Zhang, Y. Fu, Z. An, L. Chen, *Adv. Energy Mater.* **2021**, *11*, 2002863; b) Y. Wang, J. Liu, G. Zheng, *Adv. Mater.* **2021**, *33*, 2005798; c) D. Liu, P. Zhou, H. Bai, H. Ai, X. Du, M. Chen, D. Liu, W. F. Ip, K. H. Lo, C. T. Kwok, S. Chen, S. Wang, G. Xing, X. Wang, H. Pan, *Small* **2021**, 2101605.
- [15] a) M. Gong, T. Shen, Z. Deng, H. Yang, Z. Li, J. Zhang, R. Zhang, Y. Hu, X. Zhao, H. Xin, D. Wang, *Chem. Eng. J.* **2021**, *408*, 127297; b) B. Zhang, G. Fu, Y. Li, L. Liang, N. S. Grundish, Y. Tang, J. B. Goodenough, Z. Cui, *Angew. Chem., Int. Ed.* **2020**, *132*, 7931.
- [16] a) H.-S. Chen, T. M. Benedetti, J. Lian, S. Cheong, P. B. O'Mara, K. O. Sulaiman, C. H. W. Kelly, R. W. J. Scott, J. J. Gooding, R. D. Tilley, *ACS Catal.* **2021**, *11*, 2235; b) L.-W. Chen, X. Guo, R.-Y. Shao, Q.-Q. Yan, L.-L. Zhang, Q.-X. Li, H.-W. Liang, *Nano Energy* **2021**, *81*, 105636.
- [17] a) B. Zhang, X. Zheng, O. Voznyy, R. Comin, M. Bajdich, M. García-Melchor, L. Han, J. Xu, M. Liu, L. Zheng, F. P. G. de Arquer, C. T. Dinh, F. Fan, M. Yuan, E. Yassitepe, N. Chen, T. Regier, P. Liu, Y. Li, P. De Luna, A. Janmohamed, H. L. Xin, H. Yang, A. Vojvodic, E. H. Sargent, *Science* **2016**, *352*, 333; b) S. Lin, H. Xu, Y. Wang, X. C. Zeng, Z. Chen, *J. Mater. Chem. A* **2020**, *8*, 5663; c) M. Rück, B. Garlyyev, F. Mayr, A. S. Bandarenka, A. Gagliardi, *J. Phys. Chem. Lett.* **2020**, *11*, 1773; d) J. Liu, H. Liu, H. Chen, X. Du, B. Zhang, Z. Hong, S. Sun, W. Wang, *Adv. Sci.* **2020**, *7*, 1901614.
- [18] a) H. J. Song, H. Yoon, B. Ju, D.-W. Kim, *Adv. Energy Mater.* **2020**, *11*, 2002428; b) J. Wang, S. Choi, J. Kim, S. W. Cha, J. Lim, *Catalysts* **2020**, *10*, 770; c) X. Xu, W. Wang, W. Zhou, Z. Shao, *Small Methods* **2018**, *2*, 1800071.
- [19] C. Zhang, P. Zhao, S. Liu, K. Yu, *Chin. J. Catal.* **2019**, *40*, 1324.
- [20] a) D. Udomsilp, C. Lenser, O. Guillon, N. H. Menzler, *Energy Technol.* **2021**, *9*, 2001062; b) N. Hou, T. Yao, P. Li, X. Yao, T. Gan, L. Fan, J. Wang, X. Zhi, Y. Zhao, Y. Li, *ACS Appl. Mater. Interfaces* **2019**, *11*, 6995; c) M. Ma, J. Qiao, X. Yang, C. Xu, R. Ren, W. Sun, K. Sun, Z. Wang, *ACS Appl. Mater. Interfaces* **2020**, *12*, 12938; d) Y. Ding, Y. Chen, K. C. Pradel, W. Zhang, M. Liu, Z. L. Wang, *Ultramicroscopy* **2018**, *193*, 64; e) S. Choi, S. Yoo, J. Kim, S. Park, A. Jun, S. Sengodan, J. Kim, J. Shin, H. Y. Jeong, Y. Choi, G. Kim, M. Liu, *Sci. Rep.* **2013**, *3*, 2426.
- [21] G. Yang, C. Su, H. Shi, Y. Zhu, Y. Song, W. Zhou, Z. Shao, *Energy Fuels* **2020**, *34*, 15169.
- [22] S. Sengodan, S. Choi, A. Jun, T. H. Shin, Y.-W. Ju, H. Y. Jeong, J. Shin, J. T. S. Irvine, G. Kim, *Nat. Mater.* **2015**, *14*, 205.
- [23] a) K. I. Kobayashi, T. Kimura, H. Sawada, K. Terakura, Y. Tokura, *Nature* **1998**, *395*, 677; b) S. Agrestini, K. Chen, C. Y. Kuo, L. Zhao, H. J. Lin, C. T. Chen, A. Rogalev, P. Ohresser, T. S. Chan, S. C. Weng, G. Auffermann, A. Völzke, A. C. Komarek, K. Yamaura, M. W. Haverkort, Z. Hu, L. H. Tjeng, *Phys. Rev. B* **2019**, *100*, 014443; c) G. S. Thakur, H. L. Feng, W. Schnelle, C. Felser, M. Jansen, *J. Solid State Chem.* **2021**, *293*, 121784.
- [24] a) Z. Deng, M. Retuerto, S. Liu, M. Croft, P. W. Stephens, S. Calder, W. Li, B. Chen, C. Jin, Z. Hu, M.-R. Li, H.-J. Lin, T.-S. Chan, C.-T. Chen, S. W. Kim, M. Greenblatt, *Chem. Mater.* **2018**, *30*, 7047; b) A. K. Tomar, A. Joshi, S. Atri, G. Singh, R. K. Sharma, *ACS Appl. Mater. Interfaces* **2020**, *12*, 15128; c) M. Shaikh, A. Fathima, M. J. Swamynadhan, H. Das, S. Ghosh, *Chem. Mater.* **2021**, *33*, 1594; d) R. P. N. Shankar, F. Orlandi, P. Manuel, W. Zhang, P. S. Halasyamani, A. Sundaresan, *Chem. Mater.* **2020**, *32*, 5641; e) H. Sun, G. Chen, Y. Zhu, B. Liu, W. Zhou, Z. Shao, *Chem. - Eur. J.* **2017**, *23*, 5722; f) M. Goto, X. M. de Irujo-Labalde, T. Saito, S. García-Martín, Y. Shimakawa, *Inorg. Chem.* **2020**, *59*, 2024.
- [25] A. Neroni, E. Şaşıoğlu, H. Hadipour, C. Friedrich, S. Blügel, I. Mertig, M. Ležaić, *Phys. Rev. B* **2019**, *100*, 115113.
- [26] J. Zhao, J. Gao, W. Li, Y. Qian, X. Shen, X. Wang, X. Shen, Z. Hu, C. Dong, Q. Huang, L. Cao, Z. Li, J. Zhang, C. Ren, L. Duan, Q. Liu, R. Yu, Y. Ren, S.-C. Weng, H.-J. Lin, C.-T. Chen, L.-H. Tjeng, Y. Long, Z. Deng, J. Zhu, X. Wang, H. Weng, R. Yu, M. Greenblatt, C. Jin, *Nat. Commun.* **2021**, *12*, 747.
- [27] a) Z. Liu, Q. Sun, X. Ye, X. Wang, L. Zhou, X. Shen, K. Chen, L. Nataf, F. Baudelet, S. Agrestini, C.-T. Chen, H.-J. Lin, H. B. Vasili, M. Valvidares, Z. Hu, Y.-f. Yang, Y. Long, *Appl. Phys. Lett.* **2020**, *117*, 152402; b) A. Takamatsu, I. Yamada, S. Yagi, H. Ikeno, *J. Phys. Chem. C* **2017**, *121*, 28403; c) Z. Liu, X. Wang, X. Ye, X. Shen, Y. Bian, W. Ding, S. Agrestini, S.-C. Liao, H.-J. Lin, C.-T. Chen, S.-C. Weng, K. Chen, P. Ohresser, L. Nataf, F. Baudelet, Z. Sheng, S. Francoual, J. R. L. Mardegan, O. Leupold, Z. Li, X. Xi, W. Wang, L. H. Tjeng, Z. Hu, Y. Long, *Phys. Rev. B* **2021**, *103*, 014414.
- [28] a) T. Uchimura, I. Yamada, *Chem. Commun.* **2020**, 56, 5500; b) K. Pal, A. Dey, R. Jana, P. P. Ray, P. Bera, L. K. Kumar, T. K. Mandal, P. Mohanty, M. M. Seikh, A. Gayen, *Phys. Chem. Chem. Phys.* **2020**, *22*, 3499; c) K. Pal, A. Mukherjee, M. M. Seikh, P. Bera, A. Gayen, *Ceram. Int.* **2021**, *47*, 14798.
- [29] J. T. L. Gamler, H. M. Ashberry, S. E. Skrabalak, K. M. Koczkur, *Adv. Mater.* **2018**, *30*, 1801563.
- [30] G. Saravanan, K. Nanba, G. Kobayashi, F. Matsumoto, *Electrochim. Acta* **2013**, *99*, 15.
- [31] a) Q. Lenne, Y. R. Leroux, C. Lagrost, *ChemElectroChem* **2020**, *7*, 2345; b) X. Jin, M. Park, S.-J. Shin, Y. Jo, M. G. Kim, H. Kim, Y.-M. Kang, S.-J. Hwang, *Small* **2020**, *16*, 1903265.
- [32] J. Shan, Y. Zheng, B. Shi, K. Davey, S.-Z. Qiao, *ACS Energy Lett.* **2019**, *4*, 2719.
- [33] a) F. Fang, N. Feng, P. Zhao, C. Chen, X. Li, J. Meng, G. Liu, L. Chen, H. Wan, G. Guan, *Chem. Eng. J.* **2019**, *372*, 752; b) J. H. Kim, J. K. Kim, J. Liu, A. Curcio, J.-S. Jang, I.-D. Kim, F. Ciucci, W. Jung, *ACS Nano* **2021**, *15*, 81; c) J. Zhang, M.-R. Gao, J.-L. Luo, *Chem. Mater.* **2020**, *32*, 5424.
- [34] K. Zhu, T. Wu, M. Li, R. Lu, X. Zhu, W. Yang, *J. Mater. Chem. A* **2017**, *5*, 19836.
- [35] a) M. Kim, J. Park, H. Ju, J. Y. Kim, H.-S. Cho, C.-H. Kim, B.-H. Kim, S. W. Lee, *Energy Environ. Sci.* **2021**, *14*, 3053; b) S. Song, J. Zhou, X. Su, Y. Wang, J. Li, L. Zhang, G. Xiao, C. Guan, R. Liu, S. Chen, H.-J. Lin, S. Zhang, J.-Q. Wang, *Energy Environ. Sci.* **2018**, *11*, 2945.
- [36] a) T. Zhou, N. Zhang, C. Wu, Y. Xie, *Energy Environ. Sci.* **2020**, *13*, 1132; b) J. Shan, C. Guo, Y. Zhu, S. Chen, L. Song, M. Jaroniec, Y. Zheng, S.-Z. Qiao, *Chem* **2019**, *5*, 445.
- [37] B. He, K. Tan, Y. Gong, R. Wang, H. Wang, L. Zhao, *Nanoscale* **2020**, *12*, 9048.
- [38] Q. Wang, Z. L. Zhao, Z. Zhang, T. Feng, R. Zhong, H. Xu, S. T. Pantelides, M. Gu, *Adv. Sci.* **2020**, *7*, 1901279.
- [39] M. Tang, W. Chen, S. Luo, X. Wu, X. Fan, Y. Liao, X. Song, Y. Cheng, L. Li, L. Tan, Y. Liu, Z. Quan, *J. Mater. Chem. A* **2021**, *9*, 9602.
- [40] a) H. Jiang, Q. He, Y. Zhang, L. Song, *Acc. Chem. Res.* **2018**, *51*, 2968; b) Y. Duan, S. Sun, Y. Sun, S. Xi, X. Chi, Q. Zhang, X. Ren, J. Wang, S. J. H. Ong, Y. Du, L. Gu, A. Grimaud, Z. J. Xu, *Adv. Mater.* **2019**, *31*, 1807898; c) Y. Li, X. Du, J. Huang, C. Wu, Y. Sun, G. Zou, C. Yang, J. Xiong, *Small* **2019**, *15*, 1901980; d) F. Polo-Garzon, Z. Bao, X. Zhang, W. Huang, Z. Wu, *ACS Catal.* **2019**, *9*, 5692; e) T. Wu, S. Sun, J. Song, S. Xi, Y. Du, B. Chen, W. A. Sasangka, H. Liao, C. L. Gan, G. G. Scherer, L. Zeng, H. Wang, H. Li, A. Grimaud, Z. J. Xu, *Nat. Catal.* **2019**, *2*, 763; f) B. Zhang, K. Jiang, H. Wang, S. Hu, *Nano Lett.* **2019**, *19*, 530; g) X. Liu, R. Guo, K. Ni, F. Xia, C. Niu, B. Wen, J. Meng, P. Wu, J. Wu, X. Wu, L. Mai, *Adv. Mater.* **2020**, *32*, 2001136; h) Y. Zhu, T.-R. Kuo, Y.-H. Li, M.-Y. Qi, G. Chen, J. Wang, Y.-J. Xu, H. M. Chen, *Energy Environ. Sci.* **2021**, *14*, 1928; i) H. Sun, W. Zhou, *Energy Fuels* **2021**, *35*, 5716.
- [41] a) Z. Lei, T. Wang, B. Zhao, W. Cai, Y. Liu, S. Jiao, Q. Li, R. Cao, M. Liu, *Adv. Energy Mater.* **2020**, *10*, 2000478; b) X.-K. Gu, J. C. A. Camayang, S. Samira, E. Nikolla, *J. Catal.* **2020**, *388*, 130.

- [42] a) H. Li, Y. Chen, J. Ge, X. Liu, A. C. Fisher, M. P. Sherburne, J. W. Ager, Z. J. Xu, *JACS Au* **2021**, *1*, 108; b) Y. Sun, R. Li, X. Chen, J. Wu, Y. Xie, X. Wang, K. Ma, L. Wang, Z. Zhang, Q. Liao, Z. Kang, Y. Zhang, *Adv. Energy Mater.* **2021**, *11*, 2003755.
- [43] R. Zhang, N. Dubouis, M. B. Osman, W. Yin, M. T. Sougrati, D. A. D. Corte, D. Giaume, A. Grimaud, *Angew. Chem., Int. Ed.* **2019**, *58*, 4571.
- [44] A. Grimaud, A. Demortière, M. Saubanère, W. Dachraoui, M. Duchamp, M.-L. Doublet, J.-M. Tarascon, *Nat. Energy* **2016**, *2*, 16189.
- [45] L. Li, H. Sun, Z. Hu, J. Zhou, Y.-C. Huang, H. Huang, S. Song, C.-W. Pao, Y.-C. Chang, A. C. Komarek, H.-J. Lin, C.-T. Chen, C.-L. Dong, J.-Q. Wang, L. Zhang, *Adv. Funct. Mater.* **2021**, 2104746. <https://doi.org/10.1002/adfm.202104746>.
- [46] C. Walter, P. W. Menezes, M. Driess, *Chem. Sci.* **2021**, *12*, 8603.
- [47] W. Zou, C. Sun, K. Zhao, J. Li, X. Pan, D. Ye, Y. Xie, W. Xu, H. Zhao, L. Zhang, J. Zhang, *Electrochim. Acta* **2020**, *345*, 136114.
- [48] J. N. Hausmann, R. A. Khalaniya, C. Das, I. Remy-Speckmann, S. Berendts, A. V. Shevelkov, M. Driess, P. W. Menezes, *Chem. Commun.* **2021**, *57*, 2184.
- [49] a) R. Kumar, M. Bahri, Y. Song, F. Gonell, C. Thomas, O. Ersen, C. Sanchez, C. Laberty-Robert, D. Portehault, *Nanoscale* **2020**, *12*, 15209; b) Z. Bai, P. Wang, X. Chen, P. Chen, C. Liang, *Int. J. Hydrogen Energy* **2021**, *46*, 5323.
- [50] P. W. Menezes, C. Panda, S. Garai, C. Walter, A. Guet, M. Driess, *Angew. Chem., Int. Ed.* **2018**, *57*, 15237.
- [51] P. W. Menezes, S. Yao, R. Beltrán-Suito, J. N. Hausmann, P. V. Menezes, M. Driess, *Angew. Chem., Int. Ed.* **2021**, *60*, 4640.
- [52] a) H. Xu, H. Shang, C. Wang, Y. Du, *Coord. Chem. Rev.* **2020**, *418*, 213374; b) H. Sun, B. Hu, D. Guan, Z. Hu, L. Fei, M. Li, V. K. Peterson, H.-J. Lin, C.-T. Chen, R. Ran, W. Zhou, Z. Shao, *ChemSusChem* **2020**, *13*, 3045; c) H. Sun, J. He, Z. Hu, C.-T. Chen, W. Zhou, Z. Shao, *Electrochim. Acta* **2019**, *299*, 926; d) X. Xu, Y. Pan, L. Ge, Y. Chen, X. Mao, D. Guan, M. Li, Y. Zhong, Z. Hu, V. K. Peterson, M. Saunders, C.-T. Chen, H. Zhang, R. Ran, A. Du, H. Wang, S. P. Jiang, W. Zhou, Z. Shao, *Small* **2021**, *17*, 2101573; e) H. Zhang, D. Guan, Z. Hu, Y.-C. Huang, X. Wu, J. Dai, C.-L. Dong, X. Xu, H.-J. Lin, C.-T. Chen, W. Zhou, Z. Shao, *Appl. Catal., B* **2021**, *297*, 120484.
- [53] a) Y. Zhang, Y. Lin, T. Duan, L. Song, *Mater. Today* **2021**, <https://doi.org/10.1016/j.mattod.2021.02.004>; b) K. Chu, Y.-p. Liu, Y.-b. Li, Y.-l. Guo, Y. Tian, *ACS Appl. Mater. Interfaces* **2020**, *12*, 7081; c) J.-W. Zhao, C.-F. Li, Z.-X. Shi, J.-L. Guan, G.-R. Li, *Research* **2020**, *2020*, 6961578.
- [54] Z. Zhang, B. He, L. Chen, H. Wang, R. Wang, L. Zhao, Y. Gong, *ACS Appl. Mater. Interfaces* **2018**, *10*, 38032.
- [55] Y. Liu, Y. Dou, S. Li, T. Xia, Y. Xie, Y. Wang, W. Zhang, J. Wang, L. Huo, H. Zhao, *Small Methods* **2021**, *5*, 2000701.
- [56] a) H. Su, Q. Tian, C.-A. H. Price, L. Xu, K. Qian, J. Liu, *Nano Today* **2020**, *31*, 100834; b) M. Yao, B. Wang, B. Sun, L. Luo, Y. Chen, J. Wang, N. Wang, S. Komarneni, X. Niu, W. Hu, *Appl. Catal., B* **2021**, *280*, 119451.
- [57] X. Ao, W. Zhang, B. Zhao, Y. Ding, G. Nam, L. Soule, A. Abdelhafiz, C. Wang, M. Liu, *Energy Environ. Sci.* **2020**, *13*, 3032.
- [58] X. Huang, G. Zhao, G. Wang, J. T. S. Irvine, *Chem. Sci.* **2018**, *9*, 3623.
- [59] B. Zhao, L. Zhang, D. Zhen, S. Yoo, Y. Ding, D. Chen, Y. Chen, Q. Zhang, B. Doyle, X. Xiong, M. Liu, *Nat. Commun.* **2017**, *8*, 14586.
- [60] H. Yu, F. Chu, X. Zhou, J. Ji, Y. Liu, Y. Bu, Y. Kong, Y. Tao, Y. Li, Y. Qin, *Chem. Commun.* **2019**, *55*, 2445.
- [61] J. Dai, Y. Zhu, Y. Zhong, J. Miao, B. Lin, W. Zhou, Z. Shao, *Adv. Mater. Interfaces* **2018**, *6*, 1801317.
- [62] X. Mei, J. Xiong, Y. Wei, Y. Zhang, P. Zhang, Q. Yu, Z. Zhao, J. Liu, *Appl. Catal., B* **2020**, *275*, 119108.
- [63] W. Zhao, Y. Ye, W. Jiang, J. Li, H. Tang, J. Hu, L. Du, Z. Cui, S. Liao, *J. Mater. Chem. A* **2020**, *8*, 15822.
- [64] X. Han, Q. Wang, Z. Zheng, Z. Nan, X. Zhang, Z. Song, M. Ma, J. Zheng, Q. Kuang, L. Zheng, *ACS Sustainable Chem. Eng.* **2021**, *9*, 3821.
- [65] Y. Ma, A. N. Kuhn, W. Gao, T. Al-Zoubi, H. Du, X. Pan, H. Yang, *Nano Energy* **2021**, *79*, 105465.
- [66] A. Grimaud, K. J. May, C. E. Carlton, Y. Lee, M. Risch, W. T. Hong, J. Zhou, Y. Shaohorn, *Nat. Commun.* **2013**, *4*, 2439.
- [67] J. Wang, Y. Gao, D. Chen, J. Liu, Z. Zhang, Z. Shao, F. Ciucci, *ACS Catal.* **2017**, *8*, 364.
- [68] R. Pelosato, G. Cordaro, D. Stucchi, C. Cristiani, G. Dotelli, *J. Power Sources* **2015**, *298*, 46.
- [69] E. Marelli, J. Gazquez, E. Poghosyan, E. Müller, D. J. Gawryluk, E. Pomjakushina, D. Sheptyakov, C. Piamonteze, D. Aegerter, T. J. Schmidt, M. Medarde, E. Fabbri, *Angew. Chem., Int. Ed.* **2021**, *60*, 14609.
- [70] X. Miao, L. Wu, Y. Lin, X. Yuan, J. Zhao, W. Yan, S. Zhou, L. Shi, *Chem. Commun.* **2019**, *55*, 1442.
- [71] J. S. Kim, B. Kim, H. Kim, K. Kang, *Adv. Energy Mater.* **2018**, *8*, 1702774.
- [72] B.-J. Kim, E. Fabbri, I. E. Castelli, M. Borlaf, T. Graule, M. Nachtegaal, T. J. Schmidt, *Catalysts* **2019**, *9*, 263.
- [73] A. Seong, J. Kim, D. Jeong, S. Sengodan, M. Liu, S. Choi, G. Kim, *Adv. Sci.* **2021**, *8*, 2004099.
- [74] Y. Zhu, Z. He, Y. Choi, H. Chen, X. Li, B. Zhao, Y. Yu, H. Zhang, K. A. Stoerzinger, Z. Feng, Y. Chen, M. Liu, *Nat. Commun.* **2020**, *11*, 4299.
- [75] Y. Zhu, Q. Lin, Y. Zhong, H. A. Tahini, Z. Shao, H. Wang, *Energy Environ. Sci.* **2020**, *13*, 3361.
- [76] a) X. Xu, Y. Chen, W. Zhou, Z. Zhu, C. Su, M. Liu, Z. Shao, *Adv. Mater.* **2016**, *28*, 6442; b) D. Guan, J. Zhou, Y.-C. Huang, C.-L. Dong, J.-Q. Wang, W. Zhou, Z. Shao, *Nat. Commun.* **2019**, *10*, 3755; c) Z. Zhang, W. Zhou, Z. Yang, J. Jiang, D. Chen, Z. Shao, *Int. J. Hydrogen Energy* **2020**, *45*, 24859; d) X. Liu, L. Yang, Z. Zhou, L. Zeng, H. Liu, Y. Deng, J. Yu, C. Yang, W. Zhou, *Chem. Eng. J.* **2020**, *399*, 125779; e) J. Yu, X. Wu, D. Guan, Z. Hu, S.-C. Weng, H. Sun, Y. Song, R. Ran, W. Zhou, M. Ni, Z. Shao, *Chem. Mater.* **2020**, *32*, 4509.
- [77] Q. Sun, Z. Dai, Z. Zhang, Z. Chen, H. Lin, Y. Gao, D. Chen, *J. Power Sources* **2019**, *427*, 194.
- [78] H. Togano, K. Asai, S. Oda, H. Ikeno, S. Kawaguchi, K. Oka, K. Wada, S. Yagi, I. Yamada, *Mater. Chem. Front.* **2020**, *4*, 1519.
- [79] D. Guan, J. Zhou, Z. Hu, W. Zhou, X. Xu, Y. Zhong, B. Liu, Y. Chen, M. Xu, H. J. Lin, C. T. Chen, J. Q. Wang, Z. Shao, *Adv. Funct. Mater.* **2019**, *29*, 1900704.
- [80] H. Sun, X. Xu, Z. Hu, L. H. Tjeng, J. Zhao, Q. Zhang, H.-J. Lin, C.-T. Chen, T.-S. Chan, W. Zhou, Z. Shao, *J. Mater. Chem. A* **2019**, *7*, 9924.
- [81] Z. Du, H. Zhao, S. Yi, Q. Xia, Y. Gong, Y. Zhang, X. Cheng, Y. Li, L. Gu, K. Swierczek, *ACS Nano* **2016**, *10*, 8660.
- [82] J. Ahmed, N. Alhokbany, M. Ubaidullah, S. Mutehri, M. A. M. Khan, S. M. Alshehri, *Ceram. Int.* **2020**, *46*, 20038.
- [83] M. Jiang, J. Li, Y. Zhao, L. Pan, Q. Cao, D. Wang, Y. Du, *ACS Appl. Mater. Interfaces* **2018**, *10*, 19746.
- [84] Y. Tong, J. Wu, P. Chen, H. Liu, W. Chu, C. Wu, Y. Xie, *J. Am. Chem. Soc.* **2018**, *140*, 11165.
- [85] M. Retuerto, F. Calle-Vallejo, L. Pascual, G. Lumbeeck, M. T. Fernandez-Diaz, M. Croft, J. Gopalakrishnan, M. A. Peña, J. Hadermann, M. Greenblatt, S. Rojas, *ACS Appl. Mater. Interfaces* **2019**, *11*, 21454.
- [86] a) H. Wang, C. Zhao, G. Wang, H. Zhang, *J. Mater. Chem. A* **2021**, *9*, 10289; b) Y. Zhu, W. Zhou, J. Yu, Y. Chen, M. Liu, Z. Shao, *Chem. Mater.* **2016**, *28*, 1691; c) S. Yagi, I. Yamada, H. Tsukasaki, A. Seno, M. Murakami, H. Fujii, H. Chen, N. Umezawa, H. Abe, N. Nishiyama, S. Mori, *Nat. Commun.* **2015**, *6*, 8249.

- [87] I. Yamada, A. Takamatsu, K. Asai, H. Ohzuku, T. Shirakawa, T. Uchimura, S. Kawaguchi, H. Tsukasaki, S. Mori, K. Wada, H. Ikeno, S. Yagi, *ACS Appl. Energy Mater.* **2018**, *1*, 3711.
- [88] H. S. Kushwaha, A. Halder, P. Thomas, R. Vaish, *Electrochim. Acta* **2017**, *252*, 532.
- [89] X. Miao, L. Zhang, L. Wu, Z. Hu, L. Shi, S. Zhou, *Nat. Commun.* **2019**, *10*, 3809.
- [90] H. Andersen, K. Xu, D. Malyshekin, R. Strandbakke, A. Chatzidakis, *Chem. Commun.* **2020**, *56*, 1030.
- [91] B. Hua, Y.-F. Sun, M. Li, N. Yan, J. Chen, Y.-Q. Zhang, Y. Zeng, B. S. Amirkhiz, J.-L. Luo, *Chem. Mater.* **2017**, *29*, 6228.
- [92] Y. Zhu, L. Zhang, B. Zhao, H. Chen, X. Liu, R. Zhao, X. Wang, J. Liu, Y. Chen, M. Liu, *Adv. Funct. Mater.* **2019**, *29*, 1970236.
- [93] X. Wang, Y. Dou, Y. Xie, J. Wang, T. Xia, L. Huo, H. Zhao, *ACS Omega* **2020**, *5*, 12501.
- [94] N.-I. Kim, S.-H. Cho, S. H. Park, Y. J. Lee, R. A. Afzal, J. Yoo, Y.-S. Seo, Y. J. Lee, J.-Y. Park, *J. Mater. Chem. A* **2018**, *6*, 17807.
- [95] H. Zhang, D. Guan, X. Gao, J. Yu, G. Chen, W. Zhou, Z. Shao, *J. Mater. Chem. A* **2019**, *7*, 19228.
- [96] R. K. Hona, F. Ramezanipour, *Angew. Chem., Int. Ed.* **2019**, *58*, 2060.
- [97] N. Kumar, K. Naveen, M. Kumar, T. C. Nagaiah, R. Sakla, A. Ghosh, V. Siruguri, S. Sadhukhan, S. Kanungo, A. K. Paul, *ACS Appl. Energy Mater.* **2021**, *4*, 1323.
- [98] M. Qu, X. Ding, Z. Shen, M. Cui, F. E. Oropeza, G. Gorni, V. A. d. I. P. O'Shea, W. Li, D.-C. Qi, K. H. L. Zhang, *Chem. Mater.* **2021**, *33*, 2062.
- [99] H. Sun, Z. Hu, X. Xu, J. He, J. Dai, H.-J. Lin, T.-S. Chan, C.-T. Chen, L. H. Tjeng, W. Zhou, Z. Shao, *Chem. Mater.* **2019**, *31*, 5919.
- [100] H. Sun, X. Xu, G. Chen, Y. Zhou, H. J. Lin, C. T. Chen, R. Ran, W. Zhou, Z. Shao, *ChemSusChem* **2019**, *12*, 5111.
- [101] G. Chen, Z. Hu, Y. Zhu, Z.-G. Chen, Y. Zhong, H.-J. Lin, C.-T. Chen, L. H. Tjeng, W. Zhou, Z. Shao, *J. Mater. Chem. A* **2018**, *6*, 9854.
- [102] H. Sun, G. Chen, J. Sunarso, J. Dai, W. Zhou, Z. Shao, *ACS Appl. Mater. Interfaces* **2018**, *10*, 16939.
- [103] O. Diaz-Morales, S. Raaijman, R. Kortlever, P. J. Kooyman, T. Wezendonk, J. Gascon, W. T. Fu, M. T. M. Koper, *Nat. Commun.* **2016**, *7*, 12363.
- [104] I. Yamada, H. Fujii, A. Takamatsu, H. Ikeno, K. Wada, H. Tsukasaki, S. Kawaguchi, S. Mori, S. Yagi, *Adv. Mater.* **2017**, *29*, 1603004.
- [105] a) X. Zhao, H. Cheng, L. Song, L. Han, R. Zhang, G. Kwon, L. Ma, S. N. Ehrlich, A. I. Frenkel, J. Yang, K. Sasaki, H. L. Xin, *ACS Catal.* **2021**, *11*, 184; b) S. C. Peter, S. Sarkar, *Chem. - Asian J.* **2021**, *16*, 1184.
- [106] H.-S. Chen, T. M. Benedetti, V. R. Gonçalves, N. M. Bedford, R. W. J. Scott, R. F. Webster, S. Cheong, J. J. Gooding, R. D. Tilley, *J. Am. Chem. Soc.* **2020**, *142*, 3231.
- [107] H. Y. Kim, T. Kwon, Y. Ha, M. Jun, H. Baik, H. Y. Jeong, H. Kim, K. Lee, S. H. Joo, *Nano Lett.* **2020**, *20*, 7413.
- [108] Z. Wang, X. Yao, Y. Kang, L. Miao, D. Xia, L. Gan, *Adv. Funct. Mater.* **2019**, *29*, 1902987.
- [109] M. Liu, A. Hu, Y. Ma, G. Wang, L. Zou, X. Chen, H. Yang, *J. Electroanal. Chem.* **2020**, *871*, 114267.
- [110] X. Zhao, C. Xi, R. Zhang, L. Song, C. Wang, J. S. Spendelow, A. I. Frenkel, J. Yang, H. L. Xin, K. Sasaki, *ACS Catal.* **2020**, *10*, 10637.
- [111] X. Wang, L. Zhang, F. Wang, J. Yu, H. Zhu, *Prog. Nat. Sci.: Mater. Int.* **2020**, *30*, 905.
- [112] J. Zhu, Y. Yang, L. Chen, W. Xiao, H. Liu, H. D. Abruña, D. Wang, *Chem. Mater.* **2018**, *30*, 5987.
- [113] Y. Yang, W. Xiao, X. Feng, Y. Xiong, M. Gong, T. Shen, Y. Lu, H. D. Abruña, D. Wang, *ACS Nano* **2019**, *13*, 5968.
- [114] J. T. L. Gamler, K. Shin, H. M. Ashberry, Y. Chen, S. L. A. Bueno, Y. Tang, G. Henkelman, S. E. Skrabalak, *Nanoscale* **2020**, *12*, 2532.
- [115] J. Guo, L. Gao, X. Tan, Y. Yuan, J. Kim, Y. Wang, H. Wang, Y.-J. Zeng, S.-I. Choi, S. C. Smith, H. Huang, *Angew. Chem., Int. Ed.* **2021**, *60*, 10942.
- [116] J. Yu, Y. Dai, Q. He, C. Cheng, Z. Shao, M. Ni, *Appl. Phys. Rev.* **2020**, *7*, 041304.
- [117] S.-J. Ji, H.-G. Xue, N.-T. Suen, *Chem. Commun.* **2020**, *56*, 14303.
- [118] M. M. F. Espinosa, T. Cheng, M. Xu, L. Abatemarco, C. Choi, X. Pan, W. A. Goddard, Z. Zhao, Y. Huang, *ACS Energy Lett.* **2020**, *5*, 3672.
- [119] C. Lin, Z. Huang, Z. Zhang, T. Zeng, R. Chen, Y. Tan, W. Wu, S. Mu, N. Cheng, *ACS Sustainable Chem. Eng.* **2020**, *8*, 16938.
- [120] A. Samanta, S. Das, S. Jana, *Nanoscale Adv.* **2020**, *2*, 417.
- [121] H. Shi, Y.-T. Zhou, R.-Q. Yao, W.-B. Wan, X. Ge, W. Zhang, Z. Wen, X.-Y. Lang, W.-T. Zheng, Q. Jiang, *Nat. Commun.* **2020**, *11*, 2940.
- [122] K. Chen, S. Kim, R. Rajendiran, K. Prabakar, G. Li, Z. Shi, C. Jeong, J. Kang, O. L. Li, *J. Colloid Interface Sci.* **2021**, *582*, 977.
- [123] Y. Xiong, L. Xiao, Y. Yang, F. J. DiSalvo, H. D. Abruña, *Chem. Mater.* **2018**, *30*, 1532.
- [124] M. Gong, J. Zhu, M. Liu, P. Liu, Z. Deng, T. Shen, T. Zhao, R. Lin, Y. Lu, S. Yang, Z. Liang, S. M. Bak, E. Stavitski, Q. Wu, R. R. Adzic, H. L. Xin, D. Wang, *Nanoscale* **2019**, *11*, 20301.
- [125] C. He, Z. Ma, Q. Wu, Y. Cai, Y. Huang, K. Liu, Y. Fan, H. Wang, Q. Li, J. Qi, Q. Li, X. Wu, *Electrochim. Acta* **2020**, *330*, 135119.
- [126] Y. He, Y. L. Wu, X. X. Zhu, J. N. Wang, *ACS Appl. Mater. Interfaces* **2019**, *11*, 11527.
- [127] X. Zou, L. Wang, X. Ai, H. Chen, X. Zou, *Chem. Commun.* **2020**, *56*, 3061.
- [128] Y. Wang, D. Sun, T. Chowdhury, J. S. Wagner, T. J. Kempa, A. S. Hall, *J. Am. Chem. Soc.* **2019**, *141*, 2342.
- [129] L. Peng, L. Zhou, W. Kang, R. Li, K. Qu, L. Wang, H. Li, *Nanomaterials* **2020**, *10*, 1893.
- [130] J. Liang, S. Li, Y. Chen, X. Liu, T. Wang, J. Han, S. Jiao, R. Cao, Q. Li, *J. Mater. Chem. A* **2020**, *8*, 15665.
- [131] L. Zhou, X. Deng, Q. Lu, G. Yang, W. Zhou, Z. Shao, *Energy Fuels* **2020**, *34*, 11527.
- [132] M. Bao, X. Chen, S. Hu, L. Zhang, Y. Li, C. Carraro, R. Maboudian, W. Wei, Y. Zhang, S. Liu, *J. Mater. Chem. A* **2020**, *8*, 21327.
- [133] Z. Ding, J. Bian, S. Shuang, X. Liu, Y. Hu, C. Sun, Y. Yang, *Adv. Sustainable Syst.* **2020**, *4*, 1900105.
- [134] P. Zhang, H.-G. Xue, N.-T. Suen, *Chem. Commun.* **2019**, *55*, 14406.
- [135] H. Shi, Y.-T. Zhou, R.-Q. Yao, W.-B. Wan, Q.-H. Zhang, L. Gu, Z. Wen, X.-Y. Lang, Q. Jiang, *Research* **2020**, *2020*, 2987234.
- [136] D. Chen, J. Zhu, X. Mu, R. Cheng, W. Li, S. Liu, Z. Pu, C. Lin, S. Mu, *Appl. Catal., B* **2020**, *268*, 118729.
- [137] a) Y. Zhou, H. J. Fan, *ACS Mater. Lett.* **2021**, *3*, 136; b) D. Guan, W. Zhou, Z. Shao, *Small Sci.* **2021**, 2100030.
- [138] S. Ye, J. Wang, J. Hu, Z. Chen, L. Zheng, Y. Fu, Y. Lei, X. Ren, C. He, Q. Zhang, J. Liu, *ACS Catal.* **2021**, *11*, 6104.
- [139] J. Shan, C. Ye, S. Chen, T. Sun, Y. Jiao, L. Liu, C. Zhu, L. Song, Y. Han, M. Jaroniec, Y. Zhu, Y. Zheng, S.-Z. Qiao, *J. Am. Chem. Soc.* **2021**, *143*, 5201.
- [140] a) W. Cai, R. Chen, H. Yang, H. B. Tao, H.-Y. Wang, J. Gao, W. Liu, S. Liu, S.-F. Hung, B. Liu, *Nano Lett.* **2020**, *20*, 4278; b) G. Chen, Y. Zhu, H. M. Chen, Z. Hu, S. F. Hung, N. Ma, J. Dai, H. J. Lin, C. T. Chen, W. Zhou, Z. Shao, *Adv. Mater.* **2019**, *31*, 1900883.
- [141] a) Q. Ji, L. Bi, J. Zhang, H. Cao, X. S. Zhao, *Energy Environ. Sci.* **2020**, *13*, 1408; b) Q. Wang, Y. Lei, D. Wang, Y. Li, *Energy Environ. Sci.* **2019**, *12*, 1730.
- [142] a) J. Cai, J. Ding, D. Wei, X. Xie, B. Li, S. Lu, J. Zhang, Y. Liu, Q. Cai, S. Zang, *Adv. Energy Mater.* **2021**, *11*, 2100141; b) Z. Xiao, Y.-C. Huang, C.-L. Dong, C. Xie, Z. Liu, S. Du, W. Chen, D. Yan, L. Tao, Z. Shu, G. Zhang, H. Duan, Y. Wang, Y. Zou, R. Chen, S. Wang, *J. Am. Chem. Soc.* **2020**, *142*, 12087; c) W. Li, D. Wang, Y. Zhang, L. Tao, T. Wang, Y. Zou, Y. Wang, R. Chen, S. Wang, *Adv. Mater.* **2020**, *32*, 1907879.
- [143] a) B. Pattengale, Y. Huang, X. Yan, S. Yang, S. Younan, W. Hu, Z. Li, S. Lee, X. Pan, J. Gu, J. Huang, *Nat. Commun.* **2020**, *11*, 4114; b) Y. Huang, Y. Sun, X. Zheng, T. Aoki, B. Pattengale, J. Huang,

- X. He, W. Bian, S. Younan, N. Williams, J. Hu, J. Ge, N. Pu, X. Yan, X. Pan, L. Zhang, Y. Wei, J. Gu, *Nat. Commun.* **2019**, *10*, 982; c) A. R. P. Santiago, T. He, O. Eraso, M. A. Ahsan, A. N. Nair, V. S. N. Chava, T. Zheng, S. Pilla, O. Fernandez-Delgado, A. Du, S. T. Sreenivasan, L. Echegoyen, *J. Am. Chem. Soc.* **2020**, *142*, 17923.
- [144] X. Zhou, J. Dong, Y. Zhu, L. Liu, Y. Jiao, H. Li, Y. Han, K. Davey, Q. Xu, Y. Zheng, S.-Z. Qiao, *J. Am. Chem. Soc.* **2021**, *143*, 6681.
- [145] Z. Fan, L. Zhang, D. Baumann, L. Mei, Y. Yao, X. Duan, Y. Shi, J. Huang, Y. Huang, X. Duan, *Adv. Mater.* **2019**, *31*, 1900608.
- [146] a) M. Wang, L. Árnadóttir, Z. J. Xu, Z. Feng, *Nano-Micro Lett.* **2019**, *11*, 47; b) Y. Yang, Y. Wang, Y. Xiong, X. Huang, L. Shen, R. Huang, H. Wang, J. P. Pastore, S.-H. Yu, L. Xiao, J. D. Brock, L. Zhuang, H. D. Abruña, *J. Am. Chem. Soc.* **2019**, *141*, 1463.
- [147] Y. Xu, C. Wang, Y. Huang, J. Fu, *Nano Energy* **2021**, *80*, 105545.
- [148] Q. Che, Q. Li, Y. Tan, X. Chen, X. Xu, Y. Chen, *Appl. Catal., B* **2019**, *246*, 337.
- [149] X. Li, L. Zhao, J. Yu, X. Liu, X. Zhang, H. Liu, W. Zhou, *Nano-Micro Lett.* **2020**, *12*, 131.



**Hainan Sun** received his Ph.D. in chemical engineering from Nanjing Tech University, China, in 2020. He is currently a Postdoctoral Fellow working with Prof. WooChul Jung at Korea Advanced Institute of Science and Technology (KAIST), Republic of Korea. His research interests focus on design and synthesis of perovskite oxides, metal sulfides, and metal phosphides and their applications in electrochemical catalytic fields.



**Sanzhaio Song** obtained his Ph.D. in inorganic chemistry from University of Chinese Academy of Sciences in 2019. He is currently a Postdoctoral Fellow working in Shanghai Institute of Applied Physical, Chinese Academy of Science, China. His research has been focusing on molten salt method synthesis of metal oxides for both water splitting and CO<sub>2</sub> reduced reaction, and hard/soft X-ray absorption spectroscopy techniques.



**Xiaomin Xu** received his Ph.D. in chemical engineering from Curtin University, Australia. He is currently a Research Associate at Curtin University. His research interests are mainly focused on the development of perovskite oxides and other functional materials for applications in electrochemical energy storage and conversion.



**Jie Dai** received his Bachelor (2016) and Ph.D. (2021) degree in chemical engineering from Nanjing Tech University, China. He is currently a Postdoctoral Fellow working with Prof. Lizhi Zhang at School of Environmental Science and Engineering, Shanghai Jiao Tong University, China. His research involves the design of metal-oxide and single-atom electrocatalysts for energy conversion and multifunction applications.



**Jie Yu** completed her Ph.D. program in chemical engineering from Nanjing Tech University, China, in 2018. She is now a postdoctoral fellow in Hong Kong Polytechnic University, Hong Kong, China. Her research interests focus on design and synthesis of perovskite oxides, metal sulfides, metal phosphides, and carbon composites and their applications in electrochemical catalytic fields.



**Wei Zhou** earned his Ph.D. from Nanjing Tech University in 2009, where he carried out research on the development and synthesis of high-performance cathode materials for solid-oxide fuel cells. He was awarded Australian Postdoctoral Fellow to work at the University of Queensland in 2010, and then promoted to research fellow in 2013. In 2015, he became a Professor at Nanjing Tech University. His research interests include the development of key materials for low-temperature SOFCs; electrocatalysts for the ORR/OER/HER; MIECs for wastewater treatment; and scale-up of direct carbon fuel-cell stacks.



**Zongping Shao** is a Professor of chemical engineering at Nanjing Tech University, China and Curtin University, Australia. He obtained his Ph.D. from Dalian Institute of Chemical Physics, China, in 2000. He worked as a visiting scholar at Institut de Recherches Sur La Catalyse, CNRS, France, and postdoc at California Institute of Technology, USA, from 2000 till 2005. His current research interests include solid oxide fuel cells, lithium ion batteries, oxygen-permeable membranes, and low temperature energy conversion devices.



**WooChul Jung** received his Ph.D. degree at MIT and served as postdoctoral fellow at Caltech. He joined KAIST of the Department of MSE in 2013 and currently serves as Associate Professor. The main goal of his research activities is to understand the reactions that occur at the interfaces between ionic solids (oxides in particular) and gases and thereby to improve the reaction kinetics for applications in chemical and electrochemical catalysis, such as, solid oxide fuel cells, electrolyzers, and hydrocarbon reformers. He has been developing model oxide structures with well-defined interface geometries and analyzing true surface properties and reaction characteristics.